

LINKING MULTI-YEAR AND MULTI-SENSOR LAND COVER DATA TO
WATER YIELD IN THE NUECES HEADWATERS WATERSHED OF TEXAS

A Thesis

by

YAVUZ DONER

Submitted to the Office of Graduate and Professional Studies of
Texas A&M University
in partial fulfillment of the requirements for the degree of

MASTER OF SCIENCE

Chair of Committee,	Jianbang Gan
Co-Chair of Committee,	Sorin Popescu
Committee Members,	Thomas W. Boutton John Nielsen-Gammon
Head of Department,	Cliff Lamb

December 2018

Major Subject: Ecosystem Science and Management

Copyright 2018 Yavuz Doner

ABSTRACT

The stress on water resources is more critical in drylands due to ecological and climatological changes. Because upscaling the findings of paired-catchment studies to larger watersheds is difficult, hydrological models like the Soil and Water Assessment Tool (SWAT) were oftentimes used to investigate the impact of land use and land cover changes (LULC) on water yield. Such modeling studies first require the accurate estimates of LULC change using remote sensing images, which has been hindered by the presence of shadows in these images. Also, the data used in many previous modeling studies didn't have the extent of variations in LULC and other variables including climatic conditions comparable to the simulation scenarios. The objectives of this study are to classify LULC types in the shadow areas of aerial images; to evaluate the complement between LULC data and ancillary data; to estimate LULC change; and to assess the impact of the LULC change on the water yield of the Nueces River Headwaters watershed using multi-year and multi-sensor LULC data and the SWAT model.

More than 99% of the shadow area was identified with a 92.68% average accuracy. This outcome indicates that LULC types of shadow area on higher-resolution images can be classified successfully with a straightforward method incorporating the multi-sensor LULC classification schemes. The high accuracy of multi-year and multi-sensor LULC maps revealed the benefits of ancillary data use in remote sensing image classification. LULC change detection analysis was conducted using higher-resolution

maps for precise quantification. There was at least an 8% reduction in juniper cover from 2008 to 2014 in the watershed. To account for variations in LULC, 2008, 2012 and 2016 maps were used to set up multiple SWAT models. Although satisfactory model performance statistics obtained from calibration, model performance was degraded for the validation period. This indicated that the model couldn't sufficiently assess the variation in LULC and weather for a relatively brief period in the specific karst watershed. This study may be the first study conducted in a large karst watershed in the Edwards Plateau which accounted for the watershed-wide LULC changes for the entire modeling period.

ACKNOWLEDGEMENTS

I would like to express my gratitude first to God who guided me through a very challenging part of my life. I would like to thank a lot to my fiancé, Busra Sarikaya due to her passionate support and patience. She has been my reason to work and struggle hard. I owe a great thank you to Necmi Gunes who contributed a lot to my self-development with both his inspiring character and friendliness. He has always been like a father to me. I would like to thank my brother Fatih for his advices and support. I am also so thankful to my mom due to her love and support.

Special thanks go to my advisor Dr. Gan for his guidance throughout the progression of this research. I would like to thank a lot to my committee co-chair Dr. Popescu for helping me acquire experience in remote sensing. I am also so grateful to Dr. Srinivasan for his patience and very prompt responses. I also thank a lot to my committee members Dr. Boutton and Dr. Nielsen for their contributions to my learning experience at Texas A&M university.

I would also like to thank a lot to the Republic of Turkey, for providing me with a fantastic opportunity to expand my knowledge in ecosystem science and management at one of the best universities in the world. I also thank my friends, colleagues, faculty and staff in the Department of Ecosystem Science and Management for making my experience at Texas A&M valuable.

CONTRIBUTORS AND FUNDING SOURCES

Contributors

This work was supervised by a thesis committee consisting of Professors Jianbang Gan (advisor), Sorin Popescu (co-advisor) , and Thomas W. Boutton of the Department of Ecosystem Science and Management and Professor John Nielsen-Gammon of the Department of Atmospheric Sciences.

All work for the thesis was completed independently by the student.

Funding Sources

Graduate study was supported by a sponsorship from the Republic of Turkey.

NOMENCLATURE

ET	Evapotranspiration
NAIP	National Agricultural Imagery Program
USGS	United States Geological Survey
TOP	Texas Orthoimagery Program
DQQQ	Digital Orthophoto Quadrangle Quad
LULC	Land Use Land Cover
ML	Maximum Likelihood
SVM	Support Vector Machine
SWAT	Soil and Water Assessment Tool
SSURGO	Soil Survey Geographic
NLCD	National Land Cover Database
EMS	Ecological Mapping Systems
TEAM	Texas Ecosystem Analytical Mapper
TNRIS	Texas Natural Resources Information System
HRU	Hydrologic Response Unit

TABLE OF CONTENTS

	Page
ABSTRACT	ii
ACKNOWLEDGEMENTS	iv
CONTRIBUTORS AND FUNDING SOURCES.....	v
NOMENCLATURE.....	vi
TABLE OF CONTENTS	vii
LIST OF FIGURES.....	ix
LIST OF TABLES	xv
CHAPTER I INTRODUCTION	1
I.1 Background of the Study	1
I.2 Problem Statement	5
I.3 Research Hypotheses	7
I.4 Objectives	7
CHAPTER II LITERATURE REVIEW.....	8
II.1 Brush Encroachment and Management on the Edwards Plateau	8
II.2 Using Remotely Sensed Data for Mapping LULC and Change Detection	9
II.3 Soil and Water Assessment Tool (SWAT) in Hydrological Analysis.....	14
CHAPTER III RESEARCH METHODOLOGY	29
III.1 Location of The Study Area	29
III.2 Climate, Topography, Land Use and Cover and Geology of The Study Area	29
III.3 Spatial and Temporal Datasets.....	34
III.4 Analysis of the Climate and Hydrology of the Study Area.....	39
III.4.1 Rainfall and Runoff.....	39
III.4.2 Delineation of the Drainage Area.....	43
III.5 Remote Sensing Image Classifications	44
III.5.1 Preprocessing of the aerial images	44
III.5.2 Determining the Classification Scheme	48

III.5.3 Training Data Collection and Analysis of Spectral Separability	60
III.5.4 Preprocessing of Landsat Satellite images	67
III.5.5 Classification Scheme of Landsat Images.....	68
III.5.6 Training Data for Landsat Images and Spectral Separability.....	70
III.5.7 Classification of Aerial and Satellite Images	72
III.6 Intermediary Statistics and Classification Editing	74
III.6.1 Aerial Image Classifications and Initial Editing	74
III.6.2 Satellite Image Classifications and Post Classification Editing.....	80
III.7 Accuracy Assessment of the Classified Images	85
III.7.1 Collection of Validation Samples.....	88
III.7.2 Accuracy of the Initial Aerial Image Classifications and Final Satellite Thematic Maps.....	90
III.8 Identifying Shadow Pixels on Aerial Images and Associated Accuracy	92
III.9 Thematic Change Detection Analysis	99
III.10 Analyzing the Relationship Between Mapped Tree Cover, Interpolated Rainfall and Measured Streamflow.....	103
III.11 Modeling the Hydrological Impact of LULC Change	104
III.12 Model Setup and Watershed Delineation.....	106
III.13 Hydrologic Response Unit (HRU) Analysis	109
III.14 Writing Input Tables	119
III.15 Calibration and Validation of the SWAT Model	121
III.16 Model Simulation Scenario.....	138
 CHAPTER IV RESULTS AND DISCUSSION	 142
IV.1 Interpolated Annual Rainfall, Measured Water Yield and Baseflow Ratio.....	142
IV.2 Land Use and Cover Maps and Change Detection	147
IV.2.1 Accuracy of the Shadow Identification Approach and Final Thematic Maps	147
IV.2.2 Thematic Change Detection.....	154
IV.3 Statistical Relationship Between Annual Rainfall, Tree Cover and Water Yield.....	160
IV.4 Quantified 3 rd Level LULC Classes within The NLCD 2011 Classes	164
IV.5 Model Results	166
IV.5.1 Calibration and Sensitivity Analysis.....	166
IV.5.2 Results of the Model Validation	176
IV.5.3 Results of the Verification and Scenario Analysis.....	186
 CHAPTER V CONCLUSION	 193
 REFERENCES.....	 198

LIST OF FIGURES

	Page
Figure 1. Study area.	30
Figure 2. Annual precipitation of the study area from 1984-2017 (data from NCDC)....	32
Figure 3. The upstream rivers and creeks of the Nueces Rv Nr Barksdale gaging station. (Source: the USGS Streamer application)	32
Figure 4. Average annual and monthly precipitation of the study period (data from NCDC).....	33
Figure 5. Areas with no data indicated by the small white scattered pixels on the water body (top left of the image) and within the woodland (bottom left).	44
Figure 6. Natural color composite (top left), NIR false color composite (top right), texture band derived from the image (bottom left) and NDVI band (bottom right) of the 2008 aerial image. The area covered in the image is only 2.72 square kilometers and the scale is about 1/10000 (the study area is 907 square kilometers). The city seen in the images is Barksdale.	47
Figure 7. Locations of the 3D viewed junipers and oaks along Ranch Road 355. Yellow line indicates the boundaries of the study area.	54
Figure 8. Distinguishing between junipers and oaks. All aerial images are displayed as near-infrared color composite (NIR-False color). The lower part is the exact cursor location displayed in Google Earth 3D View. While junipers have darker red color, oaks can be distinguished by bright red color. On the right-hand side of the road is mainly juniper while oaks are on the left.....	55
Figure 9. The progression of brush management from 2008 to 2012. Images displayed in smaller windows are TOP 2008 (top left), NAIP 2010 (top right), NAIP 2012 (bottom left) and TEAM land use land cover data.	56
Figure 10. Juniper mortality due to chemical treatment or drought.....	57
Figure 11. Two separate locations for 2008, 2010, 2012, 2014, 2015, and 2016 showing the juniper mortality. Juniper mortality occurred after 2010.	61
Figure 12. Parcels allocated to collect validation points (outlined with yellow color). ...	64
Figure 13. Training data collection processes for Landsat Images. The ENVI screen above indicates an area of oak savanna (to the right of the image) and	

juniper area (to the left of the image). The TEAM land use and cover dataset was displayed on the bottom left window. Images shown in the screen on top are Landsat8 2014, TOP 2008, NAIP 2014 and TEAM data from left to right, respectively. A brush management site is shown at the bottom of the ENVI split screen. The images displayed at the bottom screen are Landsat8 2015, TOP 2008, NAIP 2015 and TEAM dataset from left to right, respectively.	71
Figure 14. Classification of the 2008 image before combining urban with barren and dry herbaceous with green grass (above) and after applying combinations (below).....	76
Figure 15. A juniper treatment site in 2008 aerial image (left) and the Maximum Likelihood classification result for the same location (right). Oaks, junipers, herbaceous, barren areas, and dead junipers were indicated by darker green, light green, yellow, white, and red color, respectively.	77
Figure 16. Misclassified dead juniper pixels. On the left is the NIR false-color composite of TOP 2008 aerial image, and on the right is the ML classification of 2008 image.	79
Figure 17. Intensive shadow cover of 2014 and 2015 aerial images. The images below from left to right are 2014 and 2015 ML classifications, respectively.	80
Figure 18. Correcting for water pixels in Landsat 2013 ML classification image using the information from the same image's SVM classification. While water pixels scatter around in the 2013 ML product (top), they were substituted with the juniper pixels imported from the SVM (bottom).....	84
Figure 19. Collecting validation samples for 2015 Landsat 8 image using both aerial photographs and TEAM dataset. Images seen on the split screen are 2015 Landsat image (top left), 2008 TOP aerial image (top right), 2015 NAIP image (bottom left) and TEAM LULC dataset (bottom right).	89
Figure 20. An oaksavanna vector derived from Landsat image classification overlain on the corresponding aerial image.	93
Figure 21. Water vector file derived from Landsat ML classification overlain on the aerial image.....	95
Figure 22. The image on top shows the oak vector file displayed over the NIR false-color composite of 2008 aerial image. The image below indicates the conversion of shadows to oaks on 2008 ML classification of the aerial image utilizing the oak vector file derived from 2008 Landsat ML classification. Darker green represents oaks, and light green color represents	

juniper trees. Note that the location depicted by the classifications is not the same with the image shown at the top.	96
Figure 23. Before (top right) and after (bottom left) shadow detection in 2008 aerial image classifications. The image on the top left is the NIR false-color composite of the 2008 image, the image bottom left is from the TEAM LULC map.	97
Figure 24. Maximum Likelihood classification of 2008 aerial image before (bottom left) and after (bottom right) shadow editing. The urban area is also finalized after editing shadows.	97
Figure 25. Validation data collection on ENVI for the accuracy assessment of the edited shadow areas. Images in the top row are 2008, 2010, and 2012, and images in the second row are 2014, 2015, and 2016, respectively. All images displayed as near infrared false-color composite.	98
Figure 26. A brush treatment site where junipers were removed, and oaks were left. Images in the left column from top to bottom are 2015 Landsat 8 and 2015 NAIP images, respectively. In the right column are the 2008 TOP image (top) the TEAM dataset (bottom).	100
Figure 27. Seasonal changes in unvegetated and herbaceous land covers. Images shown from left to right are 2008, 2012 and 2016 aerial images (above) and corresponding classification images (below).	101
Figure 28. Iterations to find the best window size for post classification thematic change aggregation.	103
Figure 29. The stream network and delineated watershed. The three weather stations used by SWAT are the closest ones to the study area out of 8 stations inputted to the model.	107
Figure 30. Masking out the oak cover of the 2008 thematic map.	110
Figure 31. Land use and cover of the study area derived from the 2008 aerial image. .	114
Figure 32. The slope categories of the study area.	116
Figure 33. Final HRU distribution for the calibration model (2012-2015) in the study area.	118
Figure 34. The SWAT model input tables.	120
Figure 35. The calibration period model configuration.	121

Figure 36. The subbasins with losing streams and subbasins with sustained flow.	124
Figure 37. Spatial distribution of the hydrological soil groups included in the HRUs and soil classes remained below the defined threshold.	131
Figure 38. Identification of soil classes with corresponding soil hydrological group. ..	132
Figure 39. Screenshots indicating how the rainfall partitioning has improved for the watershed following the activation of crack flow (below).	135
Figure 40. Suitable area for the brush control application.	140
Figure 41. Hypothetical LULC data for the scenario simulation.	141
Figure 42. Normal outlier box plots of precipitation over elevation.	142
Figure 43. Monthly rainfall and streamflow for the period of 2009-2017. Note that the units are different. Rainfall is expressed in mm, and streamflow is expressed in cubic feet per second. This graph was prepared to indicate peak flows as a response to storm events.	145
Figure 44. Annual average precipitation distribution throughout the study area calculated by the IDW method for the period 2009-2017. The precipitation values are expressed in mm.	146
Figure 45. Figure 44: Decreases in intercanopy space from 2014 (left column) to 2015 (right column).	151
Figure 46. Differences in canopy closure between 2015 (left column) and 2016 (right column).	152
Figure 47. A portion of the study area shown by classified (below) and NIR false color composite (above) aerial images. The year of the images from left to right is 2008, 2012 and 2016. Note that the farthest distance in this portion of the area is longer than 10 kilometers.	153
Figure 48. Land cover change at a large brush management site in the study area. The NIR false-color images are 2008, 2010, 2012 (above) and 2014, 2015, 2016 (below) from left to right. Below are the original thematic change maps showing land cover change. On top from left to right, the thematic change maps are 2008-2010, 2008-2012, 2008-2014. Below from left to right 2008-2015 and 2008-2016 thematic change maps are shown. Dark color indicates no change, yellow indicates a change from trees to herbaceous, white indicates a change from trees to unvegetated, and green indicates a change from herbaceous or unvegetated to trees.	156

Figure 49. Aggregated thematic change maps from 2008 to all other years (with 2010, 2012, 2014 above and 2015 and 2016 below and aligned from left to right). Dark color indicates no change, yellow indicates change from trees to herbaceous, and white indicates change from trees to unvegetated.	157
Figure 50. Land cover change at a brush management cite in the study area. Images from left to right are 2008, 2012 and 2016 with the NIR false color composites above and the classified images below.....	158
Figure 51. Spatial distribution of change from juniper cover to herbaceous and barren (from 2008 to 2014).....	159
Figure 52. Annual tree cover, rainfall and water yield in the study area.	162
Figure 53. The best simulation results of iteration 8 for the pre-processed SWAT-NAIP calibration.....	171
Figure 54. The best simulation result of iteration 3 for the default SWAT-NAIP calibration model. Karst features weren't considered in the parametrization.	172
Figure 55. The best simulation of the default SWAT-NAIP calibration iteration 7.	174
Figure 56. The best simulation result of iteration 6 for the SWAT-LANDSAT calibration.	175
Figure 57. The best simulation result of iteration 8 for the SWAT-LANDSAT calibration.	176
Figure 58. Validation simulation of the SWAT-NAIP model with calibrated parameter set 7 of the default model.....	178
Figure 59. The result of the validation simulation of the SWAT-NAIP model with the parameter set 8 from the preprocessed model calibration. No warm-up period was specified.	179
Figure 60. Validation simulation of the pre-processed SWAT-NAIP model after specifying a 4-year warm-up period.	180
Figure 61. The simulation result of the SWAT-LANDSAT model validation with the calibrated parameter set 8 from the calibration of the model.	181
Figure 62. The simulation result of the SWAT-NLCD validation with the calibrated parameters obtained from the literature.....	182
Figure 63. Verification simulation of the SWAT-NAIP model with the parameters obtained from the default model calibration parameter set.	188

Figure 64. Simulation result of the second half of the verification period.....188

Figure 65. Before (above) and after (below) the simulation of the juniper removal.192

LIST OF TABLES

	Page
Table 1. Band properties of Landsat 5 and Landsat 8 images used in this study.	36
Table 2. Information about the weather stations.	38
Table 3. The LULC classes and their areas mapped and calculated by NLCD 2011 for the study area.	49
Table 4. Description of the NLCD land use cover classes within the study area	50
Table 5. Land use cover for the study area derived from TEAM dataset	52
Table 6. Training data pixel counts for aerial image classification.....	63
Table 7. Improvement in spectral separability by addition of NDVI and Texture.	66
Table 8. The number of total pixels included in training data for each type of class by different years of Landsat 5 and Landsat 8 images.	70
Table 9. Separability analysis of training data collected for Landsat image classifications.....	72
Table 10. Area of each land use and cover class in different years computed by using the initial classifications.	75
Table 11. Area of classes for two 2014 ML classifications performed using differently collected ROIs.	81
Table 12. Initial statistics of Landsat ML and SVM classifications.	82
Table 13. Area of each class for every Landsat image ML classification after water pixels are edited.	85
Table 14. Sample confusion matrix for the accuracy assessment of a classification.	86
Table 15. Number of validation pixels collected for the accuracy assessment of Landsat image classifications	89
Table 16. Preliminary validation pixels collected before editing shadows in the aerial image classifications.....	90
Table 17. Final accuracy assessment results of the Landsat image classifications.	91

Table 18. Initial accuracy assessment results of aerial image classifications.	92
Table 19. Number of ground truth points collected from shadowed areas.	99
Table 20. All SWAT models set in this study.	108
Table 21. Class names and values of the produced thematic maps and corresponding SWAT LULC codes.	111
Table 22. Biophysical parameter database of the juniper.	112
Table 23. Slope classes generated for land use/soil/slope definition.	115
Table 24. The absolute range and definitions of the 15 parameters.	122
Table 25. Manual calibration processes summarized in this table.	125
Table 26. Default and adjusted parameter values for manual calibration iterations.	127
Table 27. The model results of manual calibration iterations. Each iteration has a single simulation.	129
Table 28. Hydrological soil groups and associated soil classes included or excluded in the HRUs in the watershed.	130
Table 29. Model Performance Evaluation Criteria. Adapted by Moriasi et al., Van Liew et al. and Fernandez et al. [46, 79, 80].	134
Table 30. Land use and land cover in the study watershed before and after hypothetical brush management.	139
Table 31. The statistical relationship between precipitation and elevation.	143
Table 32. Measured annual water yield by years and its ratio to interpolated annual rainfall.	144
Table 33. The statistical relationship between IDW and PRISM annual precipitation.	144
Table 34. Results of the hydrograph separation analysis.	145
Table 35. Accuracy assessment of the shadow identification method.	147
Table 36. Areas of classes detected within the shadowed areas and remaining unidentified shadow areas.	148
Table 37. Final accuracies of the NAIP ML image classifications.	149

Table 38. Accuracy of the higher-resolution maps before and after shadow editing.....	150
Table 39. Percentage of the area of each LULC class across the years.	151
Table 40. The results of change detection analysis reported in percentages for aggregated and original thematic change.	154
Table 41. Results of thematic change detection analysis reported in area.	155
Table 42. Multiple regression results of annual precipitation, tree cover, and water	160
Table 43. Linear regression of water yield on rainfall (top) and tree cover (bottom)....	161
Table 44. Area of each land use and cover class mapped using higher-resolution aerial images inside the community-level classes of the NLCD 2011 dataset.	165
Table 45. The results of the sensitivity analysis conducted by following the automatic calibration of previously adjusted parameters.	167
Table 46. Pre-Processed and default SWAT-NAIP Calibration Results.....	168
Table 47. The best parameters of the pre-processed SWAT-NAIP calibration from iterations 7 and 8.....	169
Table 48. The best parameters of the iteration 7 for the default SWAT-NAIP calibration.	173
Table 49. Calibration results of the SWAT-LANDSAT model.....	175
Table 50. Validation results of the SWAT-NAIP models for the data period of 2016-2017.	177
Table 51. Validation results of the SWAT-LANDSAT and SWAT-NLCD models.	177
Table 52. Parameters based on two previous studies used for SWAT-NLCD model validation. Adapted by Jain et al. (2015) and Qiao et al (2015).....	181
Table 53. Whole verification period modeling results.	186
Table 54. R ² value obtained from the SWAT-NAIP model for the second half and last year of the verification period.....	187
Table 55. Results of the benchmark and scenario models.	190

CHAPTER I

INTRODUCTION

I.1 Background of the Study

Drylands, categorized and defined according to the ratio of average annual precipitation to potential evapotranspiration by the United Nations Convention to Combat Desertification (UNCCD), cover approximately 35-47% percent of the world's terrestrial area [1-4]. According to the Dryness Index described by the UNCCD, which is also called the dryness index with its value ranging from 0 to 1, drylands fall into the range of 0.05 to 0.65. Arid, semi-arid and sub-humid areas are the classes of drylands and have different dryness index intervals [5]. Only semi-arid and sub-humid regions are suitable for agricultural practices while some irrigatable places are also arable. The residents on drylands make up around one-third of the total world population [1, 4]. Increasing pressure has been exerted on these lands due to intensified changes originating from natural phenomena and human activities following the industrial era [6]. Increasing warming climatic conditions are expected in these areas due to exponential and persistent greenhouse gas concentrations, especially carbon dioxide emission, in the atmosphere[3]. Although some scholars see an opportunity to sequester extra carbon in drylands, water conservation has become another debated issue, especially in semi-arid regions[7-10].

Drylands are predominantly used as rangelands. Agricultural production, historical fire pressure, urbanization, and overgrazing have been the most prominent

drivers for local, landscape, and regional-level changes in the dryland ecosystems [11]. Invasions of exotic species, alteration of streamflow regime, and degradation of soil are notable consequences of these changes worldwide. Texas has very diverse ecological regions and climates due to its widespread territory. While Southeastern part of Texas is more humid, Northern and particularly Midwest are much drier. The Edwards Plateau in west-central Texas is a significant semi-arid ecoregion. Some prominent rivers of Texas like Colorado, the Guadalupe and the Nueces Rivers have their headwaters in the ecoregion [12]. The watersheds in the plateau are of crucial importance because the water from these watersheds is drained into the Edwards Aquifer which is the primary water source for Austin and San Antonio as well as many other municipalities [13].

Accelerated increases in the human population around the region have sparked more demand for water for agriculture, industry, municipalities and for maintaining environmental flows in the rivers [14]. Shrub encroachment in the plateau has long been considered as a significant issue due to its large scale of land cover and high-water consumption[9, 15]. Following the European settlements, cattle numbers increased dramatically in the region[12]. Change in the fire regime has also provided a suitable environment for shrub establishment in the landscape [12]. Since water is the most important scarce resource in the drylands, statewide programs were initiated by the support of state Senate. In 1985 Texas Senate passed the State Agriculture Code (Bill 1083) which enables the clearing and reduction of invasive brush species like mesquite, prickly pear, salt cedar or other phreatophytes exploiting water available in the soil to the extent to become a threat to water conservation [9]. A considerable amount of research

has been conducted so far to identify the impact of shrub encroachment on local and regional hydrology[10, 12-14, 16-20]. Although higher interception and transpiration from woody plants are widely accepted, existing research results aren't always consistent in terms of streamflow generation. According to a study done on different sites of the Edward Plateau, daily water consumption of redberry juniper, Ashe juniper, mesquite, and live oak varies from 19.1 to 46.8 gallons per tree per day, while live oak consumes the least and redberry juniper consumes the most[15].

Many studies showed that there is a significantly-augmented streamflow following brush management practices. Thurow in 1988 proposed that brush management can produce desirable consequences as long as the amount of annual rainfall surpasses the 450 mm threshold[21]. Wilcox and Huang in 2010 analyzed 85 years of streamflow and its relationship with land use and cover (LULC) and found out an increase in the streamflow of three watersheds, Nueces, Frio, and Upper Guadalupe although the shrub cover has increased. They attributed this outcome to improved range conditions following a recession in the grazing pressure, eventually allowing continuous cover of rangelands by shrubs and native grasses which led to augmentation in the infiltration capacity of the soil. This result was counterintuitive given the fact that general acceptance of the negative impact of woody vegetation on the streamflow. Another study in the Edwards Plateau by Dammeyer et al. in 2016 pointed out the presence and importance of epikarst which is considerably effective for deep storage of water for a long period under the root zone of juniper species[22]. Counterintuitively, the live oaks which selectively remained on the brush removal site may exert a more severe

impact on the water budget because they have deeper roots than Ashe juniper and can access to stored water in the epikarst layer. They concluded that although the immediate response of recharge is relatively higher after brush control operation, previously available water content and subsequent extreme precipitation events can make the difference in terms of water yield. Many of these experimental studies covered a small scale of the region and thus it is unknown if the impact of shrubs in these areas can be upscaled to a larger part of the region. Because LULC alterations are usually more complex and heterogeneous in larger catchments along with the fact that change may often happen in a small proportion of the total area, finding control catchments beyond the headwater scale is usually quite difficult[23]. Modeling studies, on the other hand, have the potential to represent a larger area using all essential variables and an integrative multidisciplinary approach.

The Soil and Water Assessment Tool (SWAT), a physically-based semi-distributed model developed by the joint efforts of the United States Department of Agriculture (USDA) and Texas A&M University is widely used to estimate the impact of land management and natural events on water quality and quantity [24]. The model divides a basin into many sub-basins connected by a stream network before further delineating the sub-basins into Hydrologic Response Units (HRUs) which reflects the unique combinations of LULC and geology in the sub-basins [25]. The model has the advantage to allow for readjustment of the LULC data and to enable the researchers to investigate the impacts of woody plant cover on the watershed hydrology. Recent studies simulated the effect of brush cover on the streamflow and concluded that an increase in

the surface runoff and streamflow occurs especially following the removal of the dense canopy of brush stands [26, 27].

However, these modeling studies often focused on the augmentation of streamflow. Relatively fewer studies were conducted to demonstrate the accompanying impact of increased streamflow by the contribution of boosted surface runoff due to the removal of woody vegetation. Soil erosion is also a significant factor which contributes to the degradation of drylands. A few modeling studies conducted in drylands of Africa and Asia indicate a strong positive relationship between storm flow and soil loss.

I.2 Problem Statement

The studies reviewed above have generated important results on the relationship between brush cover and the hydrology of watersheds in the Edwards Plateau. However, these studies also have limitations. Although modeling studies offer a more comprehensive approach to the analysis of impacts of vegetation management practices on water budget, the incomplete representability of the study area by input data like LULC, climate, and geology is an important limitation. For example, utilization of a single LULC dataset for lengthy periods may neglect some land use and cover changes which may lead to more biases in the model outputs. And, the increments in the impervious surfaces like urban and barren areas would lead to an enhanced surface runoff. Besides, other types of vegetation like oak trees and herbaceous species may also have substantial effects on the hydrological cycle.

Hence, the classification approaches which don't consider these LULC classes may have the potential to overestimate or underestimate the impact of brush cover on the

water yield. Another constraint is the availability and utilization of high-resolution spatial data. For instance, digital image classifications from Landsat satellite images having a 30-meter spatial resolution usually may have to cope with mixed pixel problems. Such coarser resolution imagery may lead to a classification in which an area covered by sparsely distributed trees can be depicted as heavy woody vegetation.

Another point to note is the simulation of moderate and heavy shrub conversion to native grass. In reality, removing the whole moderate and heavy shrub cover can bring about significant environmental problems. Most of the heavy shrub cover is found on steep slopes. Removing this cover possibly makes these areas more vulnerable to soil erosion and flash flooding [25].

Models like SWAT can easily incorporate the variations in precipitation, temperature, and evapotranspiration(ET). This can compensate for the limitations existing in paired catchment studies. Assessing the impact of land cover on hydrology within the borders of the same watershed can be more practical than comparing two small catchments (<1 square km) with similar climate, geology, and land cover and using one catchment as treatment and the other as the control. Although the SWAT model can assess the dynamics of vegetation species for different years by the Potential Heat Unit parameterization, the model cannot account for all LULC changes if it isn't fed by the land cover data. Furthermore, it is highly possible that there are ongoing brush management operations on the plateau, which need to be accounted for as well.

I.3 Research Hypotheses

H1: Brush management led to LULC change in the Nueces Headwaters watershed during the 2008-2017 period.

H2: Thematic map accuracy improves with the incorporation of different sensor data and classification algorithms.

H3: The effect of brush management on water yield is significant.

I.4 Objectives

The goal of this study is to assess the impact of the land use and land cover change on streamflow in the Nueces River Headwaters Subbasin, Edwards Plateau, Texas. The specific objectives of this research are to:

- i. assess the practicality and accuracy of mapping land use and land cover by using high-resolution National Agricultural Imagery Program (NAIP) images;
- ii. use multi-sensor, multi-algorithm and ancillary data to detect shadow areas and improve classification accuracy;
- iii. quantify land use and land cover change from 2008 to 2017, and
- iv. simulate the impact of brush management on the streamflow in the Nueces Headwaters Subbasin.

CHAPTER II

LITERATURE REVIEW

II.1 Brush Encroachment and Management on the Edwards Plateau

The Edwards Plateau is geologically a karst dominated semiarid ecoregion in Texas. The characteristics of the plateau support the formation of abundant springs which feed the streams and enables a substantial amount of water to be stored in the underground aquifer systems [28]. While the area was mainly covered by native savanna grass, following the European settlements, the landscape had undergone a series of state changes including, in particular, the change from native herbaceous vegetation to the brush species[13, 29]. This change in the land cover configuration of the plateau concerned local and regional authorities and prompted researchers to conduct studies to reveal the impact of conversion from grassland to the brush dominated environment on the water resources of the region. The need for better understanding of plant water interactions on the plateau comes from the crucial importance of the Edwards aquifer which has been a very reliable source of water for several cities and municipalities in Texas[13]. The main drivers for the transformation of the landscape are mentioned to be overgrazing following the first European settlements and alterations in the natural fire regime[12]. Among the other invasive brush species, Ashe juniper is reported to be more common on the plateau. It's high transpiration and interception values were documented by Owens and Ansley[15].

Bednarz et al. prepared a feasibility report in 2000 to document the possible results of brush management applications to inform the Texas State Soil and Water Conservation Board[30]. According to the report, there was great potential to increase water yield ranging from 13,000 to 172,000 gallons for each treated acre in the eight Texas watershed where the effectiveness of brush management simulated using the Soil and Water Assessment tool. Several modeling studies followed Bednar's study in varying watersheds on the Edwards Plateau. From these studies, Wu and Afinowicz reported significant water yield potential in Cusenbary Draw and North Fork Guadalupe River watersheds respectively[13, 16]. In contrary to these modeling studies, studies relying on observation and experiment data have counterintuitive results[12, 20]. Wilcox et al. reported that brush management can yield more water as long as the 500 mm precipitation threshold value is crossed which is first defined by Thurow and when the geology of the landscape allows spring formation. They elucidated that in the locations where soils are deeper and there are no subsurface conduits which are connected to springs, there are little if any benefits related to an increase in water yield following the brush management.

II.2 Using Remotely Sensed Data for Mapping LULC and Change Detection

Land use and land cover is an essential variable in studies related to management of water resource management, flood prediction, soil degradation, and nutrient loss assessment, and biodiversity conservation [31, 32]. It is one of the significant factors affecting the hydrological responses of an ecosystem. That's why an accurate mapping of the LULC is a very important prerequisite to comprehending the influence of

vegetation on streamflow generation processes. However, there are some limitations associated with investigating the impact of LULC on the hydrological processes [33]. Paired catchment studies have been conducted to demonstrate that the impact of LULC on site hydrology is not capable of representing catchments usually larger than one square kilometer because of the high heterogeneity in biogeochemistry and climate of the area [23]. Because finding suitable control catchments is not feasible in large catchments, change detection analysis could offer a decent approach to cope with the analysis of the impact of LULC change [34]. The methods selected to map LULC is decisive to evaluate its effect on streamflow more accurately. Recent developments in Remote Sensing is very promising and attractive. Remote Sensing is a science of extracting information from the various features on the earth by utilizing electromagnetic radiation as a tool of interaction [35]. While the information related to objects may be derived by simple visual interpretation of remotely sensed images, it is usually acquired from the classified images. Image Classification is the process employed to produce thematic maps from images and facilitates the extraction of information [35]. It is defined by Khatami et al. as the process of transforming remotely sensed imagery into useful products [36]. Classification of remotely sensed images offers a timely and more affordable way of producing LULC maps of large areas. While traditional methods require long field campaigns and very hard work in addition to prohibitive costs, remote sensing technologies can produce more accurate outcomes in a shorter time with less money and effort [37].

The primary steps involved in the image classification process are selecting a suitable classification scheme, making radiometric and geometric corrections, collecting representative training samples, determining the classification method, conducting post classification processes, and assessing the accuracy of classification. The way that these steps are implemented is critical in terms of the success of any classification.

Availability and quality of data is oftentimes the most important limiting factor which is decisive in the accuracy of thematic maps. Using coarse resolution images like images from Landsat brings about mixed pixel problems. That's why interpreting objects successfully from coarse resolution images is often complicated. The intensity of the problem is usually more obvious in relatively heterogeneous areas such as urban and the areas where two or more land use cover classes intersect [35].

Classifications can be conducted in either a supervised or unsupervised format. Training samples are required to run a supervised classification. To produce highly accurate thematic maps, the selection of a suitable classification algorithm and the quality and quantity of training samples are the two crucial prerequisites. Classification methods can be split into two categories based on their spatial level (pixel level, sub-pixel level, and field level) and whether they are parametric or nonparametric. Maximum Likelihood and Minimum Distance methods are two of the most commonly used parametric methods. They have supervised classification methods. K-means and Isodata which is the modified version of K-means are two frequently used unsupervised classification methods. Without requiring training samples, unsupervised classification methods produce spectral classes after a predefined number of iterations. This is an

advantage if there is no prior extensive knowledge on the objects of the area of interest. Another advantage of this unsupervised classification approach is its potential to detect unique features in the study area which may have not been observed formerly. However, to produce a thematic map, users need to examine and combine spectral classes into information classes.

Non-parametric classifiers like fuzzy logic, neural network, decision tree, and knowledge-based classifications have been used more frequently in multisource data classifications. The fact that they don't assume the normality of the training data which is considerably difficult to obtain in heterogeneous landscapes is an important advantage compared to parametric classification methods [35]. However, they are computationally intensive and oftentimes requires sufficient ancillary data. Due to the data availability, and acceptable accuracy in most cases and user-friendly nature, Maximum Likelihood is often preferred by researchers to produce thematic maps from aerial and satellite imagery. While classifying an unknown pixel, the maximum likelihood method assesses the variance and covariance of spectral responses from training samples. It is a supervised and parametric classification method [35, 38]. With the Gaussian Distribution assumption, the mean vector and covariance matrix can define the category response pattern. Considering these parameters, the statistical probability which determines the memberships of pixels for different classes can be computed [39]. Many studies benefited from using the maximum likelihood classification to map LULC and analyze the changes in LULC and used the classification and change detection outputs to explain

the impacts of LULC change on ecosystem processes such as hydrology and biodiversity [26, 27, 40].

An LULC dataset is a significant input for modeling studies. Current and possibly future trends in deriving LULC data are the utilization of remotely sensed images. The accessibility, cost, and availability of the images are some of the primary decisive criteria in the selecting images for performing an LULC classification analysis. However, there are always important tradeoffs between satellite and aerial images while deciding which images to use. Landsat images are quite widely used in mapping vegetation cover to investigate the effect of vegetation change on the hydrology of watersheds [26, 41]. Landsat offers free satellite images to users in a 30-meter spatial resolution for the visible and near and mid-infrared bands. Landsat 7 and Landsat 8 images have also thermal infrared bands having a 100-meter spatial resolution. The satellite revisits time is 16 days. The spatial resolution of Landsat for color infrared images is coarse and the utilization of Landsat images is mostly suitable for community-level classifications. However, accurate individual object level classifications cannot be accomplished by Landsat based classifications alone.

While classification of remotely sensed images into thematic maps offers an outstanding opportunity to conduct environmental and socioeconomic studies in a cost-effective and timely manner, it is still challenging due to the factors like complexity of the ecosystem components in the study area, selected remotely sensed data, image processing and classification techniques which may impact the overall and individual class based accuracies of a classification approach [42]. In a literature review of pixel-

based land cover image classification processes, Khatami et al. (2016) found that Support Vector Machine (SVM) classification produced more accurate results than other classification algorithms [36]. According to their meta-analysis, the inclusion of texture into the classification process is the most effective method for the enhancement of classification accuracy. Unlike the Maximum Likelihood Classifier, Support Vector Machine doesn't need to assume the normality of the training data. Although this is an important advantage of non-parametric classifiers, because when a landscape is complex, parametric classifiers may potentially produce noisy results, non-parametric classifiers such as Support Vector Machine and Neural Networks often require adequate expertise knowledge and ancillary data to perform a successful classification. Furthermore, they are computationally intensive compared to the Maximum Likelihood classification which has been used as a benchmark classification method for the analysis of LULC.

II.3 Soil and Water Assessment Tool (SWAT) in Hydrological Analysis

The SWAT (Soil and Water Assessment Tool) model is a process-based hydrological model which is capable of simulating physical processes taking place in river basins in a daily time step [43]. It is developed to analyze the impacts of land management practices on watershed processes. The model is able to simulate water, sediment and nutrient transport in watersheds and large basins under dynamic climate, soil, land use, and cover, stream network features and agricultural activities [24]. It currently works on two GIS (Geographic Information System) platforms: ArcGIS and QGIS. While ArcGIS is a licensed program QGIS is a public domain GIS platform. The

SWAT model requires spatially and temporally distributed datasets as inputs to the system. Within SWAT, a digital elevation model (DEM) is used to delineate a study area into watersheds and create the stream network. Soil and LULC datasets are the other two spatial datasets required by the model. The model has built-in weather data for the United States, currently available up to 2014. Daily precipitation and temperature data are the two most significant weather data to input the model.

The SWAT model has been used worldwide and arguably the most cited hydrological model so far. Although the model's preliminary objective is to predict the outcomes of management on water, sediment and agricultural activity driven nutrient generation in large ungaged basins without requiring the calibration of the model, the availability of the observed data and autocalibration software like SWAT-CUP urge researchers to calibrate models. Therefore, it is possible to divide a modeling study into three interconnected phases: calibration validation, and simulation. USGS (United States Geological Survey) streamflow monitoring gages offer reliable data within the USA which has been very helpful for researchers investigating the impact of land management and climate change on the hydrological processes. The streamflow data is mostly used observed data for assessing the accuracy of a model's result.

Being a physically based model it also comprises empirical components [44]. The fact that a considerably high number of parameters are used in the SWAT makes it a very complex model [45]. The parametrization of the hydrological components of the system determines the accuracy of the simulations. Parameters used in the SWAT model have an uncertainty range. The interval for the parameters can depend on the

experimental data, expert knowledge, and literature. Keeping these process-based input parameters within a realistic uncertainty range is crucial [43]. As an initial step, determining the most sensitive parameters before calibration and validation are recommended [43]. In SWAT-CUP two types of sensitivity analysis can be performed: one at a time and global sensitivity analysis. While a lot of initial simulations are needed for global sensitivity analysis, the interaction between different parameters cannot be explained by one at a time sensitivity analysis [43]. Calibration of the model can be performed both manually and automatically. Automatic calibration is mostly favored due to the convenience of use and less labor and time compared to manual calibration. The criteria of the accuracy for a model was described by Moriasi et al [46]. Nash-Sutcliffe efficiency (NSE), percent bias (PBIAS) and coefficient of determination (R^2) are the three most used statistics to express the uncertainty of the simulated results. According to Moriasi et al. NSE should be equal to or greater than 0.5 to accept a model's output [46].

A few studies used the SWAT model to examine the impacts of shrub encroachment and brush control on the water yield of watersheds in Texas [16-18, 30]. In a recent study, Qiao et al., (2015) modeled the impact of woody plant encroachment on watershed hydrology [18]. They calibrated SWAT model based on the observed parameters they obtained from three small (2 to 5 ha) paired catchments in Oklahoma. They validated the calibrated model in the Council Creek Watershed which is 78 km² and about 30 km from the experimental catchments. They also investigated the prolific invasion of juniper species in the region. They argued that antecedent studies like

Afinowicz et al. (2005) had substituted biophysical and hydrological parameters of juniper species (Ashe juniper at Edwards Plateau and Juniper virginiana at Council Creek watershed and experimental catchments) with evergreen forest or pine parameters since they are not readily available in the SWAT model database. They also compared the results of water yield estimations of Wu et al. (2001) and Afinowicz et al. (2005). While the SPUR-91 model used by Wu et al. estimated a reduction of about 200 mm in actual evapotranspiration (ET_a) as a result of clearing 40% of the woody vegetation in the Cusenbary Draw watershed, the SWAT model used by Afinowicz et al. predicted about an increase of between 31.9 and 46.9 mm in water yield with a scenario of removing all heavy and moderate brush cover on North Fork of the Guadalupe River watershed [13, 16]. They argue that the inconsistency in the estimations of water budget may have stemmed from the misrepresentation of hydrological processes due to inadequate calibration of the model parameters. They emphasize that plot-level or experimental-catchment-level observations are crucial importance to understand the residing mechanisms of tree and shrub invasions on the elements of the hydrological processes. However, according to them, process-based modeling studies can be a more effective approach to accessing the ramifications of brush encroachment at larger scales with more diverse land use and cover and climate.

The study by Qiao et al. demonstrated the effectiveness of the incorporation of experimental and modeling studies. They used in-situ surface runoff data and in-situ soil moisture data during the conditioning process of simulated results to the observed data. They underlined that the issue of parameter compensation and non-uniqueness may lead

the model calibration algorithm to produce irrational or unrepresentative parameter sets for watershed ecohydrological processes[18]. They pointed out that streamflow data is predominantly used for model calibration and validation since the availability of data is very limited beyond small-scale experimental watershed studies. However, they cited that incorporation of multiple water (e.g. streamflow, soil moisture) and energy variable measurements (e.g. ET, soil temperature, biomass) is a proved approach to curb degrees of freedom and parameter uncertainty due to the challenge to relate streamflow to the ecosystem state changes such as shrub encroachment. According to the criteria described by Moriasi et al. (2007) for evaluating the accuracy of modeling studies for water quantity and quality, their study achieved very good uncertainty estimates in terms of both daily and monthly statistics [46]. Although NSE statistics were about 0.9 for monthly estimations of a model for paired catchments, the value of NSE was around 0.8 for the validation model. They attributed this small reduction to the uncertainty involved in the climate data for the larger watershed (78 km²). As a result of their modeling study, they reported that an average of 100 mm more ET_a was released from juniper encroached plots compared to grass plots within the study period (2011-2013). They claimed that the biophysical and hydrological parameters produced by their study are the first complete and reliable parameterization for invading juniper species.

One of the most recent studies investigating the influence of brush management on watershed hydrology in Texas was by Jeremy White and others in 2017. They analyzed the importance of parameterization in providing robust uncertainty estimates from models simulating the feasibility of the brush management options used by

resource management decision makers [17]. The area they modeled was within the Edwards Plateau in Southern Texas. The size of the watershed modeled by them was very small (1.4 km²). Their study area has characteristics of karst geology which is specific to the Edwards Plateau. The study period covers the years from 2001 to 2010. They constructed two discrete models one for the 2001-2003 period and the other is for the 2004-2010 period. They called these two models as “conditioning” (pretreatment) and “forecast” (post-treatment) respectively since 40% of the Ashe juniper was cleared mechanically in 2004.

According to them, the uncertainty of the model outputs is usually coupled with the potential uncertainty naturally included in the model input datasets like weather, soil, DEM, and LULC. Thereby, evaluating the uncertainty of simulated results of LULC change is quite significant especially when the results are needed to inform decision-making processes [17]. They specified two sets of parameters to calibrate models for uncertainty estimation: reduced parametrization and full parameterization. For the reduced parametrization, they selected 12 mostly used SWAT parameters from the literature which are used in the hydrological analysis of the land use management and they adjusted these parameters in the watershed scale meaning that every hydrologic response units (HRUs) in the watershed had the same value. For the full parameterization, they populated these 12 parameters in the HRU scale accordingly which resulted in 1305 adjustable parameters.

They concluded that both types of parametrizations were able to yield satisfactory results in the estimation of average daily streamflow. However, the

estimation of the difference in total volumetric ET which is a pivotal measure for assessing the outcomes of brush control remained highly uncertain, especially for the reduced-parameterization model.

Another recent study conducted by Jain et al. on the Nueces River Headwaters watershed investigated the impact of land use cover change on watershed hydrology. *Arundo donax* which is an invasive warm-season perennial grass began replacing native switchgrass in the riparian areas of the Nueces River for the past a couple decades [47]. Although the invasion occurred in specific locations they had to model an area of 2126 km² to calibrate the model with the observed streamflow data which was collected by the USGS gage at the watershed outlet. After the watershed delineation by the SWAT model, they located the areas of *Arundo donax* within the HRUs. Thus, they reported that seven HRUs along the river were identified. Since there were no *Arundo donax* biophysical and hydrological parameters prior to their modeling study they modified sugar cane parameters to represent *Arundo donax* in those seven HRUs. They divided the time-horizon into two periods: the pre-invasion period from 1979 to 1994 and the post-invasion period from 1995 to 2010. To reflect the high water, use of *Arundo donax*, they simulated irrigation from the river. Unlike the former Edwards Plateau hydrological modeling studies, they located and marked the losing streams, sinkholes, and springs which had characteristic geological features of the karst affected watersheds. Thus, they were able to isolate subbasins with no sustained flow from the subbasins which have springs and sinkholes. They pointed out that, modeling the hydrological components of the water budget is more complex in watersheds underlain by karst due to the fact that

the distribution of karstic features varies significantly within the watershed. To represent the distinctive features of subbasins they defined different adjustable parameters for those subbasins. They reported very good NSE values for the uncertainty estimation of the model. The NSE value was 0.79 and 0.74 for the calibration and validation of the SWAT model respectively. The R-square was 0.76 and 0.64 respectively for calibration and validation. The P-bias (percent bias) value which is used to evaluate the uncertainty estimation of SWAT model-biases, was 15.5% and 4.3% for calibration and validation respectively. In conclusion, they reported that the water yield was 17 mm lower on average in the seven HRUs where *Arundo donax* encroachment had been monitored.

The SWAT model has also been used to simulate the hydrological processes in karst-dominated watersheds in other parts of the US. Among the studies are Amatya et al and Baffaut et al. [48, 49]. The Chapel Branch Creek(CBC) watershed in the upper coastal plain of South Carolina which is 15 km² in size and underlain by Santee limestone was studied by Amatya et al. [48]. Their study covered a relatively short period: 2006 to 2010. They found that the existence of horizontal and vertical subsurface conduits and voids in the karst affected watersheds can impair the model's capability of estimating the ratio of streamflow components accurately (e.g. return flow, overland flow). They argued that the fewer number of studies on karst watersheds was a result of the complications involved in modeling the groundwater component of the watershed hydrology since groundwater can make dynamic impacts on the surface water flow's magnitude and timing. According to Ghanbarpour et al. (2010), models like SWAT which are configured mostly for more typical watersheds is not able to produce

satisfactory predictions of flow in karst affected watersheds [50]. A similar conclusion was also reached by some other former studies conducted by Jourde et al. in 2007 and Salerno and Tartari in 2009. They both underscored the complexity involved in using surface runoff models to simulate the flow in the watersheds of the karst-affected region because of the potential external water supply from adjacent watersheds and also likely delayed and prolonged contribution of karst subsurface flow to surface flow. Amatya et al. in 2011 calibrated the SWAT model using observation data from multiple gages. The data collected from two main points (SL1 and SL2) draining an area of 589 ha in total, and a location at a cave spring (CS) outlet draining about 1,090 ha were used in the calibration of the model. Based on the previous study they conducted in 2010, they noticed that measured flow data at SL2 and CS (cave spring) gages indicated that a significant amount of surface flow disappeared before discharging at SL2 and probably resurfaced at CS gage. So, while calibrating the SWAT model, they increased the hydraulic conductivity values of the main and tributary channel as a high as 150 mm per hour to prompt the model to simulate excessive transmission loss. Later they utilized a deep aquifer recharge coefficient which is the ratio of the subsurface flow lost from the watershed hydrological cycle. So, they noticed that the calibration of the SWAT model for the CBC watershed wasn't a standard calibration process due to the challenging natural characteristics of the karst watershed. They reported that the calibration results at the CS outlet were improved after adding measured baseflow as a point source input to the model. They explained that the unsatisfactory monthly flow estimations of the model at SL1 and SL2 locations may be attributable to the probable flow routes under the karst

conditions and the interaction with the reservoir water levels at the downstream.

Regarding this outcome, they emphasized that the SWAT model might be more useful for predicting streamflow which is predominantly composed of surface runoff. However, they pointed out that the model predictivity was much better in the estimation of monthly outflow at the reservoir outlet, particularly during wet periods. This may have resulted from the fact that when reservoir levels are high during the wet season, the storage capacity of subsurface conduits is exceeded, and the flow is conveyed as surface runoff.

Using the SWAT model, Baffaut et al. in 2009 analyzed the applicability of modeling hydrological dynamics in karst-affected watersheds in a case study of the James River Basin, Missouri which is a large scale watershed (3600 km²) [49]. Their primary focus was testing how the SWAT model performs in estimations of flow components and water quality when modifications are made to original infiltration and percolation algorithms. They noted that groundwater contamination has higher potential in karst watersheds due to the higher connectivity between surface and groundwater. Plus, anthropogenic activities increase water pollution risk. They described important characteristics of karst watersheds such as sinkholes, losing streams and springs. To simulate the rapid transfer of water through vertical conduits which are specific to karst watersheds, they modified the deep aquifer recharge algorithm by changing the source code of the original SWAT model. A similar approach was taken formerly by Afinowicz et al. [16]. Baffaut et al. examined the estimations of streamflow partitioning into baseflow and surface runoff since there was a notable possibility that groundwater flow

and surface runoff derived from the SWAT may be substantially different from those observed in total streamflow due to the considerable impact of springs, in-stream transmission losses, and discharges from wastewater treatment facilities. They utilized the USGS hydrograph separation method (HYSEP) to check whether the simulated baseflow ratio (baseflow to total streamflow) is comparable to the measured baseflow ratio. They calibrated the model using the data collected from multiple observation points with some of them on tributaries and some of them on the stem of the main channel. They reported satisfactory NSE values mostly around 0.5 while some slightly lower than 0.5 for the calibration of streamflow. According to their results, the values representing the goodness of fit were better on the main channel while the estimations performed slightly poor on tributary channel locations. They attributed this to the possible transfer of water from the upstream of a subbasin to another subbasin with subsurface conduits which connect sinkholes to the downstream or neighboring streams. Although uncertainty estimation statistics performed slightly poorer in validation, they stated that the results were successful since the values were comparable. They reported that prediction efficiencies (the coefficient of determination utilized) for the water quality estimations ranged from 0.33 to 0.97. All in all, they suggested that the modified SWAT model can be a viable solution to simulating complex hydrological processes on the karst affected watersheds.

Looking into the reported parameters used in the calibrations, one can see that there are no identical parameter sets even though the geological characteristics of the watersheds are comparable. According to Bakalowicz (2005), the generalization or

standardization of the methods and results used in the hydrological modeling of karst watersheds is a very challenging task due to the high heterogeneity. Yet, as also seen in the previous works, the approaches used in some studies guided others to evaluate and even to contribute to the existing knowledge of the hydrological modeling of the karst-affected watersheds. However, none of these studies reviewed investigated the impacts of different sources of land use and cover datasets and digital elevation models on the hydrological modeling accuracy of the SWAT. While Amatya et al. (2011) used NAIP (National Agricultural Imagery Program) images and digitized topographic maps to produce a LULC dataset for the SWAT model, Landsat images were used by Baffaut et al. (2009). And, NLCD (National Land Cover Dataset) was used by Qiao et al. (2015), White et al. (2017) and Jain et al. (2015) as the LULC input data to the SWAT model. The NLCD datasets were produced by the Multi-Resolution Land Characteristics Consortium(MRLC) and they are Landsat-derived LULC datasets which are widely used by researchers in the United States. The spatial resolution of the Landsat images is coarse (30 meters). The National Agricultural Imagery Program of the USDA (United States Department of Agriculture), on the other hand, collects aerial images in 1-meter spatial resolution during the active vegetational growth period in order to support resource management decision making in a variety of fields like environmental protection, crop yield assessment, and forest management. The convenience of using available NLCD datasets prompts most researchers to use them as the input LULC data to hydrological models. Because SWAT has the parameters set for NLCD land use and land cover classes in its plant growth and hydrology database, the selection of NLCD

facilitates the model computation of hydrological processes. The DEM data used by previous studies vary considerably. A 1.4-meter lidar-derived DEM was used by Qiao et al. (2015) White et al. (2017) and Jain et al. (2015) used 10 and 30 meters DEMs respectively. Amatya et al. (2011) also used 10-meter DEM while Baffaut et al. (2009) used a very coarse resolution DEM (60 meters). The spatial resolution of DEM datasets is important because the SWAT model delineates watersheds and calculates slopes based on the information provided by DEM. For detecting complex karst features like sinkholes and depressions LIDAR (Light Detecting and Ranging) derived DEMs are recommended for future modeling studies not only for their spatial resolution and ground accuracy but also for their capability of enhancing the modeling accuracy of karst watersheds [49, 51].

There are a few studies conducted to analyze the effect of model input data such as LULC and DEM on the model performance in estimating water quantity and quality for managed watersheds. Fisher et al. (2018) compared the results of two different SWAT hydrological models: one constructed by using 1-meter resolution LULC and DEM datasets and the other built by the utilization of 30-meter LULC and DEM datasets[52]. Their primary focus was on the investigation of the impacts of remote sensing imagery spatial resolution on LULC classification and reliability of water quality modeling. With the high-resolution modeling method, they evaluated the VOI (value of information) which is a measurement of the maximum amount the resource managers are willing to pay for the extra information produced before making a decision. They argued that only a few studies evaluated the cost of varying data types and these studies

usually tended to resample the same source of dataset rather than assessing the datasets at their original resolution.

Fisher et al conducted their study at the Camboriu watershed in Southeastern Brazil. Their study was funded by a local municipal drinking water company (EMASA). The company was seeking for decreasing the cost of water treatment and losses of natural forests due to the replacement by other land uses like crop production which caused high total suspended sediment loads (TSS). Thereby, their mission was to analyze the feasibility of conservation practices in reducing TSS to inform the managers of EMASA. So, they tested the accuracy of modeling both streamflow and TSS loads using two data sources at different spatial resolutions. They recognized that the data acquisition for 1-meter spatial resolution satellite images was quite costly (9,000 dollars) while the 30-meter satellite data were obtained for free from the Landsat archive.

Furthermore, processing high-resolution satellite images would require substantially longer time and more labor (two weeks for the high resolution versus 9 hours for the coarse resolution images). Plus, a lot of disk space was required to process and store the high-resolution satellite image data. However, although the processing and modeling of the high-resolution data were more difficult, they reported a better performance of the model, especially in water quality modeling. They found that the coarser resolution LULC datasets produced from the 30-meter spatial-resolution Landsat satellite images couldn't detect most of the changes because most land use changes took place in smaller patches (less than 900 km²) such as the ones at the forest edge. As a consequence, they reported that there was a 22.8% difference between total area

estimations of land use classes mapped using two datasets. They also underlined the importance of the total area of each land use category and the spatial distribution of each land use in the assessment of water quality. According to them, the SWAT model doesn't quite effectively represent the actual hydrologic processes in the watersheds due to its straightforward process representation which lacks the full spatial connectivity. All in all, they concluded that the spatial resolution of datasets is a decisive factor for both the accuracy of the LULC classification and water quality modeling. They stated that higher resolution imagery increased the accuracy of land use cover maps. They also indicated that the DEM data having a coarse resolution leads to the miscalculation of slope length and steepness. Besides, they found that the 30-meter SWAT model resulted in unsatisfactory NSE values for the larger EMASA watershed. Hence, they suggested that the use of higher resolution input data boosts the reliability of hydrological analysis results.

CHAPTER III

RESEARCH METHODOLOGY

III.1 Location of The Study Area

The Nueces River Headwaters and East Prong Nueces River watersheds are a part of the Nueces Headwaters Subbasin and located within the semi-arid Edwards Plateau Ecoregion. Covered by an important amount of woody vegetation, especially juniper brush (*Juniperus ashei*), this area represents an ideal case to examine the relationship among vegetation cover, soil conditions and streamflow. The study area stretches from Edwards County to the West and Real County to the East. The Edwards County section and Real County section of the study area covers 154 and 197 square miles respectively. Edwards and Real Counties are in the southwestern part of Texas. Rocksprings is the county seat of Edwards County and about 150 miles northwest to San Antonio. Leakey is the county seat of Real County and about 120 miles northwest of San Antonio. Figure 1 indicates the location of the study area, climate stations and the USGS streamflow gauging station.

III.2 Climate, Topography, Land Use and Cover and Geology of The Study Area

The study area carries the common properties of the Edwards Plateau especially in terms of geology, climate, and vegetation. According to the soil survey of Edwards and Real Counties completed and updated in 2000, soils are predominantly very shallow or shallow and used mostly as rangeland [53]. According to this soil survey, croplands,

pastures, and orchards are located on deeper soils usually found on major drainage ways and high divides.

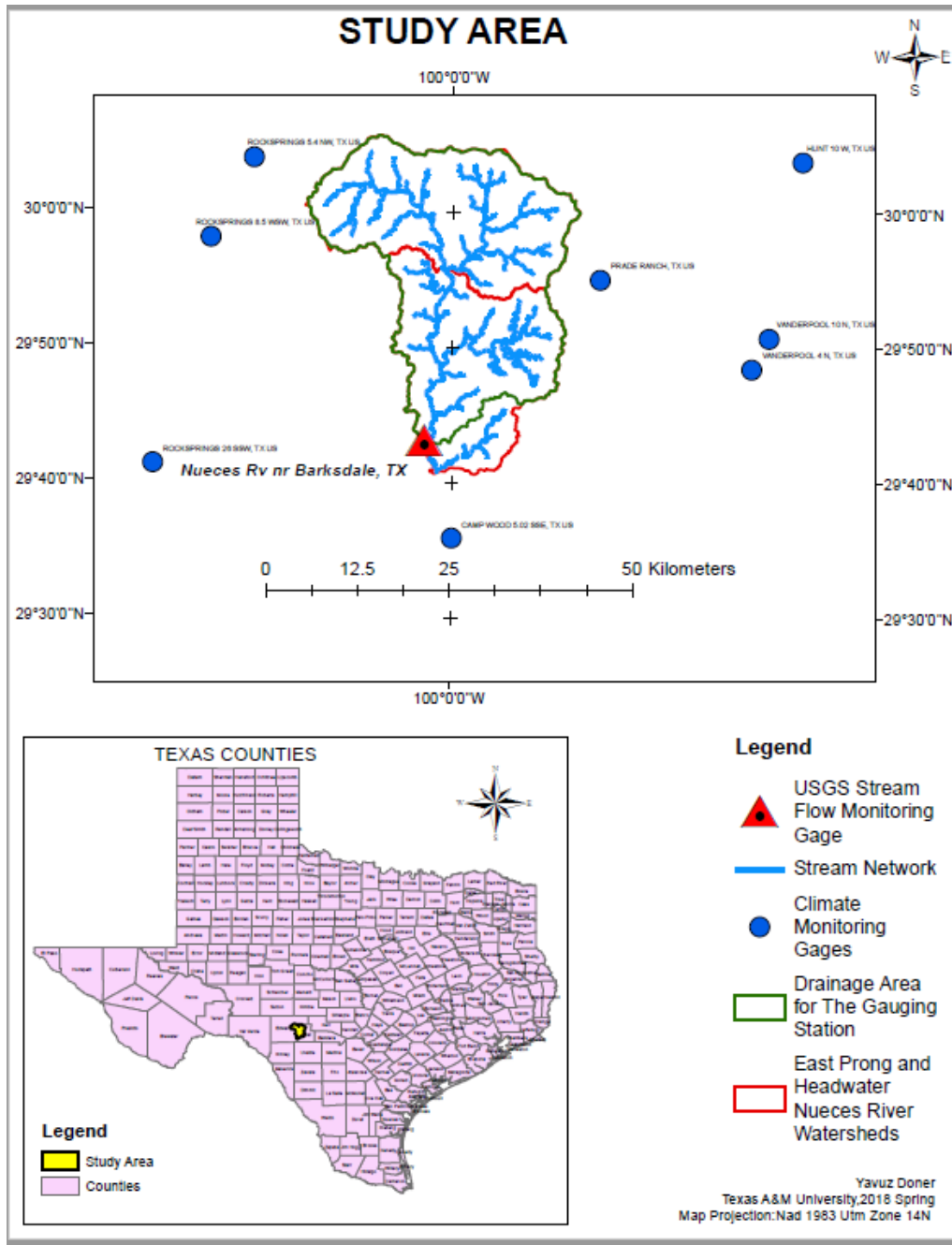


Figure 1. Study area.

The elevation of the study area ranges from 435 to 736 meters above sea level. The 33-year average annual precipitation of the study area from 1984 to 2017 shown in figure 2 is 747.33 mm. However, as shown in the figure 2, the average annual rainfall remained below the long-term average during the study period (608.6 mm for the 2008-2017 period). The rainiest month was May in the watershed area, while February was the month with the least precipitation during the period of study. According to the report obtained from USGS Streamer online application, the total length of the upstream section of the river from the gage is 125.52 kilometers (78 miles). The report described four important streams for the watersheds: Nueces River, East Prong Nueces River, Hackberry Creek, and Bullhead Creek. Figure 3 shows the upstream rivers of the USGS gage. The 2010 total county (Edwards and Real) population was 5.311. Figure 4 indicates the location of the study area, climate stations and the USGS streamflow gauging station.

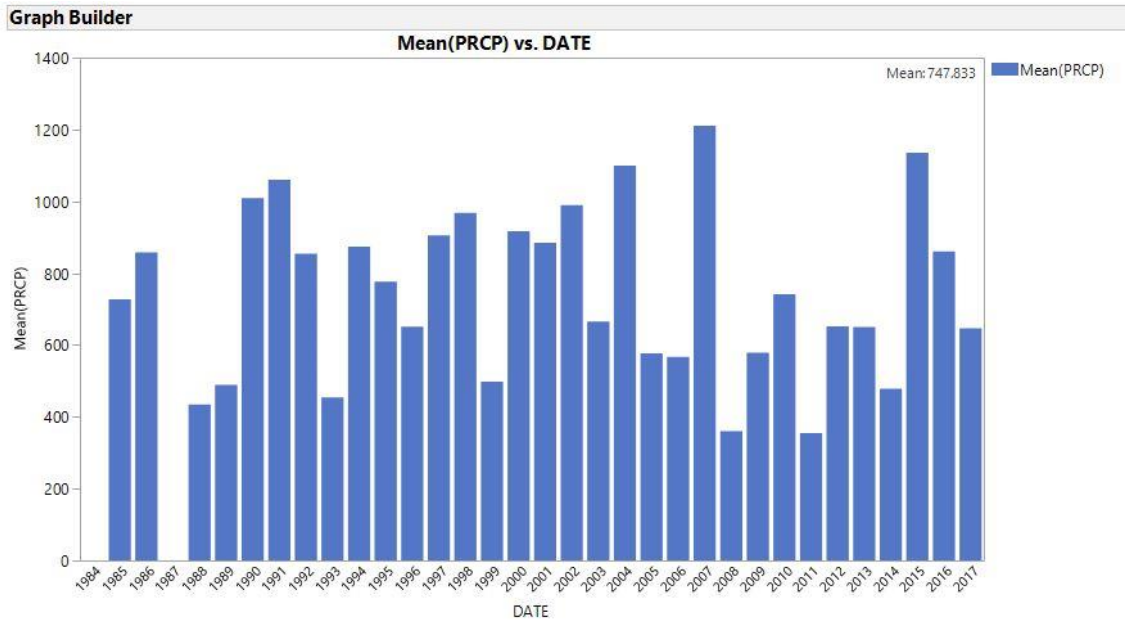


Figure 2. Annual precipitation of the study area from 1984-2017 (data from NCDC).

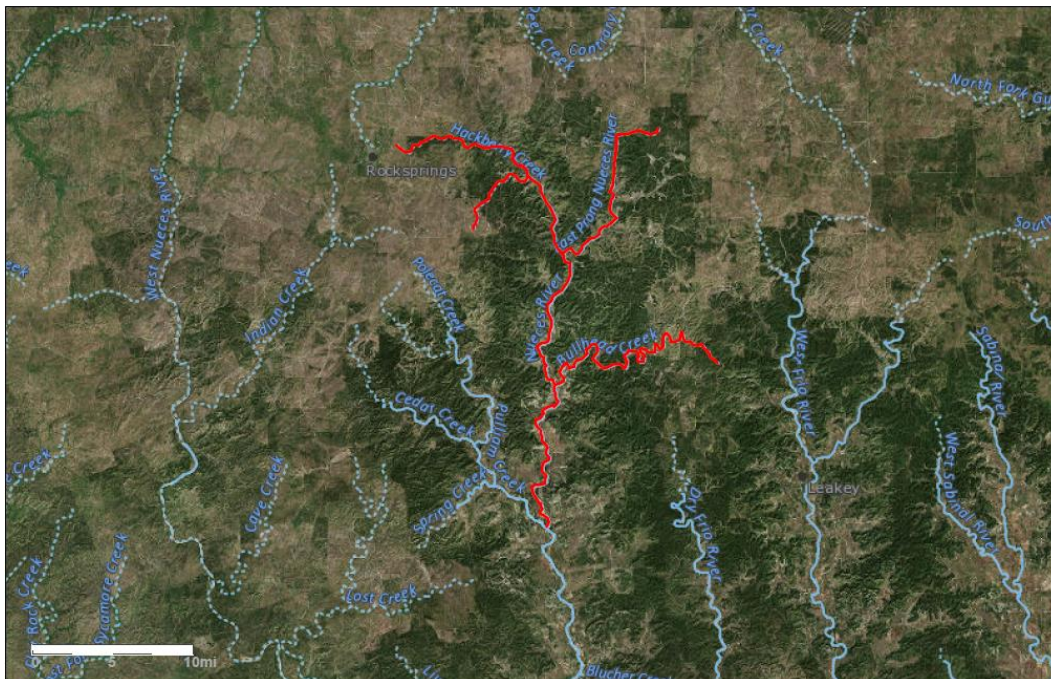


Figure 3. The upstream rivers and creeks of the Nueces Rv Nr Barksdale gaging station. (Source: the USGS Streamer application)

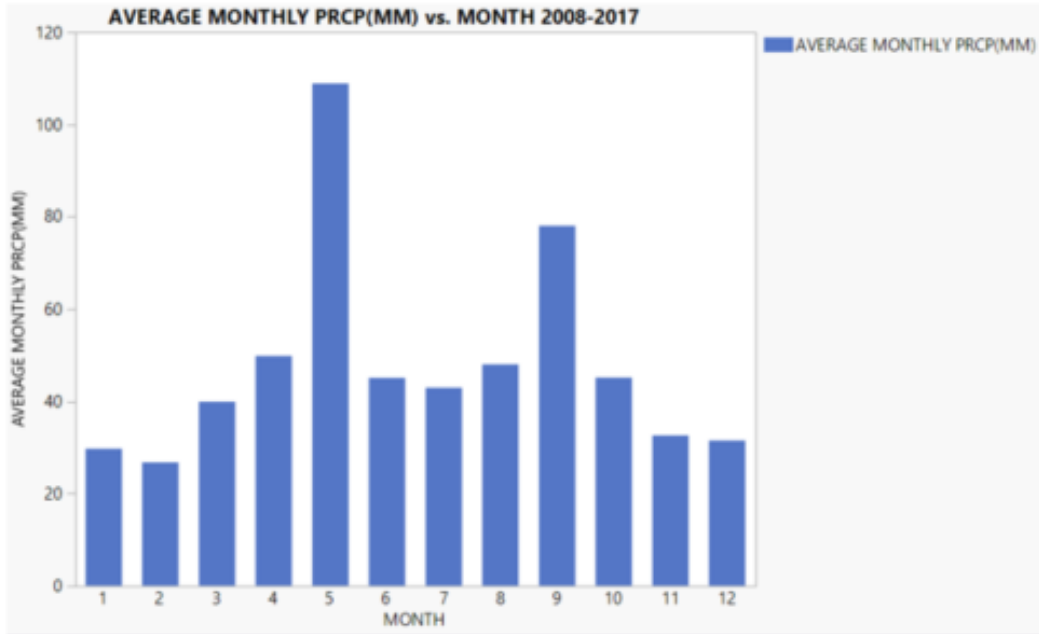
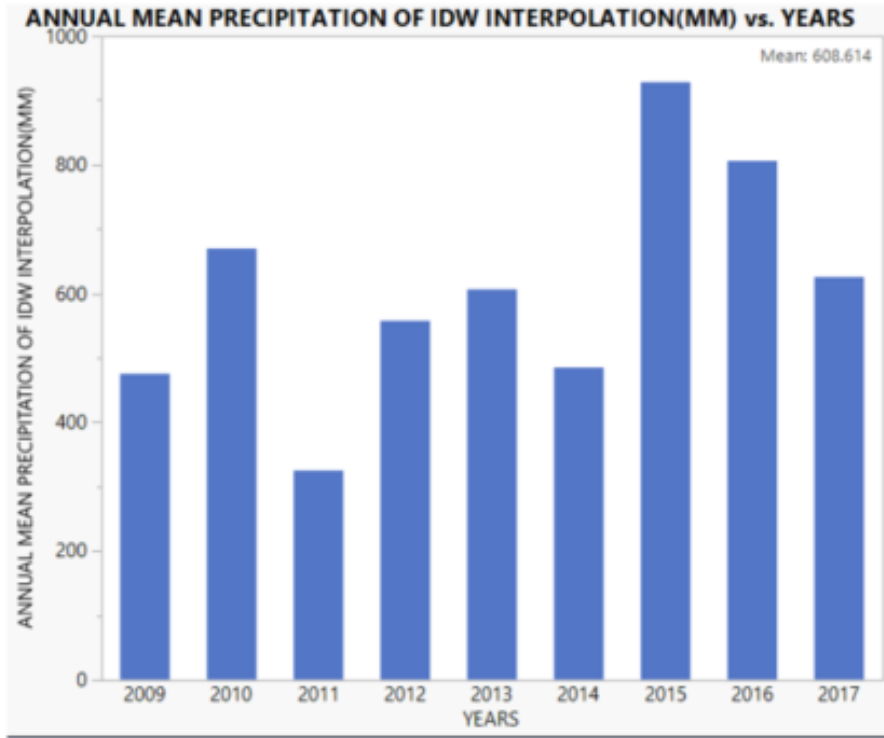


Figure 4. Average annual and monthly precipitation of the study period (data from NCDC).

III.3 Spatial and Temporal Datasets

I obtained both the Digital Elevation Model(DEM2013) and the National Agriculture Imagery Program's (NAIP) and Texas Orthoimagery Program (TOP) quarter quad images of the study area in the raster format from the website of Texas Natural Resources Information System(TNRIS). While the DEM2013 has a 10-meter pixel resolution, the spatial resolution of NAIP and TOP aerial images varies from 0.5 meters to 1 meter. These high spatial resolution digital images have four spectral bands: red, green, blue and near infrared. The digital images are geometrically and radiometrically corrected. These images are collected by the Aerial Photography Field Office (APFO) of the United States Department of Agriculture's (USDA) Farm Service Agency(FSA). The images are captured during the agricultural growing period. I downloaded 14 digital orthophoto quarter quad tiles(DOQQs) which are located within the Real and Edwards counties. The image tiles have a 3.75' x 3.75' quarter quadrangle format with a 300-pixel buffer. Six images were produced between 2008 and 2017: 2008, 2010, 2012, 2014, 2015, and 2016. All images were projected to North American Datum of 1983 (NAD83).

Another DEM dataset used in this study has a 30-meter spatial resolution and was produced by the Advanced Spaceborne Thermal Emission and Reflection Radiometer (ASTER). This DEM dataset was obtained from the USGS Earth Explorer using the online data search tool. Furthermore, two Landsat5 TM (thematic mapper) and four Landsat8 OLI_TIRS (operational land imager and thermal infrared sensor) scenes with path and row numbers of 28 and 39 respectively were downloaded from the USGS Earth Explorer interface. Only the images with no cloud cover were selected. I chose

images that matched or were as close as possible to the image capturing dates of NAIP and TOP missions. Because there was a failure in Landsat 7 ETM (Enhanced Thematic Mapper sensor) which deteriorated the quality of images I had to select Landsat 5 images. Because Landsat 5 mission was terminated before 2012 and Landsat 8 satellite mission began operating in 2013, I had to substitute 2012 with Landsat 8 OLI-TIRS's 2013 image. Landsat 5 images captured by the TM sensor are composed of six spectral bands with 30-meter spatial resolution (bands 1-5 and 7). Band 6 of Landsat 5 images is a thermal band which has a 120-meter spatial resolution. However, the resolution of the thermal bands is resampled to 30 meters by USGS. Landsat 8 images have 11 bands in total including seven spectral bands (1-7), two thermal bands (10 and 11), a panchromatic band (8) and cirrus (9). The spectral and spatial features of the Landsat images were shown in the table 1. The revisit time of both satellites (temporal resolution) is 16 days

The spatial data in NAD83 map projection for the streamflow recording station (Nueces Rv Nr Barksdale) obtained from the United States Geographical Survey's(USGS) National Water Information System (NWIS). Daily, monthly and yearly discharge in cubic feet per second and gage height in feet are available in the interface. The station has been operational since February 6, 2009. Unfortunately, the station didn't measure the suspended sediment levels for the operational period. I downloaded all available daily, monthly and yearly discharge data for the period from February 6, 2009, to December 31, 2017.

Table 1. Band properties of Landsat 5 and Landsat 8 images used in this study.

Landsat 5 TM				Landsat 8 OLI TIRS		
Bands	Names	Wavelength (micrometer)	Res. (meter)	Names	Wavelength (micrometer)	Res. (meter)
1	Blue	0.45 - 0.52	30	Ultra-Blue	0.435 - 0.451	30
2	Green	0.52 - 0.60	30	Blue	0.452 - 0.512	30
3	Red	0.63 - 0.69	30	Green	0.533 - 0.590	30
4	Near Infrared	0.76 - 0.90	30	Red	0.636 - 0.673	30
5	Shortwave Infrared 1	1.55 - 1.75	30	Near Infrared	0.851 - 0.879	30
6	Thermal	10.4 - 12.5	120	Shortwave Infrared 1	1.566 - 1.651	30
7	Shortwave Infrared 2	2.08 - 2.35	30	Shortwave Infrared 2	2.107 - 2.294	30
10				Thermal Infrared	10.60 - 11.19	100

The watershed boundary data was derived from the USGS's National Hydrograph Dataset which has a 1:24000 scale. I extracted the study area watersheds utilizing ArcGIS 10.4. Using this geodatabase, I also extracted the streams of the study area.

The most recent National Land Cover Database (NLCD) dates to 2011. I downloaded NLCD2011 from TNRIS for entire Texas. The data is Landsat based and has a 30-meter pixel resolution. I also downloaded the Ecological Mapping Systems (EMS) of Texas data using an interactive app called Texas Ecosystem Analytical Mapper (TEAM). Because it offers more comprehensive information on different vegetation species of Texas, the data from the app was used to identify the land use and cover classes of the study area. TEAM is a Google Maps-based application and

developed by Texas Parks and Wildlife's (TPWD) Ecology program. The app allows users to view and download EMS data, Natural Resources and Conservation Services Soil Survey Geographic Data, National Hydrological Data, and TPWD's Land and Water Resources Conservation and Recreation Plan (LWRCRP) Properties data. The EMS data downloaded from the TEAM application is in the shape format having a very detailed attribute table describing each map units.

The Soil Survey Geographic Database (SSURGO) was used to obtain spatially distributed soil and geology data. The SSURGO data was downloaded from the Natural Resources Conservation Services (NRCS) website. The data was in the shape format and has a very detailed attribute table describing the characteristics of different soil types.

I downloaded daily, monthly and annual climate data of the stations within and adjacent to the study area from the National Oceanic and Atmospheric Center's (NOAA) online climate database for the 2008-2017 period. While deciding on the stations used in the analysis of the climate, I considered location, the period of record, and completeness of the precipitation measurements. All climate data was in the metric format.

Unfortunately, there wasn't a weather station having complete climate data within the study area. Hence, I used the climate data of the eight weather stations which are close to the study area. Table 2 indicates the weather stations which were used in this study. I also downloaded PRISM (Parameter-elevation Relationships on Independent Slopes Model) climate data because it considers many factors like elevation, coastal distance, topographic facet orientation and orographic efficiency of the landscape [54]. Prism precipitation data was in a 4-km grid format.

Table 2. Information about the weather stations.

Station Name	Lat.	Long.	Elevation	Precipitation Coverage for the Study Period (%)	Distance to the Study Area (km)
Camp Wood 5.02 SSE	29.60	-100.00	423.70	100.00	13.00
Hunt 10 W	30.06	-99.50	612.60	99.00	31.20
Prade Ranch	29.92	-99.79	625.40	99.50	5.67
Rocksprings 26 SSW	29.69	-100.42	525.80	100.00	35.00
Rocksprings 5.4 NW	30.07	-100.28	719.90	98.00	9.15
Rocksprings 8.5 WSW	29.97	-100.34	709.00	98.00	13.91
Vanderpool 10 N	29.85	-99.55	696.20	99.00	27.87
Vanderpool 4 N	29.81	-99.58	556.30	100.00	25.88

III.4 Analysis of the Climate and Hydrology of the Study Area

III.4.1 Rainfall and Runoff

Rainfall is a key characteristic of the climate in a region. While data from a rain gauge may be complete, it is not sufficient to represent the climatic characteristics of a region since the data can only offer point estimates. Thus, obtaining the estimates of precipitation partial distribution within a region from rain gauges is a significant concern of spatial interpolation [55]. Interpolation is a mathematical function which aims to produce estimated values for a location where measured data is absent by using the data from surrounding locations [56]. Spatial interpolation is helpful to obtain the estimates of precipitation for locations having varying distances to climate monitoring stations. Despite the availability of several interpolation methods, it is usually challenging to decide which one is the most suitable method to estimate rainfall as close as to actual conditions. Depending on the characteristics of datasets, interpolation methods can yield different results [57]. The inverse-distance weighting (IDW) method is widely used because of its easy computation and accessibility through many GIS packages. GIS users have the advantage of using the IDW as a default method to produce the attributes of unsampled locations using the values from sampled points in an area [58]. Many papers investigated the efficiency of different spatial interpolation methods to estimate areal rainfall and concluded that the IDW method can be used to present the distribution of precipitation when spatially dense gauges are found in the region.[59-61]. Furthermore, previous research indicated that the IDW method can also outperform other spatial

interpolation methods like ordinary kriging (OK) and spline even though the gauges are scarcely distributed throughout the region [57].

The IDW method estimates the values by calculating a weighted average of known points within a certain region. In calculating the weighted averages, close points (weather stations) carry higher weights than distant points. The method appoints values to unknown cells by utilizing the values of known cells. The values of unknown cells are the weighted sum of the values of N known data source [55]. Distance and power are two important parameters of the IDW method. An inverse relationship is established between known and unknown points in terms of the power of distance. The IDW formula for spatial interpolation of precipitation can be expressed as:

$$\hat{R}_P = \sum_{i=1}^N w_i R_i$$

$$w_i = \frac{d_i^{-a}}{\sum_{i=1}^N d_i^{-a}}$$

where \hat{R}_P refers to the unmeasured rainfall data(mm); R_i depicts the rainfall measured by gauge, N is the count of gauges, w_i is the weight for gauges, d_i demonstrates the distance from gauge i to unmeasured locations, a refers to the power.

I selected suitable rain gauges to evaluate their precipitation coverage for the period of the study. I calculated precipitation coverage of each station using the simple formula below;

$$PC = \frac{D}{365 \times CY} \times 100$$

where PC is the precipitation coverage of a station, D is the total number of days with precipitation records including records with zero precipitation, and CY is the count of years for the period of interest.

Because all climate stations selected are outside of the study area, I decided to interpolate annual average precipitation values using ArcGIS. Inverse Distance Weighting (IDW), Spline, Ordinary Kriging, Cokriging, and Thiessen Polygons are widely used methods for interpolation of the data from sparsely or densely distributed point sources. In this case, I preferred to use the IDW method due to its practicality, efficiency and relatively higher accuracy compared to other methods [62]. While performing this IDW interpolation analysis I determined grid size to be 4x4 km aiming to compare with the results from the PRISM climate data. I subsetted both IDW interpolation and PRISM data into study area extents. Thus, each 4 x 4 km pixel has a specific precipitation value for both sources data. I calculated spatial statistics of the two datasets to derive spatially distributed annual precipitation of the watersheds from 2008 to 2017. I entered the results into the JMP statistical software to compare both results derived from IDW and PRISM. I also calculated the simple average values of the climate data in daily, monthly and annual formats. Furthermore, I tested the influence of elevation on the distribution of rainfall for different stations.

Precipitation is the most significant element of a watershed which determines different patterns of the streamflow. The amount, duration and intensity of precipitation together with the season in which it occurs can bring about significantly different results. To explain the relationship between precipitation and streamflow I performed the one-way ANOVA test using the JMP. I calculated annual water yield using the following formula:

$$Q_A = \frac{Q*365*24*3600*0.0283168*1000}{A}$$

where Q_A indicates annual streamflow per unit area which is also called annual water yield (mm). Q is the annual average streamflow measured at the USGS gage (f^3/s). A indicates the area of the watershed (m^2).

I used the Web-based Hydrograph Analysis Tool (WHAT) to extract the baseflow fraction of the total flow, a key factor to characterize the hydrology of the watershed. WHAT is formerly used by Jain et al. (2005) and considered to be a suitable baseflow filtering program for karst watersheds.

III.4.2 *Delineation of the Drainage Area*

I needed exact borders of the drainage area to resize the remote sensing images. I used the 10-meter DEM to delineate the area drained by the USGS streamflow measuring gage near Barksdale. To perform this analysis, I used several tools within the Spatial Analyst toolbox and under the Hydrology folder of ArcGIS. The sequential order of this tools was:

- i. Using the fill tool to interpolate the elevations of no data pixels using information from the neighboring pixels;
- ii. Calculating flow direction by using filled DEM and generating a raster of flow direction from each cell to its steepest downslope neighbor;
- iii. Computing flow accumulation by using flow direction raster and creating a raster of accumulated flow into each cell;
- iv. Snapping pour point (USGS gage, Nueces River Nr Barksdale): snapping pour points to the cell of the highest flow accumulation within a specified distance; and
- v. Finally, using the watershed tool to calculate the contributing area above a defined point in flow accumulation raster.

The drainage area shapefile produced after these steps had an area which matched the USGS records (about 352 square miles). The shapefile was later used to clip all aerial and satellite images into the extents of the study area.

III.5 Remote Sensing Image Classifications

III.5.1 Preprocessing of the aerial images

For NAIP images, I first mosaicked all DOQQs using ArcGIS version 10.3.

However, I realized some gaps within the red, green and blue bands of the 2008 aerial image. To prevent these pixels from being unclassified during the classification processes I interpolated these areas using a formula in the raster calculator tool of ArcGIS. Figure 5 indicates the pixels with no value for band 3 (blue band). The code used to interpolate these pixels for the blue band was:

```
“Con (IsNull ("top2008_4bands_composite.tif - Band_3"), Focal Statistics  
("top2008_4bands_composite.tif - Band_3", NbrRectangle (5,5), "MEAN"),  
("top2008_4bands_composite.tif - Band_3"))”
```

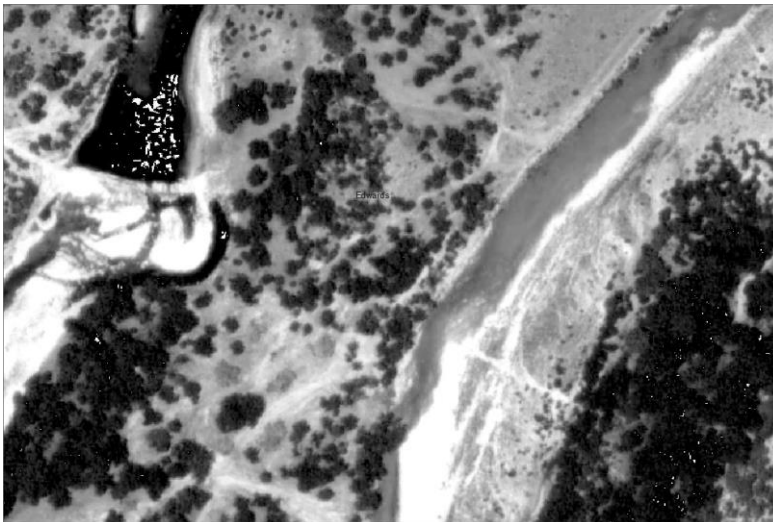


Figure 5. Areas with no data indicated by the small white scattered pixels on the water body (top left of the image) and within the woodland (bottom left).

The same steps were repeated for all bands to identify the pixels with no data. After filling the gaps for bands 1, 2 and 3 which are the red, green and blue bands respectively, I composited all the bands including near infrared to generate color-infrared images of the study area. Because the original 2008 aerial image had a 0.5-meter resolution, I resampled it to 1 meter to match the spatial resolution of other images. Following this initial processing I subsetting mosaicked aerial images to the extent of the study area using the drainage area shapefile.

To improve classification accuracy, ancillary data is oftentimes used to combine spectral characteristics of the scene with the information obtained from using several techniques. Texture and vegetation indices are mostly used methods. Thereby, I produced the texture band for all aerial images using the guidelines provided by the United States Forest Service for texture band generation of NAIP images. Neighborhood statistics under the Spatial Analyst tool of ArcGIS are used for several steps during the production of the texture band. Steps involved in deriving the image texture information are listed below:

- 1- Standard deviation is the primary statistic used for texture information. A window (rectangle) size of 7 was used to calculate standard deviations for the aerial images.
- 2- The resulting images were filtered using a 3x3 low pass filter to remove high values of texture.
- 3- Filtered texture images were smoothed using a focal mean function on the raster calculator. A 5 x 5 window is suggested by the United States Forest Service.

4- The copy raster tool was used to rescale created texture images. Data was converted to 8-bit signed integer.

Normalized vegetation index(NDVI) is one of the mostly used vegetation indices which quantifies the ratio of vegetation by calculating the difference in the reflectance from the near infrared and red bands. While green, healthy vegetation strongly absorbs red light, near-infrared portion of the electromagnetic spectrum is substantially reflected from the healthy vegetation. The value of the NDVI ranges from -1 to +1. However, there is no decisive boundary for distinct types of land cover. But in most cases, negative values indicate water while values close to +1 imply the presence of dense green leaves. Values close to 0 usually represent urban and built-up areas.

The formula of NDVI is:

$$NDVI = \frac{(NIR-RED)}{(NIR+RED)}$$

where NDVI is the Normalized Difference Vegetation Index, and NIR and RED are near infrared and red bands respectively.

After generation of the NDVI and texture bands for each aerial image, I subsetted them into the extents of the study area and stacked them with the spectral bands of aerial images. As a result, each aerial image had 6 bands in total. Because these aerial images were geometrically and radiometrically corrected before being available to public use, those newly created 6-band image data was ready for analysis. Figure 6 demonstrates the NDVI, texture, natural and false color images of a small portion of the study area in 2008.

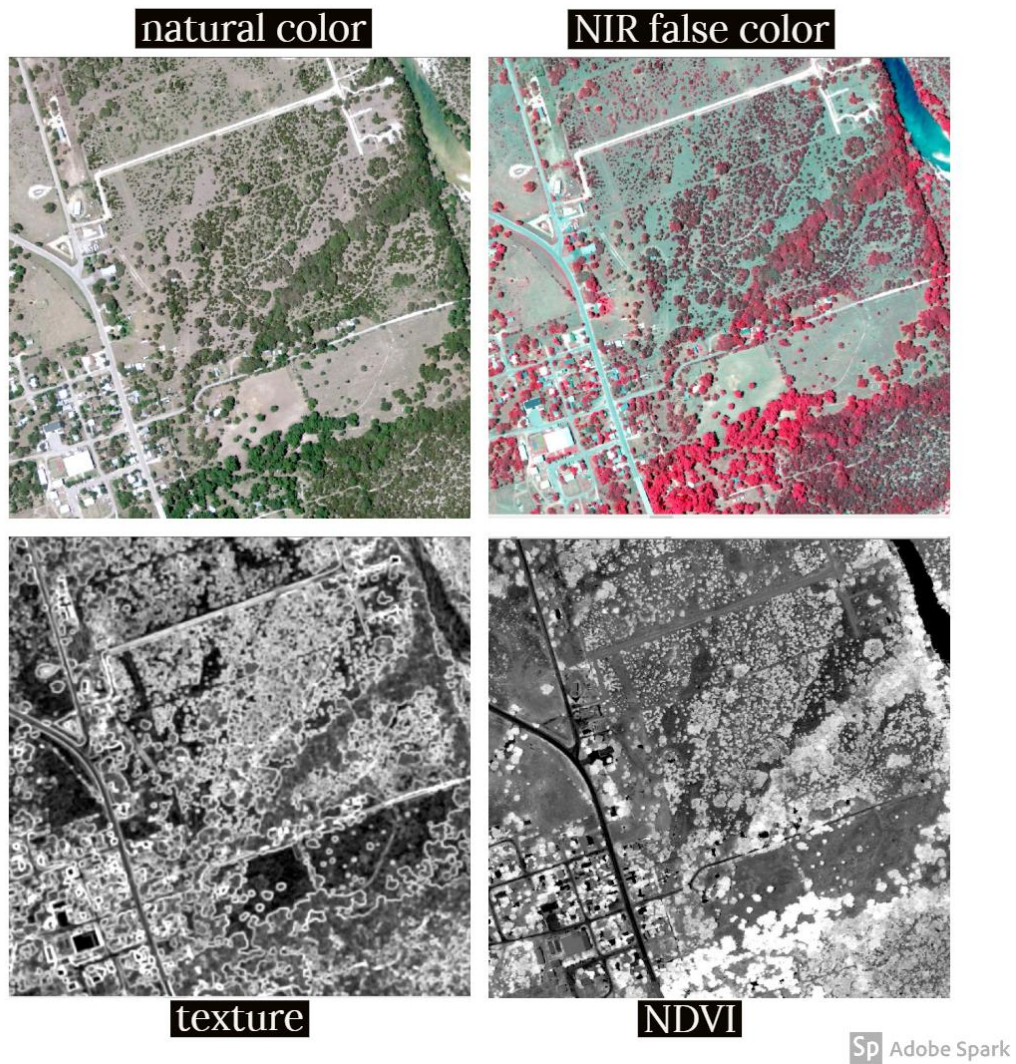


Figure 6. Natural color composite (top left), NIR false color composite (top right), texture band derived from the image (bottom left) and NDVI band (bottom right) of the 2008 aerial image. The area covered in the image is only 2.72 square kilometers and the scale is about 1/10000 (the study area is 907 square kilometers). The city seen in the images is Barksdale.

III.5.2 *Determining the Classification Scheme*

A classification scheme is a preliminary step for a supervised classification method. Anderson classification system is widely employed in the classification of Landsat images [63]. However, while it is suitable for coarse resolution (>30) image classifications, Anderson Classification approach is not appropriate when high-resolution aerial images are used for classification. Correctly identifying the major land use and cover types in the study area is critical. Field campaigns is not a cost-effective and practical alternative to analyze land use and cover in large and heterogenous watersheds. Besides, land use policy in the US makes this situation even more unfeasible because almost all the area is owned privately. Fortunately, there are a few alternatives to handle this problem. Prior studies can provide some knowledge about the land use and cover of the area. In addition to the information from the literature, the US-wide and Texas wide LULC datasets offer a decent opportunity to familiarize with the land use cover of the study area.

The NLCD, a US-wide land use and cover dataset, is a cooperative project conducted by the Multi-Resolution Land Characteristics (MRLC) Consortium. Landsat satellite images were used to produce NLCD datasets. The most recent NLCD dataset is NLCD2011. Table 3 indicates LULC types of the study area based on the NLCD 2011. The overall accuracies for the preceding NLCD datasets tested for level two classes were reported to be 79% and 78% for NLCD2001 and NLCD2006 respectively [64]. The definition of the classes shown in Table 4 reveals that there is more than one vegetation type within a land use category. While this can bring about a problem to identify

individual plant species, it is still helpful to target specific locations in the study area. Hence, I used the NLCD 2011 dataset to examine land use and cover of the study area. After sub-setting the NLCD 2011 data into the extent of the study area, I reclassified it to incorporate land cover classes with the codes shown in the first raster data. Since ArcGIS doesn't allow users to calculate statistics of a dataset with the floating-point data type, reclassification of the raw data enabled to create an attribute table by converting floating data type into integer data version. I calculated the percent cover of the classes represented in the drainage area by using the field calculator tool in the attribute table of the reclassified raster data.

Table 3. The LULC classes and their areas mapped and calculated by NLCD 2011 for the study area.

Class Code	NLCD2011 Dataset Classes	Area (km²)	Area (%)
52	shrub	544	60
42	evergreen forest	229	25
41	deciduous forest	99	11
71	grassland/herbaceous	26	3
21	developed, open space	7	1
11	open water	0	0
22	developed, low intensity	1	0
23	developed, medium intensity	0	0
24	developed, high intensity	0	0
31	barren land(rock/sand/clay)	1	0
43	mixed forest	0	0
82	cultivated crops	0	0
90	woody wetlands	1	0
Total Area		908	100

Table 4. Description of the NLCD land use cover classes within the study area

Class Code	Class Description
11	Open Water: Areas of open water, generally with less than 25% cover of vegetation or soil.
21	Developed, Open Space: Areas with a mixture of some constructed materials, but mostly vegetation in the form of lawn grasses. Impervious surfaces account for less than 20% of total cover. These areas most commonly include large-lot single-family housing units, parks, golf courses, and vegetation planted in developed settings for recreation, erosion control, or aesthetic purposes.
22	Developed, Low Intensity: Areas with a mixture of constructed materials and vegetation. Impervious surfaces account for 20% to 49% percent of total cover. These areas most commonly include single-family housing units.
23	Developed, Medium Intensity: Areas with a mixture of constructed materials and vegetation. Impervious surfaces account for 50% to 79% of the total cover. These areas most commonly include single-family housing units.
24	Developed High Intensity: Highly developed areas where people reside or work in high numbers. Examples include apartment complexes, row houses and commercial/industrial. Impervious surfaces account for 80% to 100% of the total cover.
31	Barren Land (Rock/Sand/Clay): Areas of bedrock, desert pavement, scarps, talus, slides, volcanic material, glacial debris, sand dunes, strip mines, gravel pits and other accumulations of earthen material. Generally, vegetation accounts for less than 15% of total cover.
41	Deciduous Forest: Areas dominated by trees generally greater than 5 meters tall, and greater than 20% of total vegetation cover. More than 75% of the tree species shed foliage simultaneously in response to seasonal change.
42	Evergreen Forest: Areas dominated by trees generally greater than 5 meters tall, and greater than 20% of total vegetation cover. More than 75% of the tree species maintain their leaves all year. Canopy is never without green foliage.

Table 4 continued

Class Code	Class Description
43	Mixed Forest: Areas dominated by trees generally greater than 5 meters tall, and greater than 20% of total vegetation cover. Neither deciduous nor evergreen species are greater than 75% of total tree cover.
52	Shrub/Scrub: Areas dominated by shrubs; less than 5 meters tall with shrub canopy typically greater than 20% of total vegetation. This class includes true shrubs, young trees in an early successional stage or trees stunted from environmental conditions.
71	Grassland/Herbaceous: Areas dominated by graminoid or herbaceous vegetation, generally greater than 80% of total vegetation. These areas are not subject to intensive management such as tilling but can be utilized for grazing.

Another land use land cover data source was the Texas Parks and Wildlife's (TPWD) Ecological Mapping Systems (EMS) dataset. This dataset is Texas-wide and much more detailed compared to the NLCD data. It has been produced by incorporation of Landsat satellite images and NAIP aerial images [65]. Both the NLCD and TEAM LULC datasets adopted a modified version of the Anderson Classification system. While the NLCD is in a 30-meter, TEAM data is originally created in a 10-meter spatial resolution. However, the LULC data I downloaded from TEAM interface was in the shape format. That's why I converted it into the raster format by specifying a raster resolution of 1 meter. Later, I repeated the same steps as in the NLCD and derived quantitative LULC information for the study area. Table 5 indicates the LULC classes of the study area based on the TEAM dataset.

Table 5. Land use cover for the study area derived from TEAM dataset

Class Code	Area (km²)	Area (%)	Land Use and Cover Class
10	321.57	35.45	Edwards Plateau: Ashe Juniper-Live Oak Shrubland
22	146.80	16.18	Edwards Plateau: Ashe Juniper Slope Forest
12	124.21	13.69	Edwards Plateau: Ashe Juniper-Live Oak Slope Shrubland
5	99.66	10.99	Edwards Plateau: Ashe Juniper Motte and Woodland
9	39.51	4.36	Edwards Plateau: Savanna Grassland
6	31.22	3.44	Edwards Plateau: Live Oak Motte and Woodland
24	20.07	2.21	Edwards Plateau: Oak - Ashe Juniper Slope Forest
17	20.05	2.21	Edwards Plateau: Riparian Ashe Juniper Shrubland
3	14.74	1.63	Edwards Plateau: Floodplain Ashe Juniper Shrubland
21	11.30	1.25	Barren
23	7.84	0.86	Edwards Plateau: Live Oak Slope Forest
30	7.49	0.83	Urban Low Intensity
27	7.18	0.79	Native Invasive: Mesquite Shrubland
14	7.13	0.79	Edwards Plateau: Riparian Ashe Juniper Forest
25	6.95	0.77	Edwards Plateau: Oak - Hardwood Slope Forest
11	6.19	0.68	Edwards Plateau: Shin Oak Shrubland
2	5.61	0.62	Edwards Plateau: Floodplain Live Oak Forest
33	5.10	0.56	Edwards Plateau: Floodplain Herbaceous Vegetation
7	4.14	0.46	Edwards Plateau: Deciduous Oak - Evergreen Motte and Woodland
4	3.64	0.40	Edwards Plateau: Floodplain Deciduous Shrubland
32	3.38	0.37	Edwards Plateau: Floodplain Hardwood Forest
8	2.88	0.32	Edwards Plateau: Oak - Hardwood Motte and Woodland

Table 5 continued

Class Code	Area(km²)	Area (%)	Land Use and Cover Class
1	2.54	0.28	Edwards Plateau: Floodplain Ashe Juniper Forest
15	2.24	0.25	Edwards Plateau: Riparian Live Oak Forest
13	1.30	0.14	Edwards Plateau: Shin Oak Slope Shrubland
19	0.87	0.10	Edwards Plateau: Riparian Herbaceous Vegetation
34	0.79	0.09	Edwards Plateau: Riparian Hardwood - Ashe Juniper Forest
31	0.74	0.08	Edwards Plateau: Floodplain Hardwood - Ashe Juniper Forest
29	0.61	0.07	Urban High Intensity
18	0.35	0.04	Edwards Plateau: Riparian Deciduous Shrubland
38	0.31	0.03	Edwards Plateau: Post Oak Motte and Woodland
16	0.29	0.03	Edwards Plateau: Riparian Hardwood Forest
37	0.20	0.02	Open Water
35	0.07	0.01	Edwards Plateau: Wooded Cliff/Bluff
36	0.06	0.01	Row Crops
20	0.05	0.01	Southwest: Tobosa Grassland
26	0.02	0.00	Native Invasive: Juniper Shrubland
40	0.01	0.00	Edwards Plateau: Barren or Grassy Cliff/Bluff
39	0.00	0.00	Marsh
28	0.00	0.00	Grass Farm
Total Area	907.12	100.00	

Examination of the land use and cover information obtained from these two datasets was quite helpful to understand vegetation types and intensity in the study area.

The NAIP images are projected in North American Datum 1983 (NAD83) Zone 14 North. So, I adjusted the projections of other spatial data to match the NAIP image

projection. I used ENVI version 5.4 to compare spatial data from various sources simultaneously. I viewed NLCD, TEAM and NAIP images in multiple windows after geometrically linking them in ENVI. Thus, I gained more confidence in the interpretation of individual objects. I also used Google Earth 3D-View to identify distinct types of woody vegetation. Ranch road 335 extends along the vertical axis of the study area and almost splits the study area into two similar halves. Also, a relatively short part of Highway Tx-55 passes through the western part of the study area. The street view provided by Google Earth 3D View is available along these two roads. This tool was an effective way to distinguish the species of woody plants. Oak and juniper spots marked along the ranch road 335 are shown in the Figure 7. Figure 8 demonstrates the use of Google Earth 3D View along with the aerial images and other available LULC datasets.

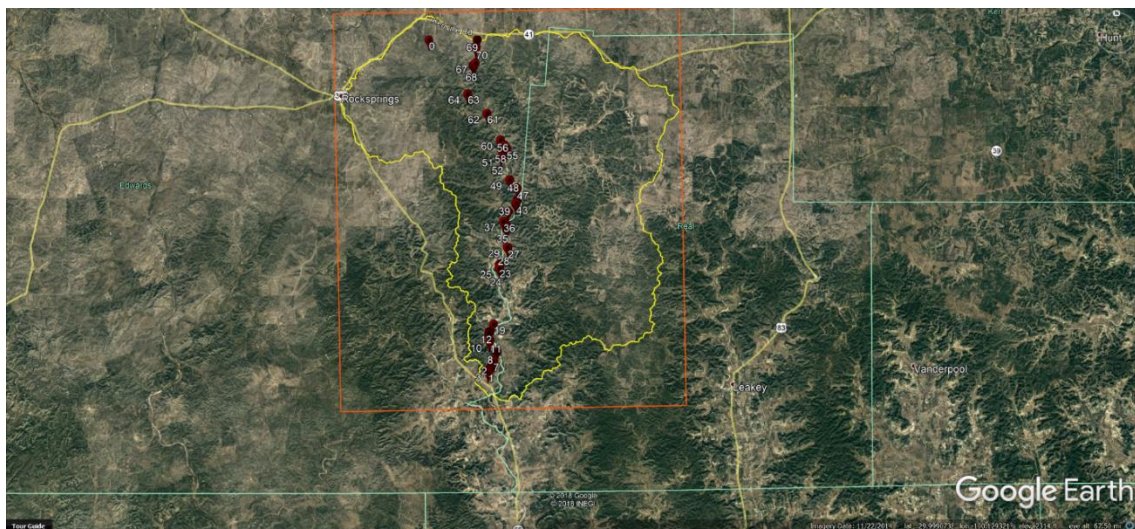


Figure 7. Locations of the 3D viewed junipers and oaks along Ranch Road 335. Yellow line indicates the boundaries of the study area.

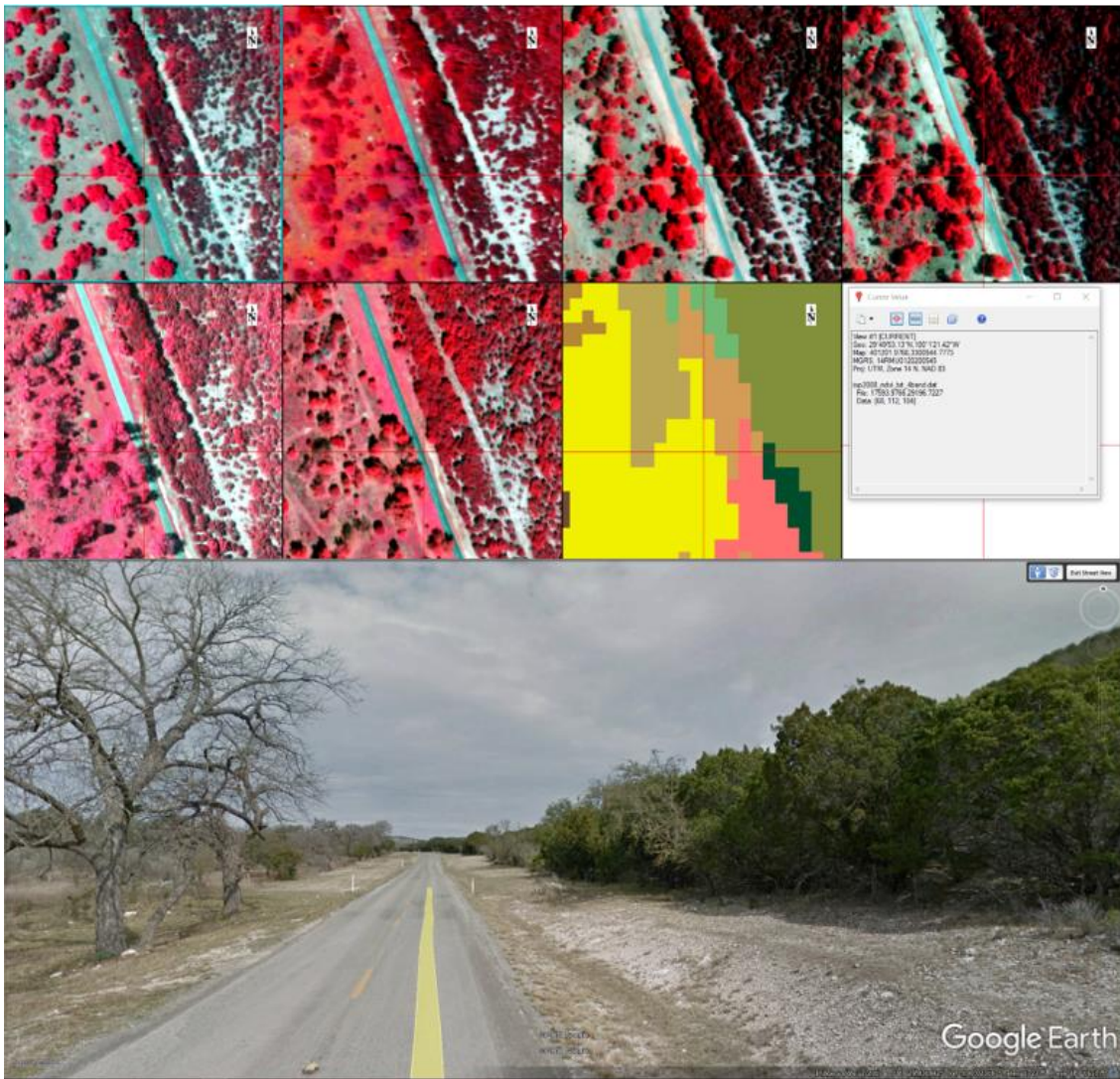


Figure 8. Distinguishing between junipers and oaks. All aerial images are displayed as near-infrared color composite (NIR-False color). The lower part is the exact cursor location displayed in Google Earth 3D View. While junipers have darker red color, oaks can be distinguished by bright red color. On the right-hand side of the road is mainly juniper while oaks are on the left.

I realized that there was a considerable amount of standing dead juniper trees in the study area. Because brush control is applied to junipers via mechanical and chemical treatments, a substantial number of standing dead junipers could be a sign of former chemical treatment or drought. A brush management site was shown in Figure 9. Figure 10 shows a small portion of the study area where dead junipers are seen. Additionally, image capturing dates vary considerably for the area. Although most of the images were taken in the agricultural growing periods, there were noticeable seasonal variation in the greenness of the herbaceous vegetation. Thus, I decided to have two separate herbaceous categories to preclude those cover types from producing noise during the classification.

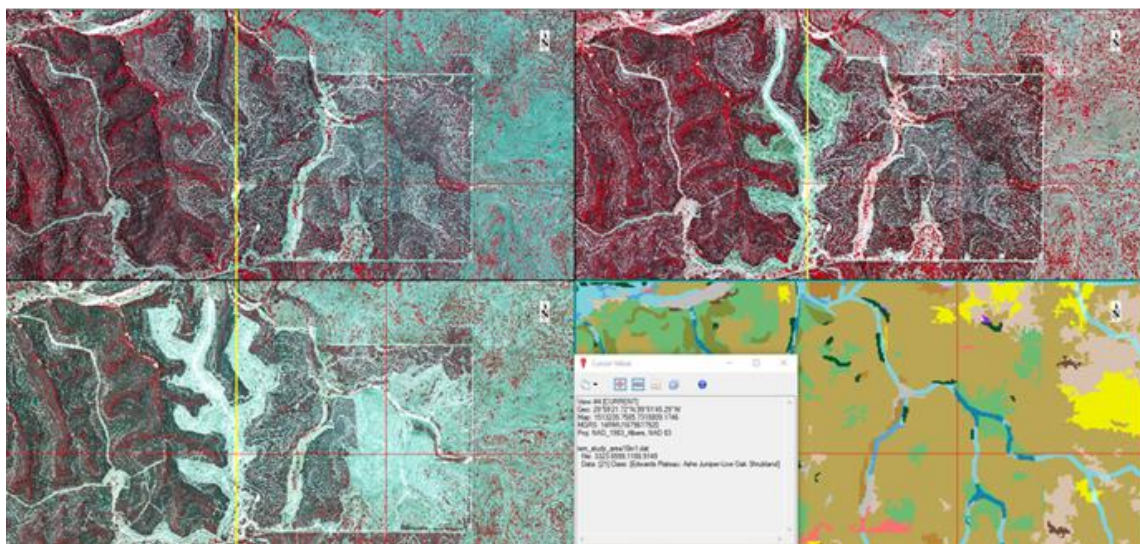


Figure 9. The progression of brush management from 2008 to 2012. Images displayed in smaller windows are TOP 2008 (top left), NAIP 2010 (top right), NAIP 2012 (bottom left) and TEAM land use land cover data.



Figure 10. Juniper mortality due to chemical treatment or drought.

Urban area cover was very low in the study area. There are only two small cities which fall into the boundaries of the study area, including a small proportion of the Rocksprings (Northwest) and Barksdale (South). Due to lower human population, there are very few cultivated lands in the study area. Most of the area is managed as

rangeland. Based on this observation, I included croplands within the herbaceous category.

Although the river channel is quite wide, water flows only in a narrow path from North to South. So, there are large unvegetated areas on the flanks of the riverbed. While flat areas usually covered by vegetation, barren areas can be easily observed on steeper slopes. Based on the TEAM, NLCD and Google Earth data, most of the woody vegetation cover is composed of *Juniperus ashei*, live oaks (*Quercus virginiana*) and some deciduous oaks.

Although high resolution aerial and spaceborne images enhance the analysis of remote sensing data, shadowed areas on these images bring about a significant problem. There was sizeable shadow cover in the NAIP and TOP aerial images. Hence, I decided to define a separate shadow category to quantify the shadow area in each image. Overall, I defined nine categories of land use and cover observed in the study area. Below is the list of these preliminary classes:

- 1) **Juniper:** All juniper species regardless of their height were included in this category.
- 2) **Oak:** Live oaks, deciduous oaks, and some broad-leaved trees were mapped in this category.
- 3) **Green Herbaceous Vegetation:** This class includes all types of non-woody vegetation having green leaves.
- 4) **Dry Herbaceous Vegetation:** Non-woody vegetation which doesn't have green foliage.

- 5) **Dead Juniper:** Any standing juniper trees and shrubs dried due to drought or herbicide treatment were placed into this category.
- 6) **Water:** Any type of open water areas like ponds, pools, and streams having visible water standing or flowing was included in this category. Ephemeral streams can be mapped as water if they have water flowing when the image was captured.
- 7) **Shadow:** Areas having little or no spectral response due to obstruction of incoming sun light were included under this category.
- 8) **Barren:** Areas with the open soil surface, rock outcrops, dry stream channels, roads, mining locations were placed in this category. These areas are completely exposed to direct or diffuse radiation since there is no vegetative cover.
- 9) **Urban:** Buildings of any size and type, and roads inside the city boundaries were included in this category.

III.5.3 *Training Data Collection and Analysis of Spectral Separability*

Training data or sampling data is essential for remote sensing image classification. While unsupervised image classifiers don't require sampling data, supervised classification algorithms use the statistical information derived from observed signals. Since every object on the earth has distinctive spectral characteristics (spectral signature), the quality and quantity of the training data are critical to the success of the classification. Sampling data is commonly obtained during field campaigns or collected on high resolution (<1 m) aerial photographs and satellite images [42].

Because the study area is extensively large and privately owned, a field survey was not a practical alternative. Hence, I collected training data with the aid of NLCD, TEAM, Google Earth 3D View and aerial images. I marked several locations along Ranch Road 355 on Google Earth and I created polygons of different land use and cover types after examining the vegetation and land use in 3D view. I exported this feature layer as a shape file and viewed it in the ENVI. Comparisons of different woody vegetation species within these polygons in the ENVI helped me gain confidence in the visual interpretation of these features. I realized that the color and texture differences between oak and juniper were more obvious in the 2008 image. The 2015 image was the only image captured during the leaf-off season. As a result, especially in the southern parts of the area, I noticed a considerable number of leafless trees on the image. However, this situation was helpful for differentiating between evergreen and deciduous woody plant species. The spatial pattern which was created by the configuration of dead

junipers in the study area shown in Figure 11 may imply the previous chemical treatments.

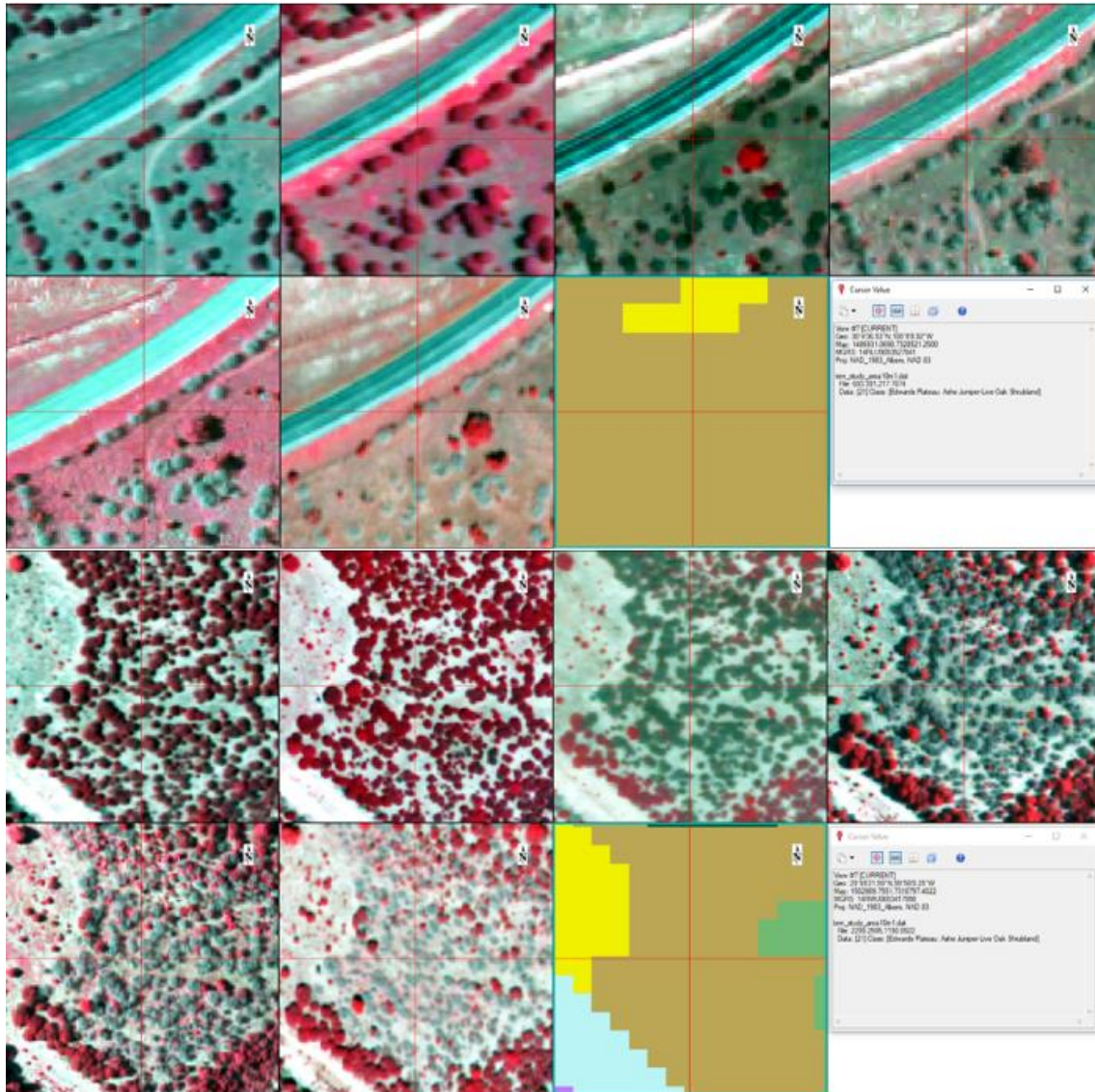


Figure 11. Two separate locations for 2008, 2010, 2012, 2014, 2015, and 2016 showing the juniper mortality. Juniper mortality occurred after 2010.

Training data can be collected using ROI (Region of Interest) tool in ENVI. This tool enables the collection of training data in several formats like a geometry (polygon, square, point etc.), pixels, and growing and threshold techniques. I used the default polygon technique to create ROIs for each class. The representability and number of ROIs can make a significant impact on the accuracy of the classification outputs. The rule of thumb for the number of ROIs is to produce at least ten times of the number of spectral bands for each land use and land cover class in the classification scheme. Because the images preprocessed had six bands, the minimum number of training data for each class should have been sixty. However, I collected thousands of training data because the study area is very large. Table 6 shows the number of training pixels collected for each class. To prevent the same locations are being sampled more than once, during the assessment of the accuracy, I divided the study area into multiple parcels. I selected four parcels to collect reference points to assess the accuracy of each classification. Total area spared for collecting reference points covered approximately 22% of the study area. Figure x shows the location of these parcels.

Table 6. Training data pixel counts for aerial image classification.

Number of Classes	Class Names	Count of Training Pixels for Aerial Images					
		2008	2010	2012	2014	2015	2016
1	Barren	23111	18028	15083	10674	8164	12348
2	Dead Juniper	1800	1227	1980	1421	1302	1345
3	Dry Herb	21351	3669	16709	17668	4204	9803
4	Green Grass	12371	40435	6858	5729	22267	15660
5	Juniper	19502	15025	14083	14024	16846	14978
6	Oak	48592	46723	45662	40929	52627	45403
7	Shadow	1592	2260	727	1176	1190	938
8	Urban	41225	42457	43860	35001	39352	39059
9	Water	74014	72048	51296	45739	56636	64475
Total Pixels		243558	241872	196258	172361	202588	204009

To test the separability of the classes of training data, the Jeffries-Matusita (JM) distance was used. Assuming the normal distribution of the spectral data obtained from ROIs, JM calculates the separability of the classes in a pairwise manner. The formula can be expressed as [66];

$$J_{ij} = \sqrt{2(1 - e^{-\alpha})}$$

where J_{ij} is the separability function for any two classes, α depicts the Bhattacharya distance. J_{ij} values range from 0 to 2. The values greater than 1.9 implies very good separability between classes. The 1.0 to 1.9 interval indicates moderate separability while the values lower than 1.0 mean poor separability of classes. So, any j_i value close to 1.9 and over 1.9 imply satisfactory separability between the classes. Jeffries-Matusita and Transformed Divergence separability analysis can be performed in ENVI.

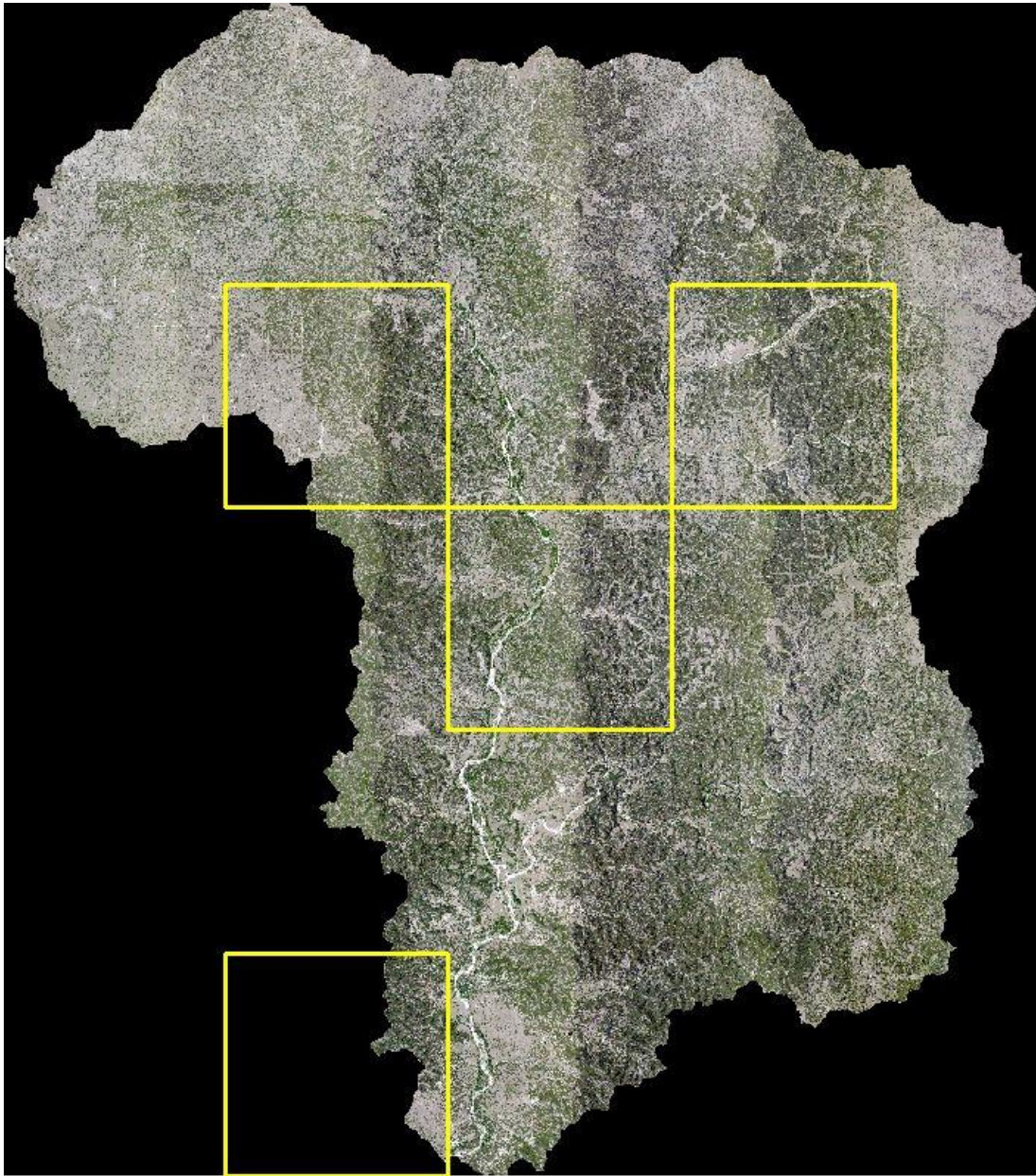


Figure 12. Parcels allocated to collect validation points (outlined with yellow color).

I conducted separability analysis for both original aerial images having optical (red, green, blue) and NIR band and NDVI and texture-stacked images using ENVI. Thus, I compared the effect of using texture and NDVI data on improving the separability of spectral signatures of varying land use and cover classes. Because the results of the spectral separability were important, before proceeding to the classification phase, I listed some of the separability results in this methodology section. I also reported the percent increase in the spectral separability resulted from the addition of the texture and NDVI bands. Table 7 shows the spectral separability of the NDVI and texture stacked aerial images and the percent increase in separability compared to the original 4-band imagery.

Based on the results of the separability analysis, I found that distinguishing between different objects can be improved by supplementing original images with the texture and NDVI data. Nevertheless, separability between oak and juniper remained below 1.9 for each training dataset. The 2008 training data had better juniper and oak separability than other years. Because only junipers were subjected to vegetation control in the study area and oak trees were selectively left during the brush treatment, I decided to map oak cover for only 2008 image. This approach was important in terms of reliable quantification of the oak area. So, I combined oak and juniper sampling data and created a “Tree” ROI for each year excluding 2008. As a result, the number of classes to be included in image classification became eight for these years.

Table 7. Improvement in spectral separability by addition of NDVI and Texture.

CLASS PAIRS		Original	Stack	Percent Increase
2008				
Juniper	Oaks	1.55	1.82	17.46
Greengrass	Oaks	1.65	1.85	12.09
Dryherbs	Deadjunipers	1.65	1.99	21.02
Shadow	Deadjunipers	1.66	1.98	19.06
Urban	Barren	1.73	1.93	11.47
Juniper	Shadow	1.73	1.88	8.57
Dryherbs	Urban	1.88	1.98	4.94
2010				
Juniper	Oaks	1.51	1.69	11.92
Greengrass	Oaks	1.23	1.59	30.02
Dryherbs	Deadjunipers	1.61	1.95	20.82
Shadow	Deadjunipers	1.9	1.98	4.69
Urban	Barren	1.7	1.89	11.16
Juniper	Shadow	1.82	1.88	3.3
Dryherbs	Urban	1.77	1.93	8.61
2012				
Juniper	Oaks	1.59	1.79	12.89
Greengrass	Oaks	1.74	1.85	6.19
Shadow	Deadjunipers	1.36	1.73	27.44
Juniper	Shadow	1.7	1.93	13.27
Dryherbs	Urban	1.54	1.91	24.11
Urban	Deadjunipers	1.89	1.95	3.48
Shadow	Water	1.87	1.99	6.36
2014				
Juniper	Oaks	1.05	1.48	41.23
Greengrass	Oaks	1.51	1.72	14.01
Dryherbs	Deadjunipers	1.61	1.97	22.5
Shadow	Deadjunipers	1.68	1.92	14
Urban	Barren	1.77	1.95	9.69
Juniper	Shadow	1.58	1.82	15.27
Dryherbs	Urban	1.62	1.92	18.17
Urban	Deadjunipers	1.59	1.8	13.28
Oaks	Shadow	1.89	1.98	4.75
Juniper	Greengrass	1.73	1.91	10.88
Urban	Water	1.87	1.92	2.64
Shadow	Water	1.72	1.95	13.23
Water	Deadjunipers	1.88	1.96	4.16

Table 7. continued

CLASS PAIRS		Original	Stack	Percent Increase
2015				
Juniper	Oaks	0.8038	1.0983	36.65
Greengrass	Oaks	1.1607	1.8054	55.55
Dryherbs	Deadjunipers	1.6003	1.9274	20.45
Urban	Barren	1.6462	1.8859	14.56
Dryherbs	Urban	1.5731	1.8215	15.79
Urban	Deadjunipers	1.6057	1.8024	12.25
Juniper	Greengrass	1.5683	1.933	23.25
Oaks	Deadjunipers	1.8377	1.9686	7.12
Dryherbs	Oaks	1.8297	1.9555	6.87
2016				
Juniper	Oaks	1.188	1.436	20.88
Greengrass	Oaks	1.7467	1.9227	10.07
Dryherbs	Deadjunipers	1.7024	1.9186	12.7
Urban	Barren	1.87	1.9693	5.31
Dryherbs	Urban	1.7209	1.9241	11.81
Greengrass	Dryherbs	1.8664	1.9508	4.52
Urban	Deadjunipers	1.738	1.9123	10.03
Juniper	Greengrass	1.6471	1.9358	17.53

III.5.4 Preprocessing of Landsat Satellite images

Before compositing each band of the Landsat images, I performed radiometric correction. I used the metadata file provided with the images to compute radiance, reflectance and at sensor-temperature. Landsat 8's OLI sensor has two more spectral bands than Landsat 5's TM sensor: a new coastal aerosol band (band1) and cirrus band (band9). Landsat 8's TIRS sensor has two thermal bands (band 10 and 11) while Landsat 5's TM sensor has one thermal infrared band (band 6). However, it is suggested to not use Landsat 8's thermal band 11 in scientific studies due to reported measurement errors [67]. So, I didn't include band 11 while compositing the Landsat 8 scenes. I used eight

Landsat 8 bands (bands 1 to 7 and 10) and seven Landsat 5 bands (all the bands) in the analysis of the land use and cover. Radiometric corrections were performed on the ArcGIS platform.

I derived NDVI and texture bands from Landsat images and stacked them with spectral bands and a thermal band of each scene. I generated the texture bands of Landsat images in ENVI using the variance of the spectral data. I applied a 3 x 3 kernel which was the minimum size for the calculation of variance.

III.5.5 Classification Scheme of Landsat Images

Images from Landsat satellite missions have a coarse-spatial resolution (30 meters). Thereby, resolving the objects having a size smaller than 30 meters in horizontal space is not feasible with these coarse resolution images. The guidelines defined by Anderson were quite helpful when classifying land use and cover from these images [63]. I determined the land use and cover classes to map using Landsat images based on the knowledge I obtained during the analysis of NLCD, TEAM LULC datasets, fine resolution aerial images and Google Earth 3D View. I adopted a modified Anderson Classification system for the classification scheme. I realized that the majority of live oaks in the study area were mapped under the shrub category of the NLCD dataset. Another point is that any area covered by sparsely distributed woody vegetation was mapped as shrubs in the NLCD dataset even though I observed that oak trees established a scattered canopy structure, particularly in range areas.

Both Landsat satellite images and NAIP aerial photographs don't provide any data on the heights of the objects. Light Detecting and Ranging (LIDAR) data is usually used to model canopy height. However, Lidar data is still very scarce. Because of these limitations, mapping shrub cover accurately is not a feasible way when multispectral remote sensing data is the only available source of data. So, I decided to map junipers regardless of their heights during Landsat image classifications. I defined two classes having oak cover: oak and oak savanna. I didn't include the urban area in the classification scheme of Landsat images because urban area accounted for less than 1% of the total land use and cover in the study area. Furthermore, there was high potential confusion between urban areas and barren areas due to the similar spectral response. The classes and their descriptions were listed below.

- 1) **Juniper:** Areas where *Juniperus ashei* covers more than 25% of the total vegetation area.
- 2) **Oak:** Areas dominated by live and deciduous oaks typically covering more than 50 % of the total vegetation area.
- 3) **Oak Savanna:** Usually used as range areas, where oak trees scatter around while herbaceous vegetation dominates the open spaces among trees. Oak cover ranges from 20% to 50% of total vegetation.
- 4) **Unvegetated:** Areas with less than 10% of total vegetation cover.
- 5) **Herbaceous:** Areas dominated by herbaceous vegetation (more than 80% of the total vegetation cover).
- 6) **Water:** Any area covered by open water.

III.5.6 Training Data for Landsat Images and Spectral Separability

I displayed corresponding Landsat scenes and aerial images in geometrically linked multiple windows in ENVI. I also compared locations on Landsat images to those in the NLCD and TEAM land use and cover datasets. The 2008 aerial image was employed to check for the oak-covered areas since I had sufficient confidence in identifying this land cover type only in 2008 data. Figure 13 demonstrates the identification of LULC on Landsat images during the training data collection. The number of training pixels collected for each class is shown in Table 8. I analyzed the spectral separability of Landsat training data using Jeffries-Matusita and Transformed Divergence techniques in ENVI. According to the results, most of the confusion occurred between herbaceous and oak savanna classes. There was also confusion to some extent between oak and juniper, oak and oak savanna, and oak savanna and juniper classes. Table 9 shows the results of separability analysis for each training dataset.

Table 8. The number of total pixels included in training data for each type of class by different years of Landsat 5 and Landsat 8 images.

Number of Classes	Class Name	Landsat Training Data Pixel Count					
		2008	2010	2013	2014	2015	2016
1	Herbaceous	2166	1920	1451	666	880	848
2	Juniper	6044	5797	6089	2427	2952	2743
3	Oak	1819	1431	1865	676	719	806
4	Oaksavanna	2050	2331	5381	1000	938	904
5	Unvegetated	724	569	628	473	263	192
6	Water	502	401	446	279	334	347
	Total	13305	12449	15860	5521	6086	5840

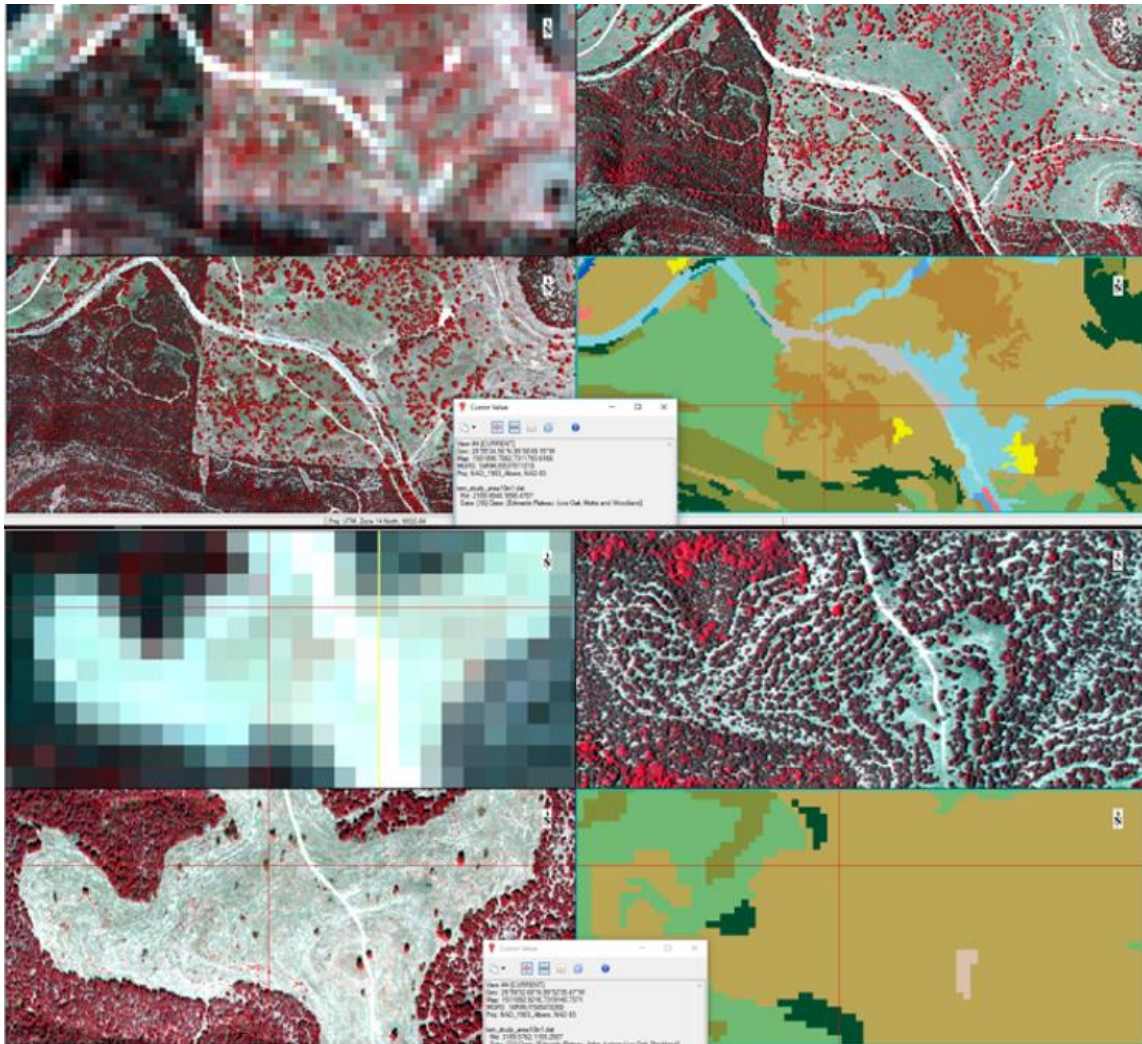


Figure 13. Training data collection processes for Landsat Images. The ENVI screen above indicates an area of oak savanna (to the right of the image) and juniper area (to the left of the image). The TEAM land use and cover dataset was displayed on the bottom left window. Images shown in the screen on top are Landsat8 2014, TOP 2008, NAIP 2014 and TEAM data from left to right, respectively. A brush management site is shown at the bottom of the ENVI split screen. The images displayed at the bottom screen are Landsat8 2015, TOP 2008, NAIP 2015 and TEAM dataset from left to right, respectively.

Table 9. Separability analysis of training data collected for Landsat image classifications.

Class Pairs	Roi Separability of Landsat Images					
	2008	2010	2013	2014	2015	2016
Herbaceous and Oaksavanna	1.67	1.58	1.49	1.68	1.42	1.58
Oak and Juniper	1.88	1.73	1.86	1.78	1.74	1.84
Oaksavanna And Juniper	1.89	1.74	1.78	1.94	1.96	1.98
Oak and Oaksavanna	1.93	1.80	1.94	1.89	1.87	1.94
Juniper and Water	1.95	1.94	1.99	1.96	1.97	1.97
Unvegetated And Water	1.97	1.98	1.97	2.00	2.00	2.00
Herbaceous and Juniper	1.98	1.88	1.88	1.97	1.97	1.95
Herbaceous and Unvegetated	1.98	1.98	1.96	1.99	1.99	2.00
Oak and Water	1.99	1.98	1.99	1.99	1.99	1.99
Oaksavanna And Water	2.00	2.00	2.00	2.00	2.00	2.00
Oaksavanna And Unvegetated	2.00	2.00	2.00	2.00	2.00	2.00
Herbaceous and Water	2.00	2.00	2.00	2.00	2.00	2.00
Unvegetated And Juniper	2.00	2.00	2.00	2.00	2.00	2.00
Oak and Herbaceous	2.00	2.00	1.91	2.00	1.97	1.99
Oak and Unvegetated	2.00	2.00	2.00	2.00	2.00	2.00

III.5.7 Classification of Aerial and Satellite Images

I used the supervised Maximum Likelihood method to perform the classification of each aerial image. For Landsat images, I used two classification techniques: Maximum Likelihood and Support Vector Machine(SVM). Maximum Likelihood Classifier uses the algorithm below to compute the probability that a pixel belongs to a specific class;

$$P(i|\omega) = \frac{P(i|\omega)P(i)}{P(\omega)}$$

where $P(i|\omega)$ depicts the likelihood function, $P(i)$ is the information from the training data which is the probability that class i exists in the area of interest and $P(\omega)$ is the probability that ω is observed(ω), and can be calculated by;

$$P(\omega) = \sum_{i=1}^M P(\omega|i)P(i)$$

where M indicates the number of classes. To make sure $\sum_{i=1}^M P(i|\omega)P(i)$ adds up to 1, $P(\omega)$ is generally treated as a normalization constant. Any pixel depicted by X is placed into a class (e.g., class j) by the formula;

$$x \in i \text{ if } P(i|\omega) > P(j|\omega) \text{ for all } j \neq i$$

According to these calculations, each pixel is placed into the class having the highest probability. Provided that the likelihood values are below a threshold defined by the user, those pixels are labelled as unclassified. In my case I didn't specify any threshold during the classification processes.

Support Vector Machines (SVM) is a nonparametric supervised classification method which has been tested in many studies investigating land use and cover change [68]. It doesn't require the assumption of the normal distribution of the spectral data. It has the capability of statistical learning. The necessary parameters to set up SVM are defined by users and every parameter has a distinctive effect on kernel type (polynomial, linear, radial basis function, sigmoid). As such, the classification accuracy of SVM models strongly relies on the selected parameters and kernel types. Ustuner et al. (2017) examined the impact of different parameter sets and kernel types on the accuracy of 63 different models in a study Turkey [68]. I adopted the best parameter set and kernel type

reported by Ustuner et al. So, I set up the SVM with kernel type and parameters indicated below:

- i. Kernel type: Polynomial
- ii. Gamma: 0.1 (default)
- iii. Polynomial Degree: 6
- iv. Bias: 5
- v. Error Penalty: 800

III.6 Intermediary Statistics and Classification Editing

III.6.1 Aerial Image Classifications and Initial Editing

After classifying aerial images using the Maximum Likelihood algorithm in ENVI, I combined green herbaceous and dry herbaceous classes to create a “herbaceous” category. While visually interpreting the classification outputs I realized that a great deal of pixels having no vegetative cover were mapped as urban. This was expected due to a similar spectral response from uncovered and urban areas. Since the total area of human-built structures accounts for less than 1% of the study area as documented in the NLCD and TEAM datasets, I decided to combine urban and barren areas into an unvegetated category. Figure 14 shows classification result of before and after class combinations applied. Later, I used the shape files created to delineate the urban area in the study area to edit the unvegetated class and extract urban/built-up areas.

Mapping dead junipers wasn’t easy or even possible with coarse-resolution satellite images. However, modeling dead junipers is not a practical way in terms of

hydrological modeling. In other words, including dead juniper within the juniper category increases the bias when estimating the hydrological response of watersheds. Every object within the watershed can have an influence on the hydrological cycle. But this impact can be so negligible or significant depending on the combination of many factors like biophysical characteristics and spatial distribution and coverage. Table 10 indicates the initial classification results. The results implied that more than 5% of the study area was covered by dead Junipers. This result can be significant to account for the impact of dead junipers in hydrological modeling studies investigating the impact of brush encroachment on water yield. Figure 15 shows an area covered by dead juniper and its classification result.

Table 10. Area of each land use and cover class in different years computed by using the initial classifications.

Class Name	Initial Classification Statistics					
	Area of The Classes (Percent)					
	2008	2010	2012	2014	2015	2016
Dead junipers	10.27	8.45	5.55	12.07	8.58	12.33
Herbaceous	17.84	22.96	19.22	17.19	14.77	11.33
Juniper	36.66					
Oaks	13.61					
Shadow	5.55	4.69	4.83	10.00	9.44	6.61
Trees		52.30	44.63	40.66	53.16	48.61
Unvegetated	15.89	11.43	25.65	19.85	13.89	20.92
Water	0.18	0.15	0.11	0.23	0.16	0.20
Total	100.00	100.00	100.00	100.00	100.00	100.00

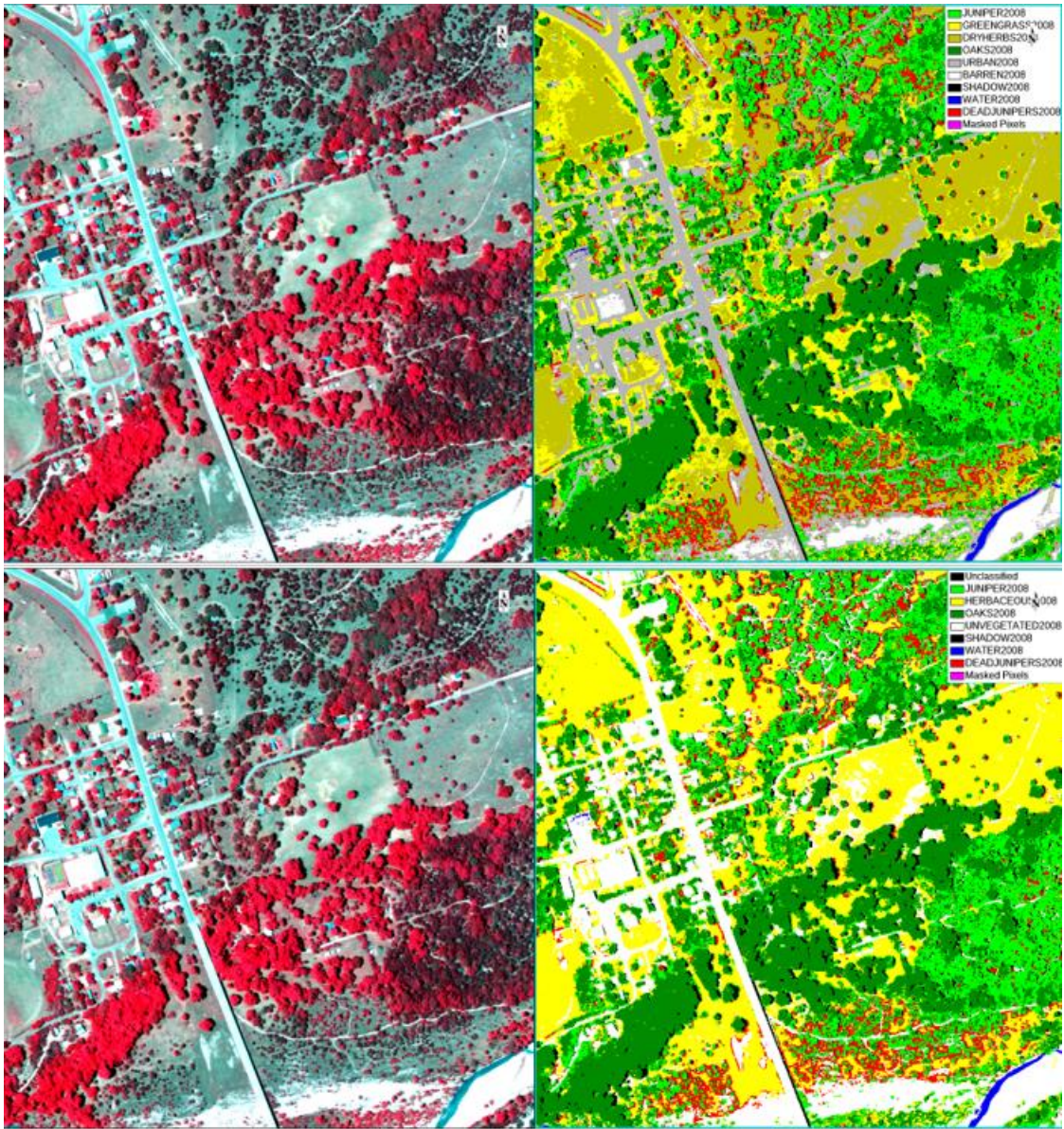


Figure 14. Classification of the 2008 image before combining urban with barren and dry herbaceous with green grass (above) and after applying combinations (below).

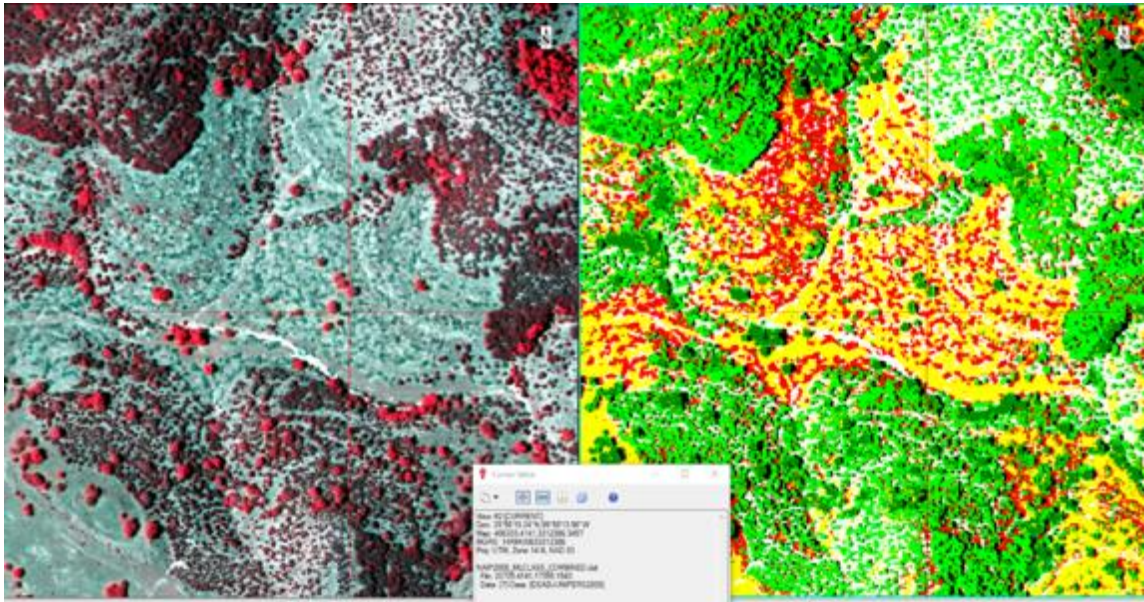


Figure 15. A juniper treatment site in 2008 aerial image (left) and the Maximum Likelihood classification result for the same location (right). Oaks, junipers, herbaceous, barren areas, and dead junipers were indicated by darker green, light green, yellow, white, and red color, respectively.

Although class statistics hinted that the dead juniper cover was significant, I realized some noise in the classification of dead junipers, especially in 2008 and 2012 images. Brush management activities in the study area were intensified after 2010. I observed by visual interpretation of the classification images and aerial images that the mechanical treatment areas expanded substantially after 2010. I found that dead juniper area was significantly overestimated in 2008 image classification. In contrast, the dead juniper area was underestimated in the 2012 classification. The overestimation problem in 2008 classification primarily resulted from the misclassification of areas where a transition from shadow to herbaceous occurs. These misclassified dead juniper pixels mostly concentrated around the sparsely distributed woody vegetation (mostly live

oaks). Figure 16 indicates misclassified dead juniper area in the 2008 aerial image. I resolved this issue by converting dead juniper pixels into the herbaceous category. I relied on several assumptions when applying this solution:

- i. Brush management was performed by mechanical or chemical treatments in the study area. The goal of brush control is to convert invasive shrub species like junipers into native herbaceous vegetation. Hence, I assumed that the final land use and cover state of the areas where brush control was implemented was herbaceous.
- ii. Empirical data is needed to quantify rainfall interception from this standing dead juniper mass to model their hydrological influence accurately. Plus, there is currently no matching database in the SWAT's land use cover and plant database associated with the dead juniper category. Because dead junipers aren't biologically active, the ET from those areas cannot match the ET from the areas covered by healthy junipers. I assumed that the ET from dead juniper areas is more comparable to ET from herbaceous cover.
- iii. I assumed that the issue of overestimated dead juniper pixels in 2008 image due to the confusion of dead juniper spectral response with shadow is substantially compensated when herbaceous and dead juniper classes are combined. This adjustment is also applicable to other years.

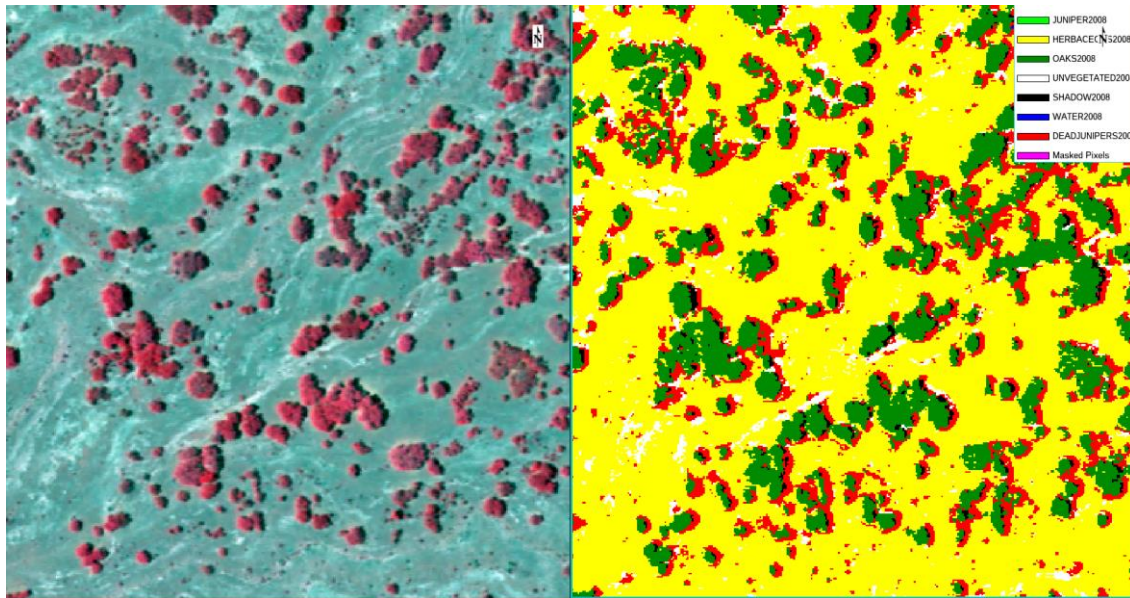


Figure 16. Misclassified dead juniper pixels. On the left is the NIR false-color composite of TOP 2008 aerial image, and on the right is the ML classification of 2008 image.

Classified shadow area for each aerial image ranged from 4.49 % to 10% of the total area. Especially, as shown in Figure 17, 2014 and 2015 image classifications indicated that there was very high shadow cover during the image capturing. Overall, because the shadow cover accounted for a very significant number of pixels in each classification, it is important to identify land use and cover within the shaded locations. Because the temporal resolution of NAIP images causes a significant limitation to reveal what type of land use and cover resides under the shadow, I developed a strategy to handle this challenge. I decided to compensate the limitation resulted from the temporal resolution of aerial imagery with the information provided from satellite image classifications. I'll describe the methodology for identifying LULC of shadow pixels after the satellite image classification section.

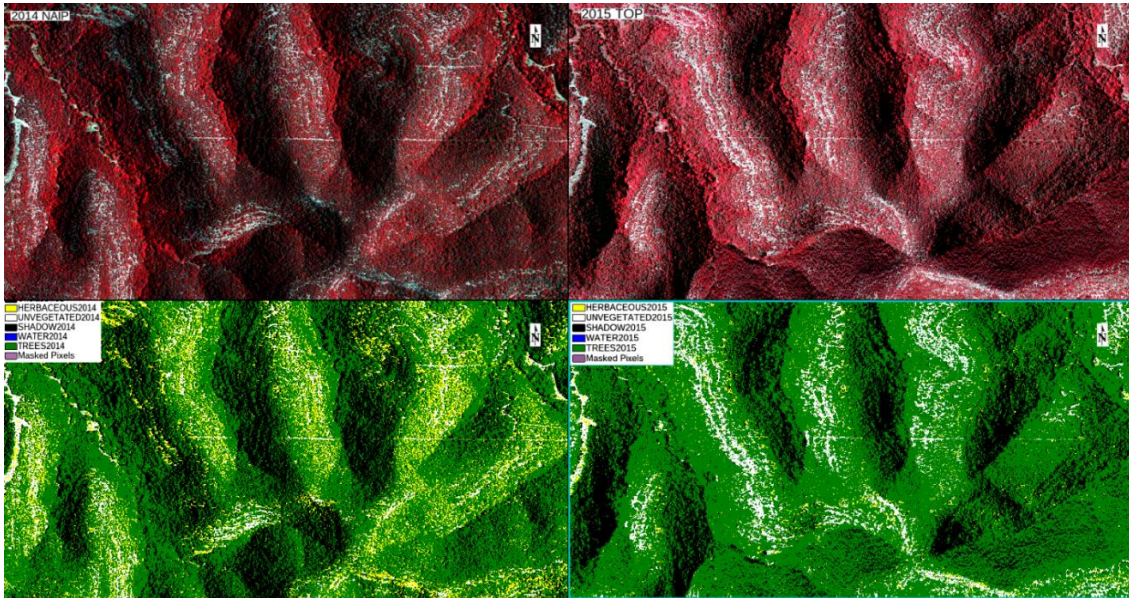


Figure 17. Intensive shadow cover of 2014 and 2015 aerial images. The images below from left to right are 2014 and 2015 ML classifications, respectively.

III.6.2 *Satellite Image Classifications and Post Classification Editing*

I classified six Landsat images using Maximum Likelihood (ML) and SVM methods. The same ROI data was used to train both classification algorithms. For 2014 Landsat image, I re-collected training data using the pixel method with varying brush sizes (mostly greater than 2) instead of using geometric features like polygons. Thus, I aimed to investigate the impact of different ROI collection methods on the response of the same classification algorithm. I found out that the selection of ROI collection method had an important impact. The area of each land use cover was different in two Landsat 2014 ML classifications. Table 11 indicates the area of each class for 2014 Landsat image based on the two-training data collection method. Oak savanna area was estimated substantially higher in the classification which used pixel method. I noticed that this

higher estimate of oak savanna resulted from the classification of herbaceous cover as oak savanna with this approach.

Table 11. Area of classes for two 2014 ML classifications performed using differently collected ROIs.

Classes	2014 Landsat MI Class Statistics(Percent) With Different Roi Methods	
	Polygon Method	Pixel Method
Herbaceous	11.28	5.76
Juniper	57.37	48.63
Oak	12.51	7.17
Oaksavanna	14.35	30.01
Unvegetated	2.43	4.49
Water	2.06	3.94

Table 12 shows the results of the ML and SVM classifications for Landsat images. The results indicated that there was a considerable difference in terms of the area of each class. I realized that while juniper cover was overestimated in SVM classifications, water area was overestimated in ML classifications. Because my major focus was on identifying shadow pixels in aerial image classifications, I decided to utilize ML classification results.

Table 12. Initial statistics of Landsat ML and SVM classifications.

Classes	Maximum Likelihood (ML) and Support Vector Machine (SVM) Landsat Classification LULC Statistics (Percent)					
	2008 ML	2008 SVM	2010 ML	2010 SVM	2013 ML	2013 SVM
Herbaceous	14.11	12.66	17.83	12.65	8.47	4.73
Juniper	54.07	62.80	49.93	61.13	54.10	61.26
Oak	8.61	7.25	7.65	4.76	8.22	7.37
Oaksavanna	19.22	15.04	19.34	18.47	23.95	23.79
Unvegetated	2.26	1.95	3.39	2.44	4.09	2.26
Water	1.74	0.28	1.87	0.55	1.17	0.59
Total	100	100	100	100	100	100

Classes	Maximum Likelihood (ML) and Support Vector Machine (SVM) Landsat Classification LULC Statistics (Percent)					
	2014 ML	2014 SVM	2015 ML	2015 SVM	2016 ML	2016 SVM
Herbaceous	5.76	6.55	10.37	6.38	12.81	6.56
Juniper	48.63	69.92	60.91	66.70	55.60	63.40
Oak	7.17	8.75	7.68	7.05	11.23	11.11
Oaksavanna	30.01	12.52	16.94	17.65	15.38	16.55
Unvegetated	4.49	1.95	2.48	1.73	3.15	1.98
Water	3.94	0.31	1.63	0.48	1.82	0.40
Total	100	100	100	100	100	100

I edited the pixels classified as water in ML classifications using the information extracted from SVM classifications. Figure 18 demonstrates the adjustment of water pixels in Landsat ML classification with the use of information derived from Landsat SVM classifications. I first applied a majority filter with a window size of 3 to both ML and SVM classifications to remove isolated pixels. Thus, some misclassified individual water pixels were removed in SVM classifications. I found out that some electromagnetic radiation from urban area led SVM to classify some urban area as water. In ArcGIS, I created a polygon shapefile and digitized urban areas using high-resolution aerial images. I converted this urban shapefile into an ENVI ROI file and converted water pixels into unvegetated on SVM products using the ENVI post classification editing tool. Later, I used the “convert classification to vector” tool in ENVI and created vector files for each category classified by the SVM. Having these vector files converted to ROI files, I edited the water pixels of ML products. After these steps, I performed accuracy assessment for Landsat ML image classifications and converted ML products into the vector files for use in editing shadow pixels in ML classifications of NAIP images. Final area statistics for Landsat ML classifications are shown in Table 13.

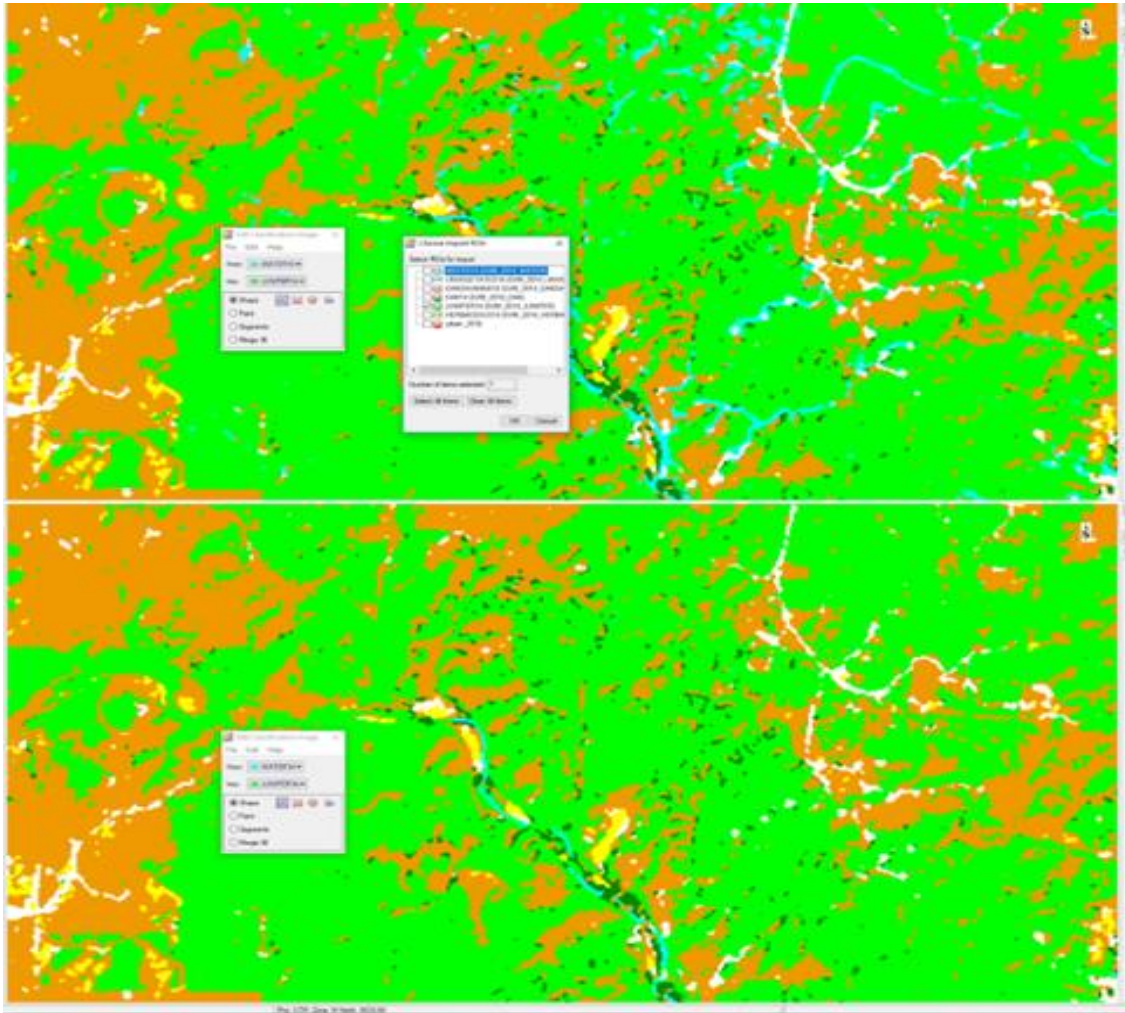


Figure 18. Correcting for water pixels in Landsat 2013 ML classification image using the information from the same image's SVM classification. While water pixels scatter around in the 2013 ML product (top), they were substituted with the juniper pixels imported from the SVM (bottom).

Table 13. Area of each class for every Landsat image ML classification after water pixels are edited.

Classes	Finalized Landsat Images ML Classification LULC Statistics (Percent)					
	2008 ML Final	2010 ML Final	2013 ML Final	2014 ML Final	2015 ML Final	2016 ML Final
Herbaceous	13.19	17.23	6.86	5.00	9.05	11.72
Juniper	58.85	54.85	58.27	54.03	65.59	60.25
Oak	6.67	5.63	6.25	5.54	5.39	9.09
Oaksavanna	18.93	18.85	24.21	31.10	17.26	15.51
Unvegetated	2.08	3.14	3.81	4.05	2.25	3.02
Water	0.20	0.25	0.54	0.23	0.40	0.36

III.7 Accuracy Assessment of the Classified Images

As a measure of reliability and utility of a product of remote sensing image classification, thematic map accuracy quantifies the level of agreement between the attributes of a thematic map and reference points [69]. The primary step for analyzing the accuracy of a map is the identification of the target population which indicates the locations depicted by the LULC map [70]. Ground truth data (reference points) can be provided for each class by interpreting high-resolution aerial photography and satellite images, videography, field surveys, or with the incorporation of all these techniques [70].

The accuracy assessment of the classifications can be conducted by generating an error matrix (confusion matrix), which compares the agreement between ground truth data (field surveys, high resolution aerial and satellite imagery) and the resulting thematic map on a class-by-class basis [71]. Table 14 indicates a sample confusion matrix.

Table 14. Sample confusion matrix for the accuracy assessment of a classification.

Map Categories		Ground Truth Pixels				Total
		1	2	3	k	
Classified Pixels	1	$X_{1,1}$	$X_{1,2}$	$X_{1,3}$	$X_{1,k}$	Total _{R1}
	2	$X_{2,1}$	$X_{2,2}$	$X_{2,3}$	$X_{2,k}$	Total _{R2}
	3	$X_{3,1}$	$X_{3,2}$	$X_{3,3}$	$X_{3,k}$	Total _{R3}
	k	$X_{k,1}$	$X_{k,2}$	$X_{k,3}$	$X_{k,k}$	Total _{R4}
Total		Total _{C1}	Total _{C2}	Total _{C3}	Total _{C4}	Total Obs.

The diagonal values in the confusion matrix demonstrate the full agreement between the ground truth pixels and the classified pixels. The ratio of the sum of all correctly classified pixels to a total number of ground truth pixels gives the overall accuracy of the classification. It is shown as a percentage. The overall accuracy can be formulated as;

$$OA = \frac{\sum_{a=1}^U X_{kk}}{Q} \times 100$$

where OA is the overall accuracy of the classification, Q depicts the total number of pixels and U shows the total number of classes. According to Scepan. (1999) an acceptable overall accuracy should be equal to or greater than 85% [72]. Producer's and user's accuracies are two other important accuracy measurements for the classification.

Producer's accuracy is measured by the ratio of the number of correctly classified ground truth pixels to the sum of ground truth pixels for each class. The

resulting value indicates how well the ground truth pixels are correctly classified for each type of class. The diversion from the complete accuracy in the producer's accuracy gives the omission errors. The formula for the producer's accuracy can be written as:

$$PA = \frac{X_{kk}}{X_{Ck}} \times 100$$

where PA is the producers' accuracy, X_{kk} is the value at the k^{th} row and k^{th} column, X_{Ck} is the column total for any class. Story and Congalton (1986) stated that minimum acceptable producer's accuracy for a class should be 90% [73].

User's accuracy quantifies how successfully the classification is done. The resulting statistic shows the percentage of the probability that a pixel on the classified data truly represents that class on the ground [73]. It is calculated by the ratio of the total number of correctly classified pixels for each class to the row sums for each class. The deviation from the complete accuracy gives the commission error. The formula for calculating the user's accuracy can be written as:

$$UA = \frac{X_{kk}}{X_{Rk}} \times 100$$

where UA is the User's Accuracy, X_{kk} is the total number of correctly classified pixels for each class, and X_{Rk} is the row sum for each class. Another quantification method for classification accuracy is the Kappa coefficient which integrates the off-diagonal values along with the diagonal ones so that it can generate a more reliable assessment of the accuracy compared to overall accuracy[38].The formula of the Kappa coefficient can be written as [74]:

$$K = \frac{N(\sum_{i=1}^k X_{ii}) - \sum_{i=1}^k (X_{i+} \times X_{+i})}{N^2 - \sum_{i=1}^k (X_{i+} \times X_{+i})}$$

where K is the Kappa coefficient, N is the total number of sample pixels, $\sum_{i=1}^k X_{ii}$ is the sum of major diagonal, and $\sum_{i=1}^k (X_{i+} \times X_{+i})$ is the sum of products of the class row total and the class column total for all rows and columns.

III.7.1 *Collection of Validation Samples*

There are several types of sampling strategies for obtaining reference data including random, stratified random, systematic, and cluster sampling. Determining sampling size is another challenging task. However, the rule of thumb for the size of reference points is to collect at least 50 samples for each LULC class. For classifications having more than 12 classes, collecting at least 75 to 100 samples is recommended.

Reference points were collected with the interpretation of high-resolution aerial images, Google Earth 3D view and TEAM LULC map. Figure 19 demonstrates the collection of reference points for 2015 Landsat Image. I adopted the random sampling approach while collecting the points. More points were collected for juniper and oak classes. I collected validation points within the parcels spared for the accuracy assessment of the classifications. The number of reference pixels collected for each LULC class to test the accuracy of Landsat ML classifications is shown in Table 15. Table 16 shows the number of preliminary reference pixels collected for the initial accuracy assessment of aerial image classifications.

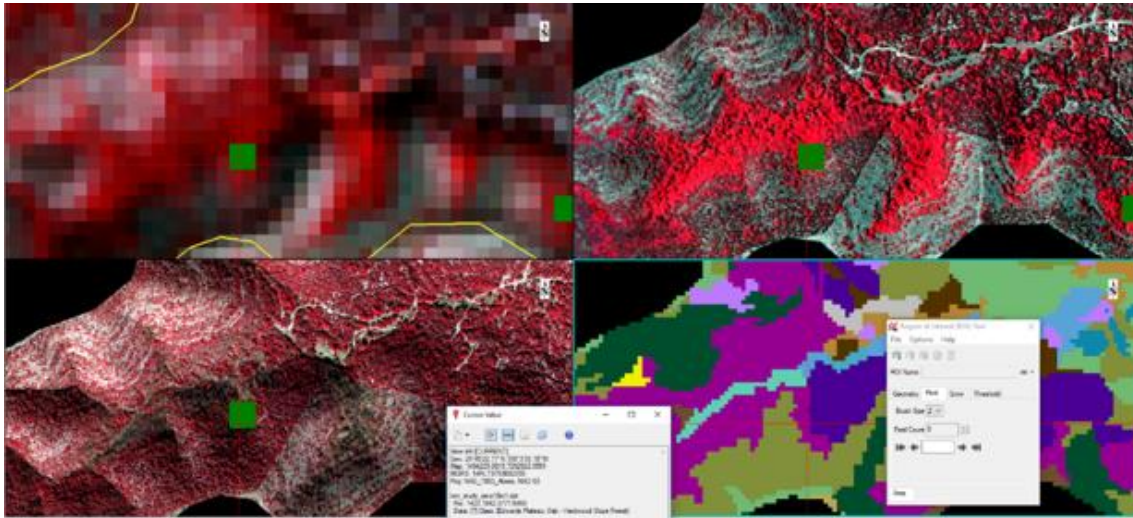


Figure 19. Collecting validation samples for 2015 Landsat 8 image using both aerial photographs and TEAM dataset. Images seen on the split screen are 2015 Landsat image (top left), 2008 TOP aerial image (top right), 2015 NAIP image (bottom left) and TEAM LULC dataset (bottom right).

Table 15. Number of validation pixels collected for the accuracy assessment of Landsat image classifications

Class Name	Reference Data Pixel Count for Landsat Image Classification Accuracy Assessment					
	2008	2010	2013	2014	2015	2016
Herbaceous	100	100	100	100	100	100
Juniper	250	250	250	250	250	250
Oak	200	150	200	200	200	200
Oak Savanna	150	100	100	100	150	99
Unvegetated	90	70	70	100	100	70
Water	60	70	70	70	100	75
Total	850	740	790	820	900	794

Table 16. Preliminary validation pixels collected before editing shadows in the aerial image classifications

Class Name	Reference Data Pixel Count					
	2008	2010	2012	2014	2015	2016
Dead juniper	70	70	70	70	70	70
Herbaceous	100	100	100	100	100	100
Shadow	70	70	70	70	70	70
Tree		300	300	300	300	300
Unvegetated	70	70	70	70	70	70
Water	70	70	70	70	70	70
Juniper	200					
Oak	100					
Total	680	680	680	680	680	680

III.7.2 Accuracy of the Initial Aerial Image Classifications and Final Satellite Thematic

Maps

I reported four types of accuracy metrics for initial NAIP and final Landsat classifications: overall accuracy, Kappa coefficient, producer’s and user’s accuracy. Because I used the information derived from the Landsat classifications to identify the shadow area in the aerial images, I reported the final accuracy results of Landsat classifications in the methodology chapter. The final accuracy statistics for Landsat ML image classifications are shown in Table 17. Table 18 shows the results of the accuracy assessment of the preliminary ML aerial image classifications.

Table 17. Final accuracy assessment results of the Landsat image classifications.

Landsat ML user accuracy (percent)						
class name	2008	2010	2013	2014	2015	2016
herbaceous	91.67	84.68	70.51	88.14	82.73	94.06
juniper	90.74	95.20	87.36	90.48	87.28	93.80
oak	99.44	96.21	93.81	96.55	95.93	94.30
oaksavanna	94.19	76.72	78.64	63.01	92.31	89.22
unvegetated	97.73	100.00	90.79	96.08	94.95	100.00
water	100.00	100.00	100.00	100.00	100.00	100.00
Landsat ML producer accuracy (percent)						
class name	2008	2010	2013	2014	2015	2016
herbaceous	99.00	94.00	55.00	52.00	91.00	95.00
juniper	98.00	95.20	94.00	98.80	98.80	96.80
oak	89.50	84.67	91.00	84.00	82.50	91.00
oaksavanna	97.33	89.00	81.00	92.00	88.00	91.92
unvegetated	95.56	92.86	98.57	98.00	94.00	95.71
water	81.67	94.29	100	94.29	93.00	97.33
overall and kappa						
	2008	2010	2013	2014	2015	2016
kappa coefficient	0.93	0.90	0.84	0.85	0.89	0.93
overall accuracy (%)	94.59	91.76	87.59	88.17	91.33	94.46

Table 18. Initial accuracy assessment results of aerial image classifications.

Class	Initial User Accuracy (Percent)					
	2008	2010	2012	2014	2015	2016
dead junipers	93.33	93.94	87.32	98.48	97.10	98.53
herbaceous	94.74	71.22	87.62	79.28	85.19	98.99
shadow	100.00	97.18	90.41	81.40	90.67	95.65
trees	99.66	99.62	99.66	97.88	98.61	99.67
unvegetated	73.40	78.82	77.22	83.95	79.76	83.33
water	98.11	100.00	100.00	100.00	96.49	98.33
juniper	98.02					
oak	100.00					

class	initial producer accuracy (percent)					
	2008	2010	2012	2014	2015	2016
dead junipers	100.00	88.57	88.57	92.86	95.71	95.71
herbaceous	90.00	99.00	92.00	88.00	92.00	98.00
shadow	98.57	98.57	94.29	100.00	97.14	94.29
trees	97.67	87.00	97.33	92.33	94.33	99.67
unvegetated	98.57	95.71	87.14	97.14	95.71	100.00
water	74.29	81.43	84.29	75.71	78.57	84.29
juniper	99.00					
oak	92.00					
overall accuracy	94.12%	90.44%	92.94%	91.32%	92.94%	96.91%
kappa coefficient	0.93	0.87	0.91	0.88	0.91	0.96

III.8 Identifying Shadow Pixels on Aerial Images and Associated Accuracy

Shadow areas on aerial images can result from many factors like image capturing date and time, sensor position, topographic features, and clouds. Revealing shadow areas is of particular importance when the thematic maps are used in hydrological modeling. Therefore, I developed a strategy to identify the true cover of shadow pixels. After obtaining satisfactory accuracy for Landsat image classifications I converted all classes of Landsat thematic maps into ENVI vector files (EVF). Then I converted the EVFs to normal shape files and ROI files, respectively. The Post Classification Editing tool in

ENVI is a very helpful multitasking tool which enables users to import spatial information from external sources in the ROI format. Before converting shadow into associated land use and cover categories using the ROI files I made the following assumptions:

- 1) Any shadow inside the oak savanna ROI file hides the herbaceous vegetation cover. I made this assumption due to the sparse distribution of oaks within the oak savanna areas. Figure 20 shows an oaksavanna vector file derived from Landsat ML classification displayed on sparsely distributed oak trees shown in the aerial image.

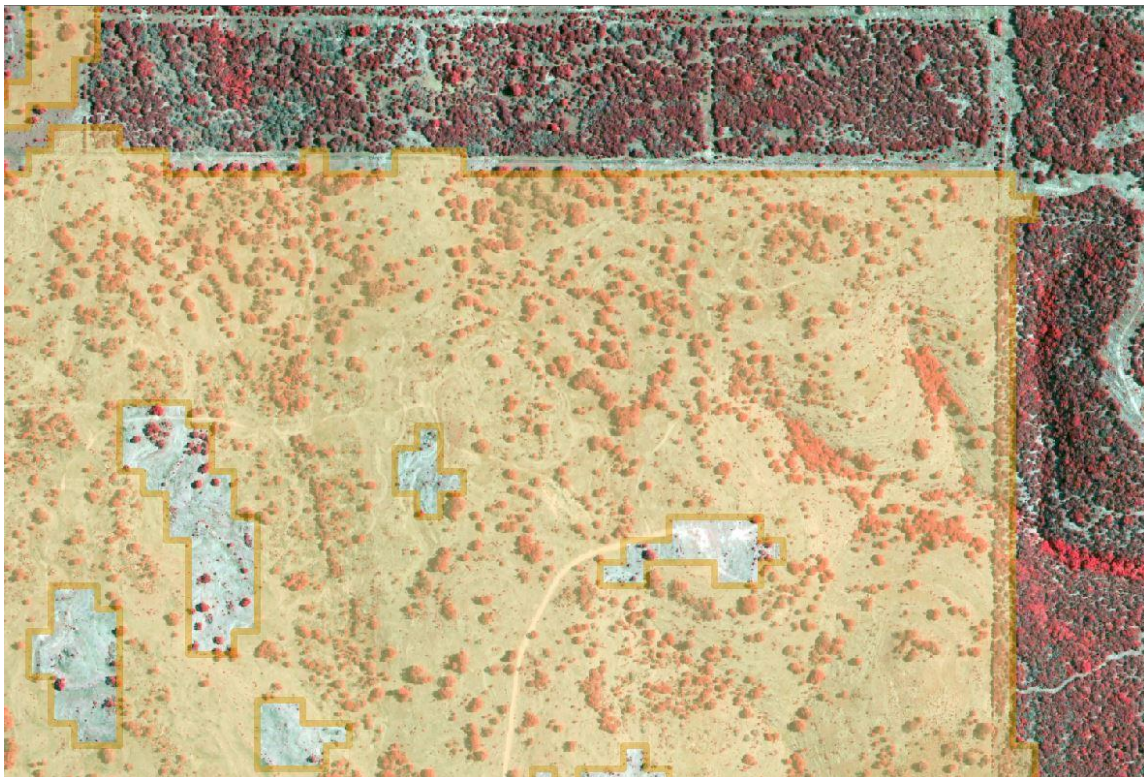


Figure 20. An oaksavanna vector derived from Landsat image classification overlain on the corresponding aerial image.

- 2) Any shadow pixel inside the oak ROI hides oaks.
- 3) Any shadow area inside the juniper ROI is covered by junipers. Although the juniper class is defined to cover at least 25% of the total vegetation area in the classification scheme of the Landsat image, I realized that most of the shadowed pixels are inside the denser canopies of juniper-dominated areas and on higher elevations with steeper slopes where junipers are usually the dominant land cover type.
- 4) Excluding the water ROI, I decided to convert shadow pixels into herbaceous for the rest of the ROI files which had very few shadow pixels. I excluded editing the shadows falling into the water ROI because there was a higher potential for a spatial mismatch of Landsat-derived ROIs due to the coarse resolution. For example, when a stream channel width is about 20 meters, the entire Landsat pixel falls onto this specific location is most probably classified as water. There are riparian hardwood species along the river and they cause shadowed areas within the stream channel or adjacent to the stream channel. So, to prevent this shadow from being edited incorrectly, I had to ignore the shadow pixels along or within the river channel. Figure 20 shows a water vector file derived from Landsat ML classification displayed on a part of the Nueces River.

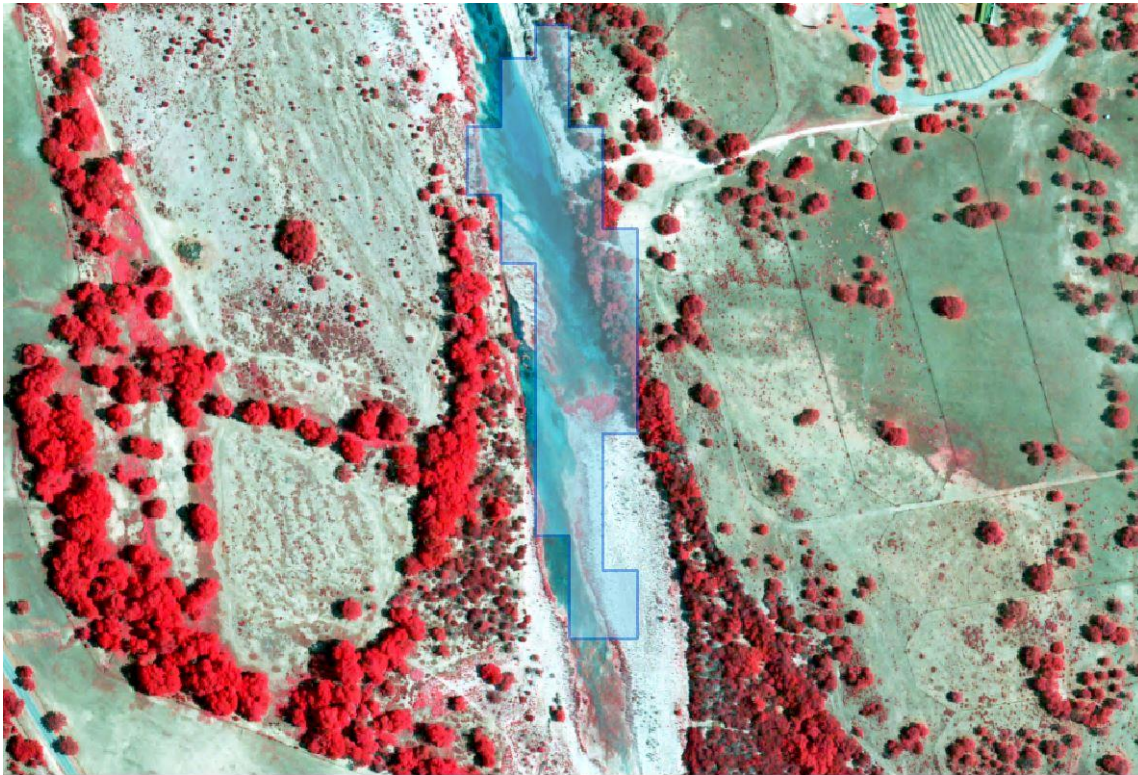


Figure 21. Water vector file derived from Landsat ML classification overlain on the aerial image.

Based on the assumptions made, I edited shadow pixels in ENVI using the ROI files derived from Landsat ML classifications. Figures 22, 23 and 24 demonstrate the process of shadow detection. To test the accuracy and utility of this approach I collected ground truth samples from the tree, herbaceous, oak, and juniper covered areas under shadow cover for a specific image. Because I could only map oak and juniper cover for 2008, juniper and oak ROIs are used for only 2008 image. I identified the cover type of shadow pixels by displaying every year's aerial images on geometrically linked multiple windows in ENVI which is demonstrated by Figure 24.

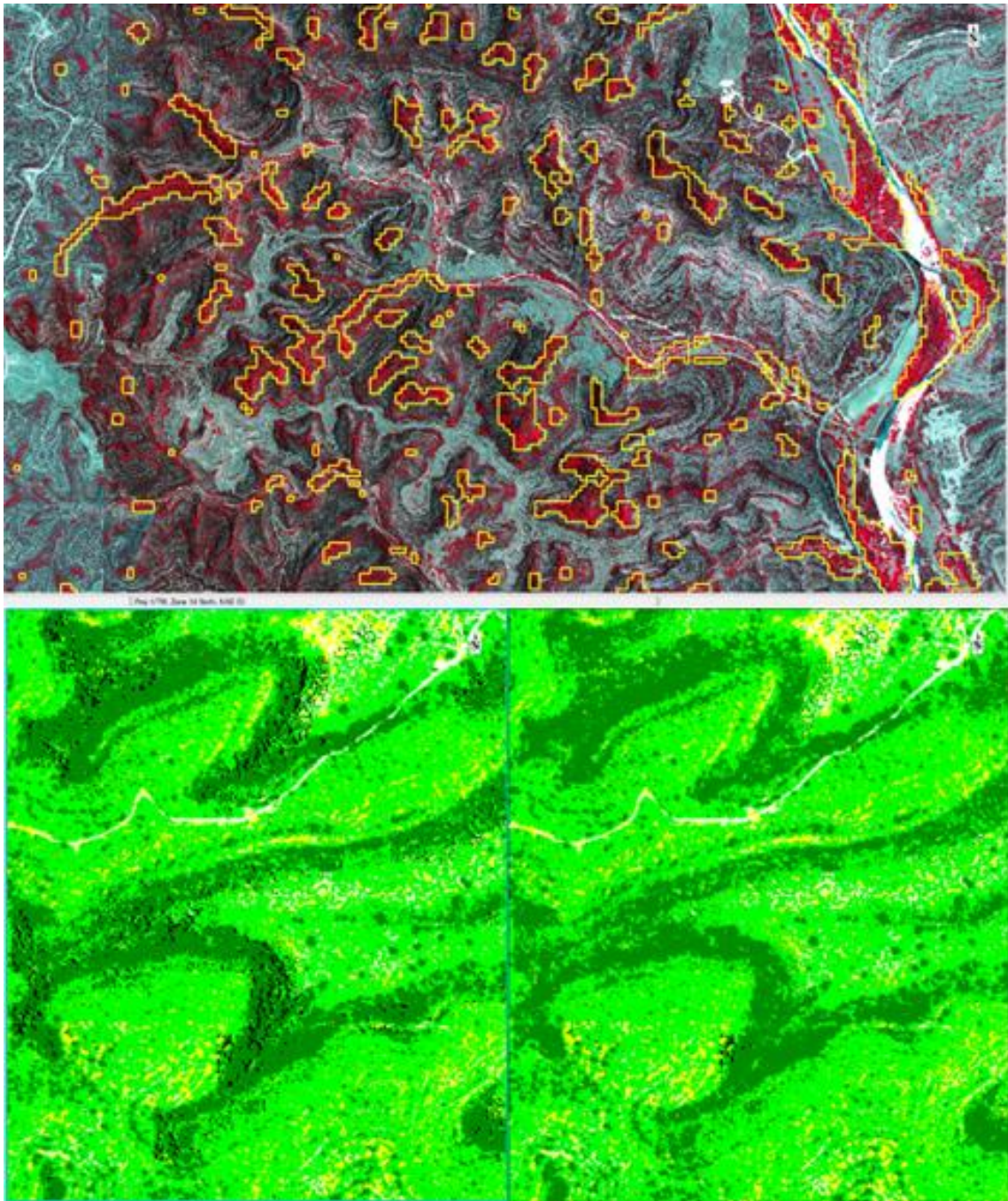


Figure 22. The image on top shows the oak vector file displayed over the NIR false-color composite of 2008 aerial image. The image below indicates the conversion of shadows to oaks on 2008 ML classification of the aerial image utilizing the oak vector file derived from 2008 Landsat ML classification. Darker green represents oaks, and light green color represents juniper trees. Note that the location depicted by the classifications is not the same with the image shown at the top.

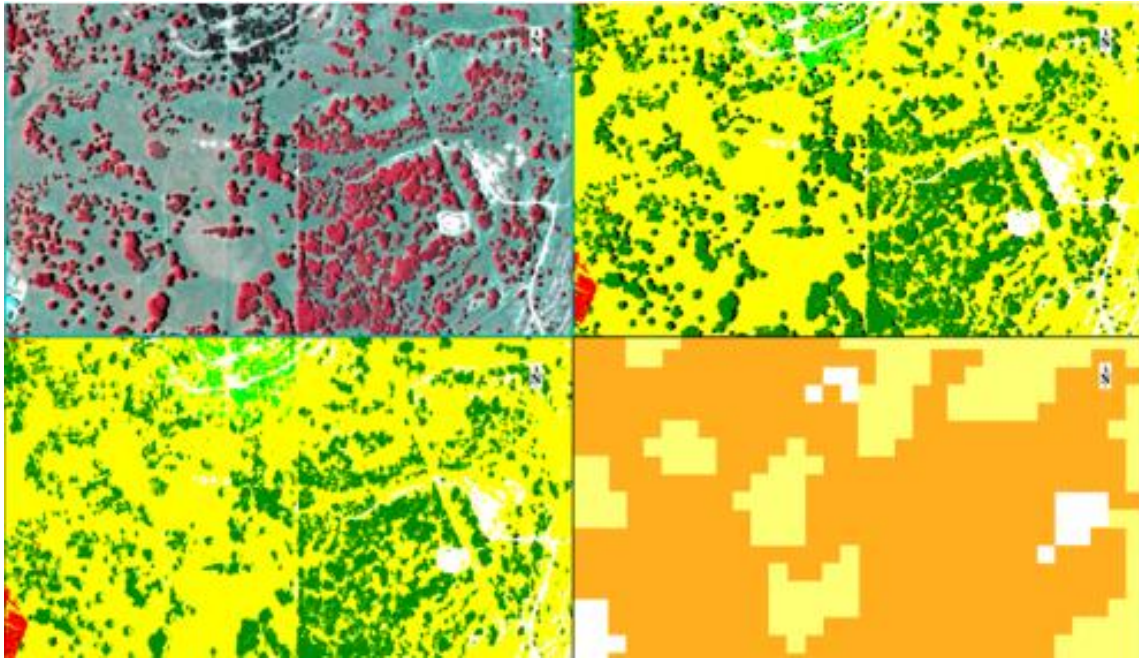


Figure 23. Before (top right) and after (bottom left) shadow detection in 2008 aerial image classifications. The image on the top left is the NIR false-color composite of the 2008 image, the image bottom left is from the TEAM LULC map.

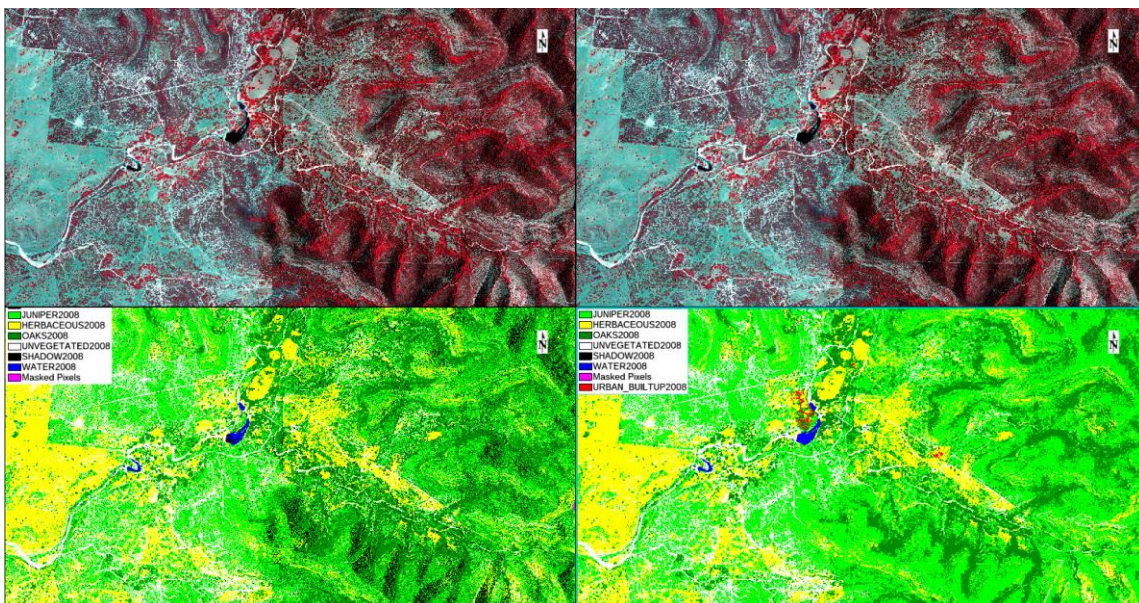


Figure 24. Maximum Likelihood classification of 2008 aerial image before (bottom left) and after (bottom right) shadow editing. The urban area is also finalized after editing shadows.

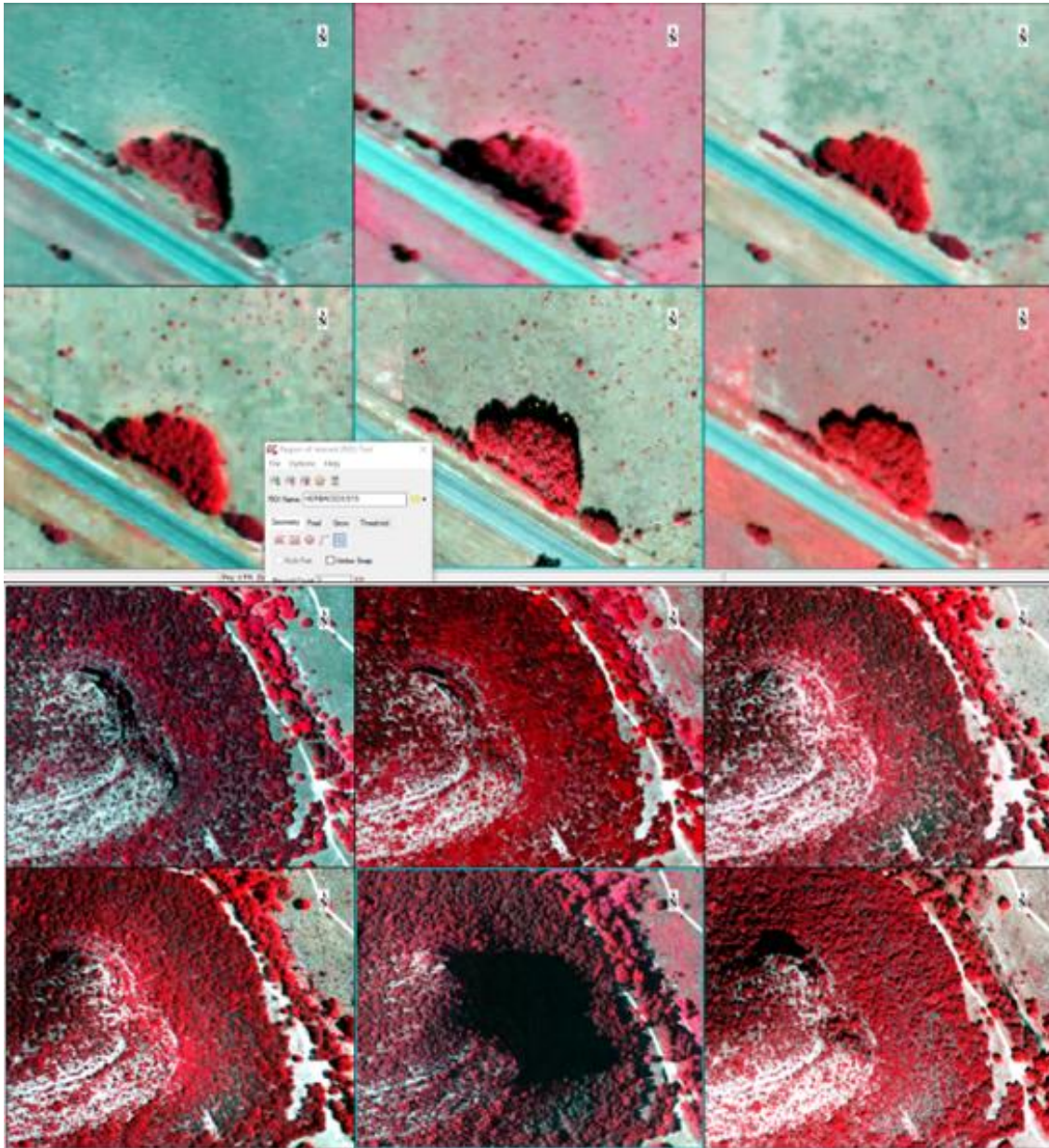


Figure 25. Validation data collection on ENVI for the accuracy assessment of the edited shadow areas. Images in the top row are 2008, 2010, and 2012, and images in the second row are 2014, 2015, and 2016, respectively. All images displayed as near infrared false-color composite.

Table 19. Number of ground truth points collected from shadowed areas.

Class Name	2008	2010	2012	2014	2015	2016
Herbaceous	70	70	70	71	70	70
Juniper	71					
Oak	70					
Tree		70	70	70	70	70

After using reference points shown in Table 19 for the accuracy assessment of shadow detection, I combined them with the initially collected reference points to perform the final accuracy assessment. I also quantified the area of classes converted from shadow cover. After completing all the editing for shadow, I applied a majority filter with a window size of five to every ML classification of aerial images.

III.9 Thematic Change Detection Analysis

Quantification of land use and cover change in the study area was a necessary task for investigating the impact of LULC on the hydrology of the watershed. Computing the change statistics and mapping the spatial configuration of change were achieved using Change Detection Statistics and Thematic Change workflows in the ENVI software. The change detection statistics routine outputs a detailed tabulation of changes between two classification images. The changes can be reported as pixel counts, percentages and areas. To perform a successful change detection analysis, classification images must be georeferenced or co-registered. Co-registration can be done automatically in ENVI using the available map information. I combined juniper and oak classes into the “tree” class to comply with the rest of the classification images. I assumed that any change occurred in the tree cover in the study area can be attributed to juniper control or invasion. I neglected the change in the oak cover based on the site-

specific knowledge obtained from the literature and the visual interpretation of brush control sites. A brush control site is shown in Figure 26 where oak trees were left.

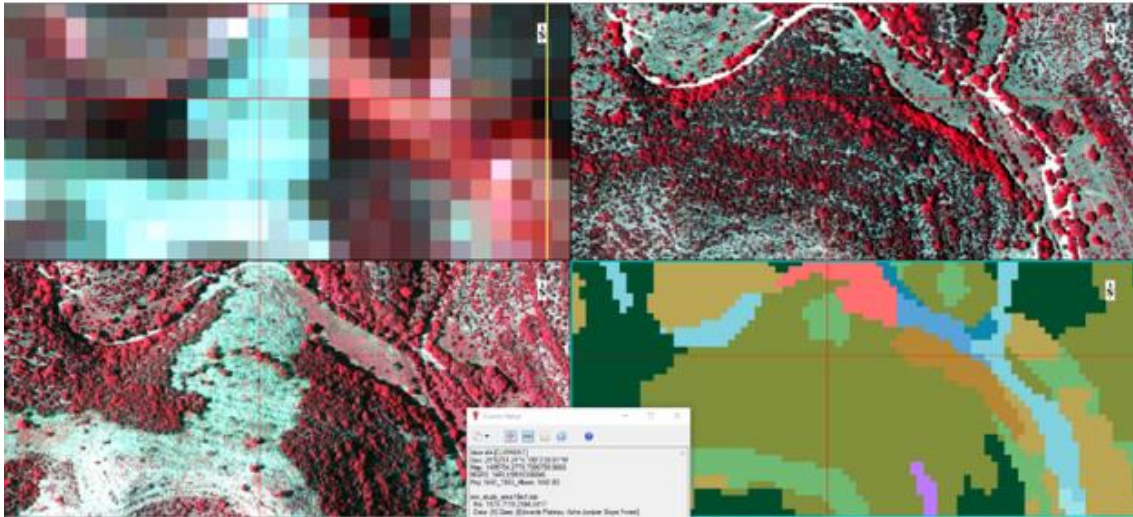


Figure 26. A brush treatment site where junipers were removed, and oaks were left. Images in the left column from top to bottom are 2015 Landsat 8 and 2015 NAIP images, respectively. In the right column are the 2008 TOP image (top) the TEAM dataset (bottom).

In the thematic change detection workflow, the option “don’t show no change area” is automatically activated if the classification categories have the same names for different years. Because I suffixed all class names with the associated year to prevent possible confusion due to multiple-year data, I edited class names using the “edit class names and color” option in the ENVI software. However, the option “don’t show no change area” couldn’t be activated. Therefore, I decided to use suffixes for any class name while performing thematic change detection analysis. The analysis resulted in thematic maps that have more than thirty classes representing the combinations of any

classes in the initial-state and final-state maps. I used “combine classes” in the post classification toolbox to combine any classes indicating no change or negligible change into the “No Change” category.

I realized that the class changes from “herbaceous” to “unvegetated” and from “unvegetated” to “herbaceous” had many pixels. This situation stemmed from the image capturing date. In other words, herbaceous cover at a specific location could be easy or difficult to detect depending on the season when the images were captured. For example, there would be a rigorous herbaceous cover when soil moisture conditions were favorable, but herbaceous cover might not be so obvious during the drought period. Figure 27 shows the seasonal variations among the herbaceous and unvegetated classes.

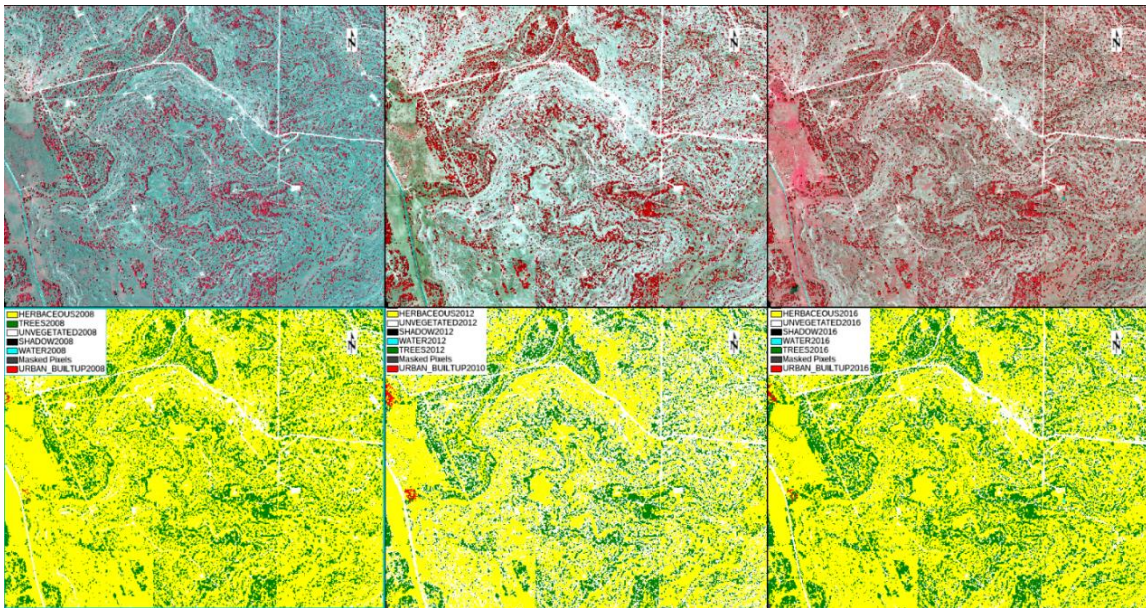


Figure 27. Seasonal changes in unvegetated and herbaceous land covers. Images shown from left to right are 2008, 2012 and 2016 aerial images (above) and corresponding classification images (below).

Because my primary goal was to investigate the impact of changes in woody cover on streamflow, I included the change between herbaceous and unvegetated cover within the “No Change” category. Thus, I calculated change statistics for the following classes:

- i. Herbaceous to Tree
- ii. Unvegetated to Tree
- iii. Tree to Herbaceous
- iv. Tree to Unvegetated

After having change and no change classes, I applied post classification aggregation to highlight the brush control areas. Deciding which window size was suitable required several iterations. I tested multiple window sizes from very small to large and compared them visually to align aerial image series with the associated classifications. Finally, I decided to use a window of 250 m after many iterations. Figure 28 demonstrates the results of different iterations with relatively small window sizes.

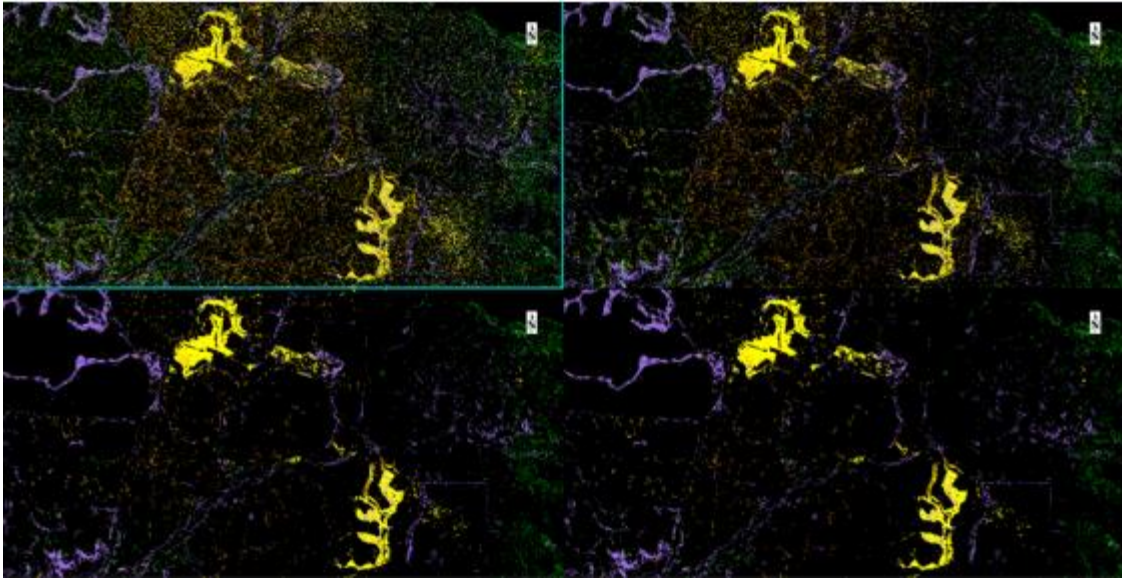


Figure 28. Iterations to find the best window size for post classification thematic change aggregation.

III.10 Analyzing the Relationship Between Mapped Tree Cover, Interpolated Rainfall and Measured Streamflow

After processing all the data, I quantified tree cover for six years, annual rainfall from 2008 to 2017 for each year and obtained the measured streamflow from 2009 to 2017. I tested the impact of two variables, annual tree cover and annual rainfall (independent variables), on the streamflow (dependent variable) using multi-regression analysis. I used the JMP statistical analysis software to perform this analysis. The statistical testing results were evaluated at a 95% confidence level. I also analyzed the linear relationships between rainfall and water yield and between tree cover and water yield separately. I used the 2008 LULC map to associate with the 2009 rainfall and water yield because the streamflow data was only available after 2009.

III.11 Modeling the Hydrological Impact of LULC Change

The SWAT model was used in this study to investigate the ramifications of the land use and cover change on water yield. My primary goal was to achieve acceptable uncertainty estimates for the model calibration and validation. The model is primarily used to simulate ET, surface run-off, percolation, lateral flow, groundwater flow (return flow), and transmission losses [24]. These hydrological components are calculated using the daily equation below:

$$SW_t = SW_0 + \sum(R_{day} - SURQ - E_a - W_{seep} - GWQ)$$

where SW_t is the final soil water content (mm), SW_0 is the initial soil water content (mm), t is the time (days), R_{day} is the amount of daily precipitation (mm/day), $SURQ$ is the amount of surface runoff (mm), E_a is the amount of ET (mm), W_{seep} is the amount of water penetrating the vadose zone from the soil profile (mm), and GWQ is the amount of groundwater flow (mm). To estimate surface run-off, run-off curve number methods were used. The Net Water Yield (WYLD) was calculated as follows:

$$WYLD = SURQ + LATQ + GWFQ - TLOSS$$

where $LATQ$ is the lateral flow (mm), and $TLOSS$ is the transmission loss (mm). The SWAT uses the exponential function of soil depth and moisture to measure evaporation and a linear function of Potential Evapotranspiration (PET) and Leaf Area Index (LAI) while computing transpiration [75].

The Nash-Sutcliffe model efficiency (NSE) and the Coefficient of the Determination (R^2) are oftentimes utilized to evaluate the performance of the model estimations [76]. The value of R^2 is between 0 and 1. It assesses the goodness of fit

between the simulated data and the observed data. The value of 1 indicates the best fit while 0 means no correlation between them. Most of the hydrological studies use NSE to test the model performance [77]. While the value of NSE ranges from negative infinity ($-\infty$) to 1, a value of 1 for NSE indicates the perfect fit between the measured and simulated data. The minimum acceptable R^2 value should be 0.60 while it should be at least 0.50 for the NSE [76, 78]. R^2 and NSE are computed by the following equations, respectively:

$$R^2 = \left[\frac{\sum_{i=1}^n (Q_{obs} - \overline{Q_{obs}})(Q_{sim} - \overline{Q_{sim}})}{[\sum_{i=1}^n (Q_{obs} - \overline{Q_{obs}})^2]^{0.5} [\sum_{i=1}^n (Q_{sim} - \overline{Q_{sim}})^2]^{0.5}} \right]$$

$$NSE = \left[1 - \frac{\sum_{i=1}^n (Q_{sim} - Q_{obs})^2}{\sum_{i=1}^n (Q_{obs} - \overline{Q_{obs}})^2} \right]$$

where Q_{obs} and $\overline{Q_{obs}}$ are the observed value and the mean of the observed data, respectively, and Q_{sim} and $\overline{Q_{sim}}$ are simulated and the mean of simulated data, respectively.

Following the completion of the LULC classifications and change detection analysis, I used the land use and cover data to set up the SWAT models. I decided to construct multiple SWAT models to account for the changes occurred from 2009 to 2017. Because there was a lack of 2009 LULC data, I used the 2008 LULC map instead. I divided the data into three subsets for model warmup, calibration, and validation, respectively. Specifying a few years (2 to 5) as the model warmup period is a recommended measure to allow the model to adjust parameters to the conditions of the study area. No simulation result was outputted for the warmup period. I decided to leave the 2008-2011 period as the warmup period for the model calibration. This decision was

reasonable given that there was no streamflow record for 2008. The calibration data covered the period from 2012 to 2015. The validation data covered the 2016-2017 period. The processes described hereafter includes the setups of the SWAT model calibration, validation, and simulation.

III.12 Model Setup and Watershed Delineation

I used ArcSWAT version 2012 for my modeling purposes. The 2012 version of the SWAT can work on ArcGIS 10.4 and preceding versions. My first SWAT project was devised for the calibration period. Automatic watershed delineation workflow was used to delineate a basin into subbasins. A digital elevation model was required to compute flow direction and flow accumulation. So, a stream network can be created following these steps if a predefined stream network isn't available or not preferred. Although I obtained the National Hydrography Dataset from the USGS, I preferred to use the 10-meter DEM to let the model create a stream network to avoid any potential error. After the model created the stream network I determined the whole watershed outlet based on the location of the streamflow measuring gage (USGS 0818999010 Nueces Rv Nr Barksdale). The basin area was calculated to be 350 square miles. The drainage area was divided into 31 subbasins by the model. Then, the model calculated subbasin parameters and completed the watershed delineation process. Figure 29 shows the resulting subbasins after watershed delineation process in the SWAT-NAIP models.

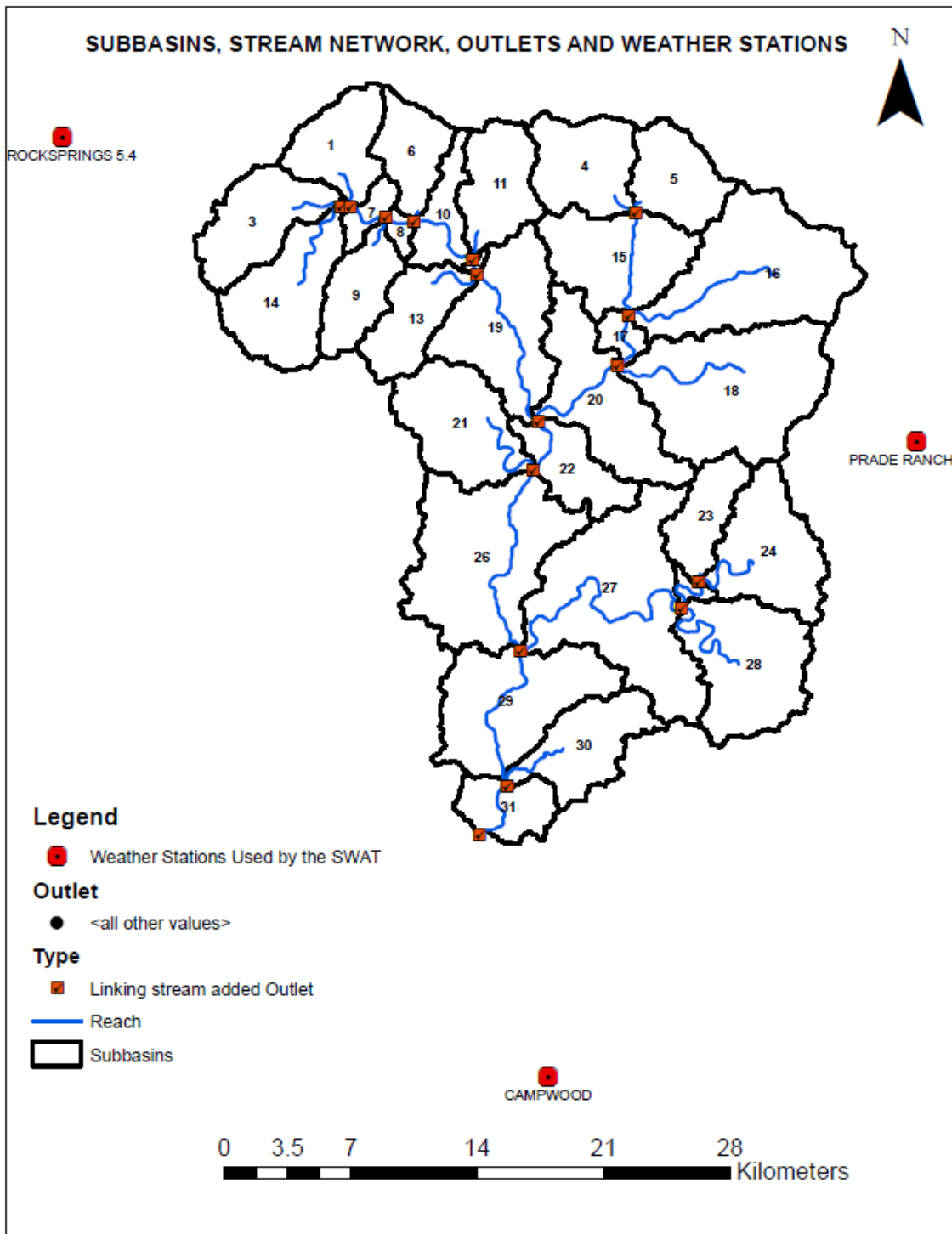


Figure 29. The stream network and delineated watershed. The three weather stations used by SWAT are the closest ones to the study area out of 8 stations inputted to the model.

Multiple models were set in this study. The models created with the use of the thematic maps derived from the NAIP aerial images were named as SWAT-NAIP and classified into two categories depending on whether the crack flow code was active. The models having the active crack flow were in the pre-processed category while the remaining SWAT-NAIP models with the inactive crack flow were placed under the default model category. The models based on the Landsat and NLCD LULC datasets were named as SWAT-LANDSAT and SWAT-NLCD, respectively, and they were placed in the default model category. All the SWAT models were set up are shown in Table 20.

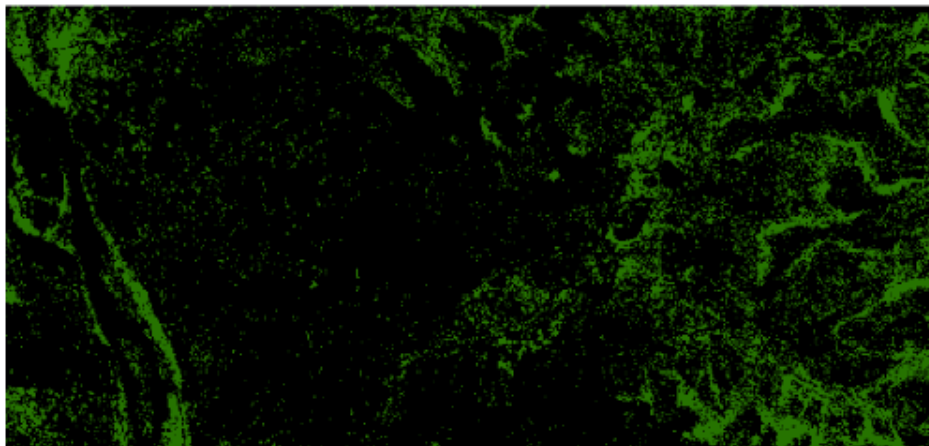
Table 20. All SWAT models set in this study.

#	MODEL GROUP	MODEL NAME	TYPE	PERIOD	WRM UP	DEM (m)	SUBS.	HRU
1	pre-prc.	SWAT-NAIP	calibration	2012-2015	4	10.31	31	1239
2			validation	2016-2017	0-4	10.31	31	1201
3		SWAT-NAIP	calibration	2012-2015	4	10.31	31	1239
4			validation	2016-2017	4	10.31	31	1201
5	default	SWAT-LANDSAT	calibration	2012-2015	4	28.97	35	851
6			validation	2016-2017	4	28.97	35	851
7		SWAT-NLCD	validation	2012-2015	4	28.97	35	875
8		SWAT-NAIP	verification	2009-2011	1	10.31	31	1207
9		SWAT-NAIP	scenario	2009-2011	1	10.31	31	1044

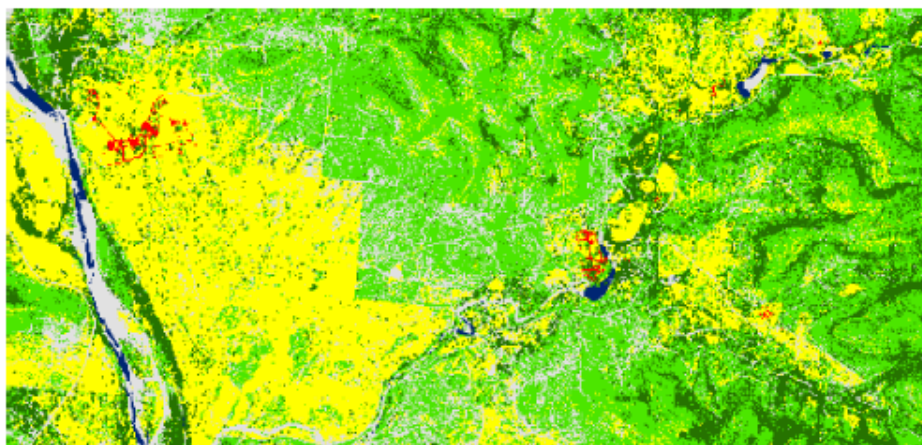
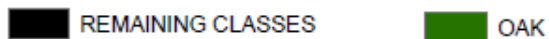
III.13 Hydrologic Response Unit (HRU) Analysis

An HRU is a unique combination of land use cover, soil, and slope. The hydrological response of these units varies significantly depending on the type of the combination. Before inputting LULC thematic maps into land use/soils/slope definition workflow I reclassified and resampled them respectively. Because the resolution of the DEM data defines the resolution of the SWAT model, resampling thematic maps improved the computational speed of the model. The nearest neighbor method was used when resampling the raster datasets. Thereby, the new spatial resolution of the LULC raster datasets matched the resolution of the DEM. I created an “oak mask” in ArcGIS using 2008 aerial image classification. Figure 30 demonstrates the extraction of the 2008 oak cover. I reclassified the resampled 2008 LULC raster data using spatial analyst tools. I converted the value of oak to “0” and the value of all the other classes to “1”. Later, I multiplied the resampled 2012 and 2016 LULC raster datasets with this mask raster. So, the area represented by “0” in the new 2012 and 2016 maps was the same oak area in the 2008 map. Using spatial analyst tools in ArcGIS I reclassified the 2012 and 2016 LULC data and converted the value of 0 into 3 (oak class value in 2008) and all the remaining tree class (value=5) into the juniper class (value=1). I matched the class values of 2008, 2012 and 2016 images and created a land use cover lookup table which is shown in Table 21 to prompt the SWAT model to import the LULC data.

EXTRACTION OF 2008 OAK COVER



Legend 2008 Oak Mask Class Name



Legend 2008 Aerial Image Classification Class_Name



1:39,678

Figure 30. Masking out the oak cover of the 2008 thematic map.

Table 21. Class names and values of the produced thematic maps and corresponding SWAT LULC codes.

VALUE	CLASS NAME	SWAT LAND USE CODE
1	JUNIPER	JUNI
2	HERBACEOUS	RNGE
3	OAK	OAK
4	BARREN	BARR
6	WATER	WATR
7	URBAN/BULTUP	URML (Urban Medium Low Density)

The SWAT model plant database didn't have juniper data. However, Dr. Raghavan Srinivasan who is one of the important contributors and developers of the SWAT model provided me with the juniper database which is shown in Table 22. I had to update the plant database in the model using this dataset. However, hydrological parameters of the plant like the Soil Conservation Service (SCS) curve numbers (CN2) for soil moisture condition and Canopy Maximum Storage (CANMAX) weren't included in the provided dataset. So, I determined juniper hydrological parameters based on the literature [18]. The Soil Survey Geographic dataset (SSURGO) is recognized by the model. However, the SSURGO dataset was also missing in the 2012 version of the SWAT soil database. I downloaded the ArcSWAT12 SSURGO database from the website of the model and loaded the folder into the project database directory. Later, I resampled and projected the SSURGO dataset to match the spatial resolution and projection (NAD1983 UTM Zone 14N) of the DEM and LULC datasets.

Table 22. Biophysical parameter database of the juniper.

Land cover/plant code	JUNI	
Land cover/plant classification	Warm season perennial (6)	
Crop Name	JUNIPER	
Plant Biophysical Parameters	Description	Value
BIO_E	Radiation use efficiency (kg/ha)/(MJ/m**2)	16
HVSTC	Harvest index	0.01
BLAIC	Maximum potential leaf area index	12
FRGRW1	Fraction total PHU at 1st point on leaf dev. curve	0.2
LAIMX1	Fraction BLAI at 1st point on leaf dev. curve	0.2
FRGRW2	Fraction total PHU at 2nd point on leaf dev. curve	0.99
LAIMX2	Fraction BLAI at 2nd point on leaf dev. curve	0.99
DLAIC	Fraction of growing season when leaf area declines	0.99
CHTMXC	Maximum canopy height (m)	12
RDMXC	Maximum root depth (m)	3.5
TOPT	Optimal temperature for plant growth (deg C)	30
TBASE	Minimum (base) temperature for plant growth (deg C)	10
CNYLDC	Normal fraction of nitrogen in yield (kg N/kg yield)	0.0015
CPYLDC	Normal fraction of phosphorus in yield (kg P/kg yield)	0.0003
BN1	N fraction in plant at emergence	0.006
BN2	N fraction in plant at 50% maturity	0.002
BN3	N fraction in plant at maturity	0.0015
BP1C	P fraction in plant at emergence	0.0007
BP2C	P fraction in plant at 50% maturity	0.0004
BP3C	P fraction in plant at maturity	0.0003
WSYFC	Lower limit of harvest index	0
USLE_C	Minimum value of USLE C factor for water erosion	0.001
GSIC	Maximum stomatal conductance (m/s)	0.007
VPDFR	Threshold vapor pressure deficit (VPD) (kPa)	-3.5
FRGMAX	Decline in BIO_E per unit increase in VPD	1
WAVPC	Decline in leaf conductance per unit increase in VPD	8
CO2HI	Elevated CO2 atmospheric concentration (uL CO2/L air)	660

Table 22 continued

Land cover/plant code	JUNI	
Land cover/plant classification	Warm season perennial (6)	
Crop Name	JUNIPER	
Plant Biophysical Parameters	Description	Value
BIOEHI	Biomass-energy ratio corresponding to CO2HI	15
RSDCOPL	Plant residue decomposition coefficient	0.05
ALAIMIN	Minimum LAI during winter dormant period	0.75
BIOLEAF	Fraction of biomass accumulated each year	0.3
MAT_YRS	No of yrs req for tree species to reach full development	50
BMX_TREES	Maximum biomass for a forest (metric tons/ha)	1000
EXT_COEF	Light extinction coefficient	0.37
BMDIEOFF	Fraction above ground biomass that dies	0.1

Updating the plant and soil database of the SWAT model version 2012, I inputted the LULC and SSURGO data into the model. After LULC codes were imported from the look-up file, the model reclassified LULC data. For calibration and validation of the model, 2012 and 2016 LULC data were used. For scenario simulation 2008 LULC data derived from the ML classification of aerial image was used. Figure 31 shows the entire 2008 LULC map for the study area. Map Unit Key (mukey) is the attribute of the SSURGO dataset which was recognized by the model. Since I converted the SSURGO data from feature class to raster by specifying mukey as the raster value, the SWAT model easily matched the associated soil attributes.

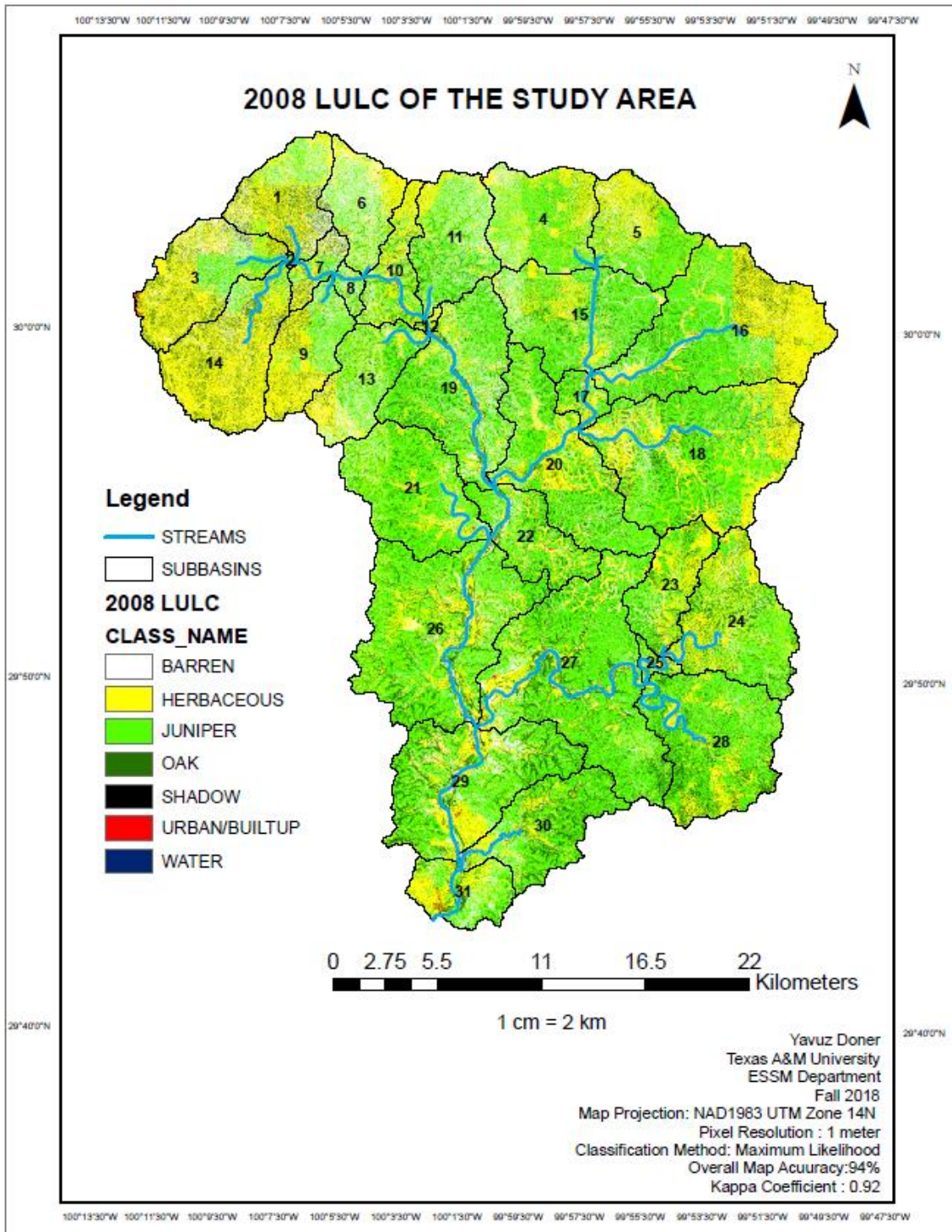


Figure 31. Land use and cover of the study area derived from the 2008 aerial image.

The last step was to define the slope gradient to complete land use/soils/slope definition workflow. I specified multiple slopes. I divided slope into five categories based on the slope gradient classification of the United States Department of Agriculture (USDA). The slope gradients and their range are shown in Table 23. Figure 32 shows the distribution of the slope gradients in the entire study area. Following the reclassification of land use cover, soil, and slope, the model overlaid all the input data to generate unique combinations.

Table 23. Slope classes generated for land use/soil/slope definition.

Slope Number	Slope Level (%)	Class
1	0-3	Flat
2	3-9	Gentle
3	9-15	Moderate
4	15-35	Steep
5	>35	Extremely Steep

I used the HRU definition tool to produce final HRUs for the model. I selected the multiple-HRUs option to specify thresholds for final HRU generation. Thresholds can be specified in either percentage or area. Land use is the base layer and soil threshold applies the soils on the land use cover which is over the specified land use threshold. Following this, slope threshold applies to the remaining slopes on the land use and soils.

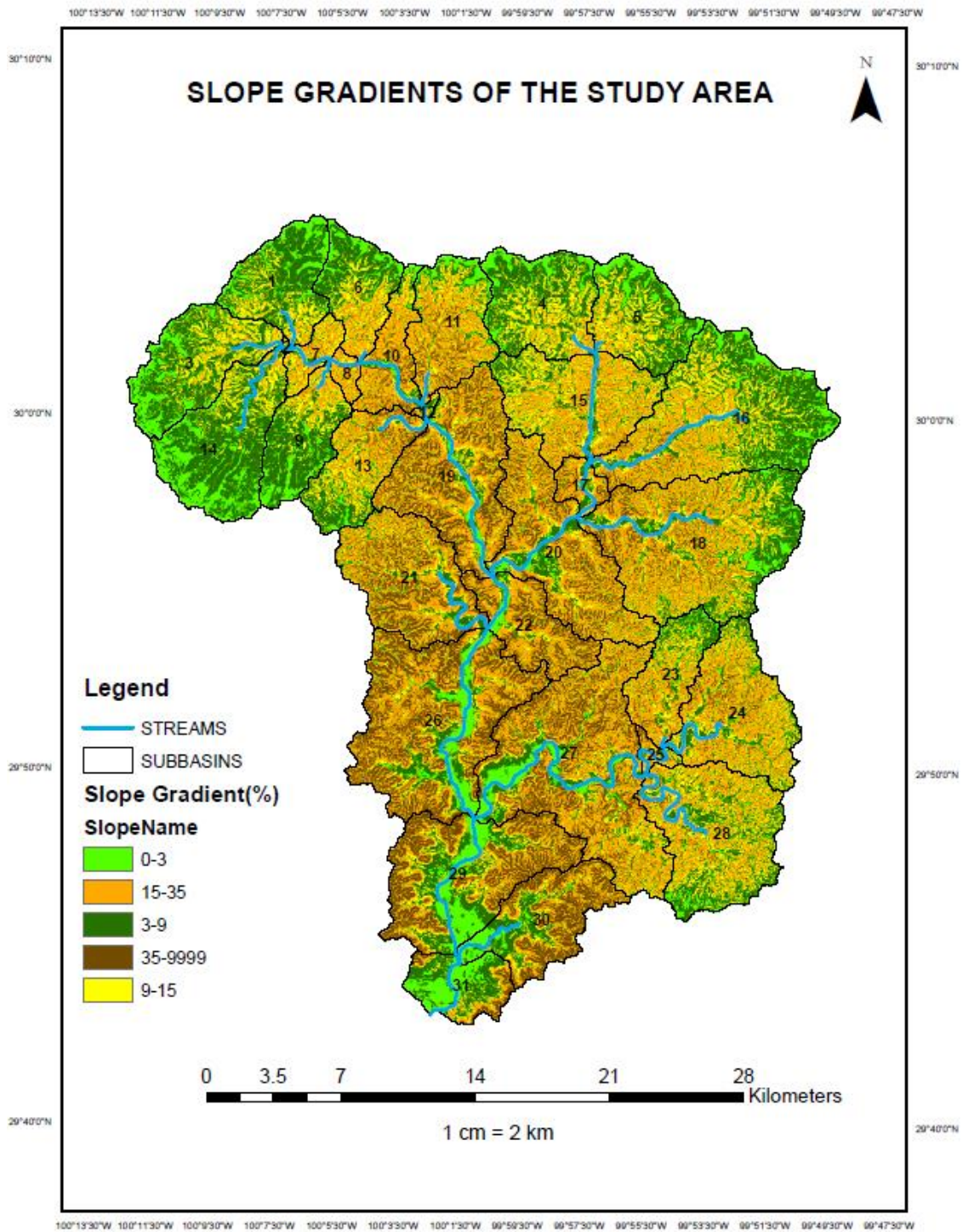


Figure 32. The slope categories of the study area.

The default thresholds for land use, soil, and slope were 20%, 10%, and 20%, respectively. However, I specified 10%, 5% and 5% thresholds for land use, soil, and slope, respectively, to increase the representation of the land use, soil, and slope. Since the mean subbasin area was around 29 km², the 10% land use threshold was crossed by major LULC classes (juniper, oak, herbaceous and barren). The representability of the watershed characteristics by the created HRUs was very high (90% to 100%). Figure 33 shows the model's LULC, soil and slope report for the SWAT-NAIP model calibration.

SWAT model simulation Date: 9/27/2018 12:00:00 AM Time: 00:00:00
 MULTIPLE HRUs LandUse/Soil/Slope OPTION THRESHOLDS : 10 / 5 / 5 [%]
 Number of HRUs: 1239
 Number of Subbasins: 31

		Area [ha]	Area[acres]	
Watershed		90643.0769	223983.5752	
LANDUSE:		Area [ha]	Area[acres]	%Wat.Area
	Juniper --> JUNI	36702.0953	90692.7126	40.49
	Range-Grasses --> RNGE	19677.2193	48623.3926	21.71
	Oak --> OAK	11588.9689	28636.9216	12.79
	Barren --> BARR	22674.7935	56030.5484	25.02
SOILS:				
	374292	37682.5916	93115.5680	41.57
	374307	1484.2733	3667.7135	1.64
	374318	75.4172	186.3597	0.08
	374290	2496.2203	6168.2851	2.75
	374291	2279.8161	5633.5397	2.52
	374316	178.4713	441.0115	0.20
	374293	39042.4075	96475.7410	43.07
	374308	892.4068	2205.1818	0.98
	374302	446.1217	1102.3891	0.49
	374305	30.9546	76.4904	0.03
	374317	34.6998	85.7449	0.04
	374288	355.9157	879.4856	0.39
	374310	3191.0994	7885.3662	3.52
	374303	1858.9655	4593.5967	2.05
	374313	200.2864	494.9176	0.22
	374309	245.5057	606.6570	0.27
	374304	120.7946	298.4896	0.13
	374298	27.1293	67.0377	0.03
SLOPE:				
	0-3	8725.0584	21560.0555	9.63
	9-15	15708.5008	38816.4910	17.33
	3-9	23191.2111	57306.6422	25.59
	15-35	28986.2610	71626.5001	31.98
	35-9999	14032.0457	34673.8864	15.48

Figure 33. Final HRU distribution for the calibration model (2012-2015) in the study area.

III.14 Writing Input Tables

The SWAT model can use either observed or simulated weather data. The US Weather Generator first-order (WGEN US First Order) monthly weather database including 1041 stations for the entire US can be used to simulate monthly rainfall, temperature, solar radiation, wind speed, and relative humidity. However, this weather data is only available until 2014. Rainfall and temperature are two key weather data required by the model. I imported observed daily rainfall and temperature data. Two lookup files defining the name, longitude, latitude, and elevation of the precipitation and temperature stations were also needed. Separate text files had to be prepared for the temperature and precipitation records of different stations. The names of the stations were given to the corresponding files so that the model could extract the data via the use of the station's lookup file. The daily temperature and precipitation data must be entered in a sequential order. Only the initial date of the measured data can be specified on top of the column. The first day of the weather data was accepted as the starting date of the simulation. The weather data obtained from the National Climatic Data Center (NCDC) was in the metric format and daily time step. I noted that there was some missing data for eight stations. The SWAT model can interpolate gaps in the weather data if a “-99” value specified. So, in Excel, I identified missing dates for each station and filled these gaps with “-99”. However, after running the model I realized that most of the “-99” s caused an error when the weather data was created and led to very excessive rainfall estimates. After talking to Dr. Srinivasan, I prepared weather data from scratch by interpolating missing dates’ data from other stations. Fortunately, almost no missing date

of a station coincided with the missing date of other stations. I used the average precipitation and temperature of other stations to fill the gaps. Then I prompted the model to write all the input tables to the current project database. Figure 34 shows the model input tables. After writing all parameters to the project database, I was ready to run the model. The first model was built for calibration which covered the 2012-2015 period. Four years were specified as Number of Years to Skip (NYSKIP) which was the period of the model warm-up. I ran all models in a monthly time step. Figure 35 shows the model configuration for the SWAT-NAIP calibration.

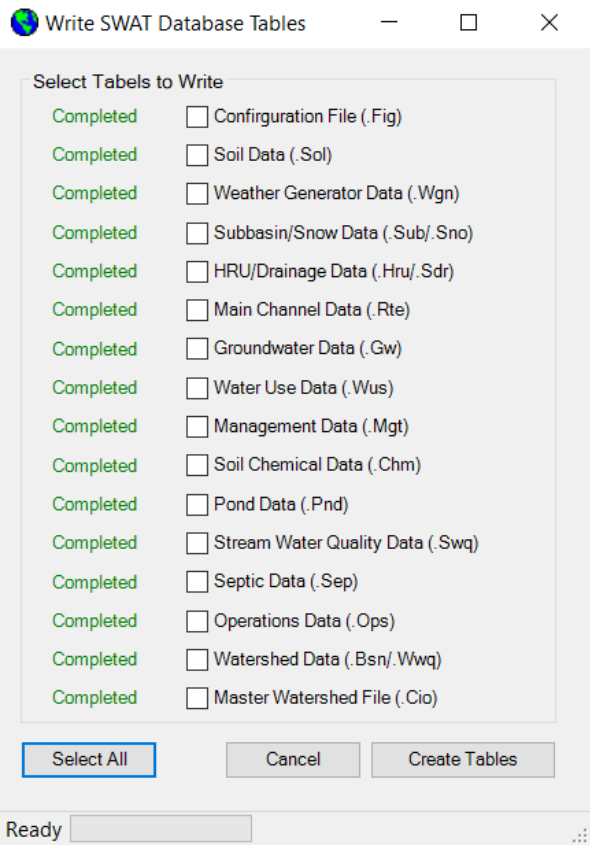


Figure 34. The SWAT model input tables.

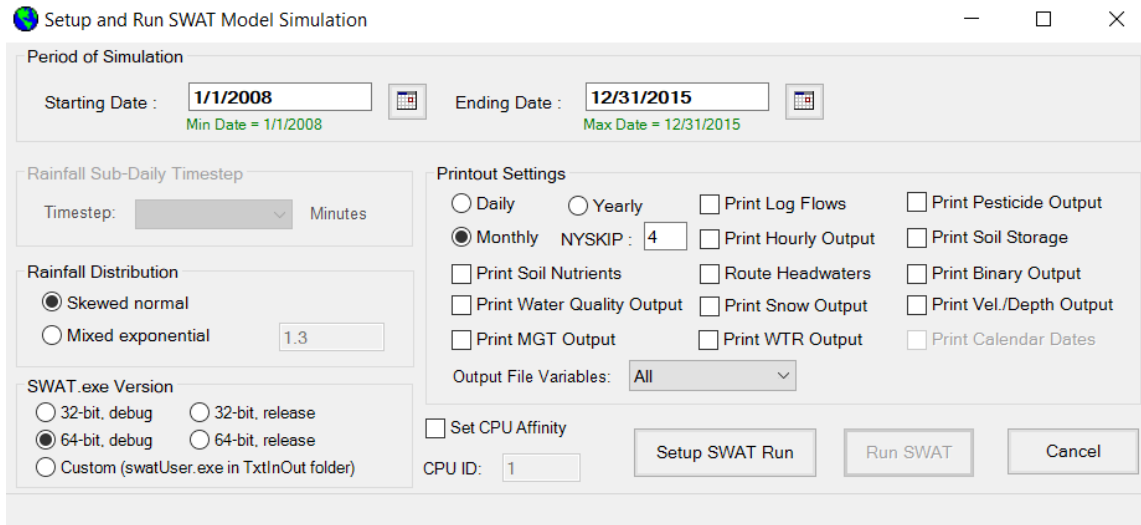


Figure 35. The calibration period model configuration.

III.15 Calibration and Validation of the SWAT Model

The model calibration can be done manually, automatically or with the combination of both. The complex nature of the hydrological model due to the substantial number of parameters involved in the representation of the biogeochemical and hydrological processes make calibration a very challenging task. The default parameters in the SWAT project database were based on the experimental studies and published records. Parameter values can vary significantly from one watershed to another due to the site-specific hydrological response of different regions. Thus, parameters in the SWAT model are given an uncertainty range. However, any calibrated parameter value should be within the minimum and maximum limits. SWAT-CUP is an automatic calibration program which was devised to calibrate and validate the SWAT projects. Absolute SWAT values available in the SWAT-CUP project guide users to

check if the calibrated parameter within the reasonable range. Table 24 shows the absolute range of the parameters which were adjusted throughout the calibration of the model.

Table 24. The absolute range and definitions of the 15 parameters.

Parameters	Absolute Range		Description of The Parameters		
	Min	Max			
gw	1	rchrg_deep	0.00	1.00	Deep aquifer percolation fraction.
	2	gwqmn	0.00	5000	Threshold depth of water in the shallow aquifer required for return flow to occur (mm).
	3	alpha_bf	0.00	1.00	Baseflow alpha factor (days).
	4	gw_delay	0.00	500	Groundwater delay (days).
	5	revapmn	0.00	500	Threshold depth of water in the shallow aquifer for "revap" to occur (mm).
	6	gw_revap	0.02	0.20	Groundwater "revap" coefficient.
hru	7	ovn	0.01	30	Manning's "n" value for overland flow.
	8	canmax	0.00	100	Maximum canopy storage.
	9	surlag	0.05	24	Surface runoff lag time.
	10	esco	0.00	1.00	Soil evaporation compensation factor.
sol	11	sol_awl	0.00	1.00	Available water capacity of the soil layer(mm/mm)
	12	sol_k	0.00	2000	Saturated hydraulic conductivity(mm/hr)
mgt	13	cn2	17.00	98	SCS runoff curve number
sub	14	ch_k1	0.00	300	Effective hydraulic conductivity in tributary channel alluvium.
rte	15	ch_k2	-0.01	500	Effective hydraulic conductivity in main channel alluvium.

After the initial runs of the model, I created the SWAT-CUP SUFI2 project. My initial iterations using the parameters commonly reported by many studies weren't satisfactory. While R^2 was over 0.6 for most of the iterations, the NSE value remained below 0. The best-simulated mean flow was more than three-fold of the observed mean flow for the 2012-2015 period. Later, I found that Jain et al. (2015) also studied the Nueces Headwaters Basin and identified subbasins with no flow and subbasins with springs and sinkholes. They parameterized their model to account for the distinctive characteristics of the karst watershed. Hence, I identified the losing streams and sinkholes for each subbasin from the aerial images. Thereby, I adopted the approach of Jain et al. (2015) and defined distinct parameter ranges for the subbasins having sustained flow throughout the year and the subbasins with no observed surface flow in the stream channel. Figure 36 demonstrates the spatial distribution of the subbasins with continuous stream flow and the subbasins with losing streams.

Before parameterizing the model automatically, I conducted initial manual calibration to familiarize myself with the hydrological processes taking place in the study area. I performed eight iterations until I felt the preprocessed model was ready for autocalibration. Table 25 shows the steps of the manual calibration process. The first iteration didn't include any change to the parameters. Besides, I didn't define a warm-up period for the first iteration to compare the result to that of the following iteration having a 4-year warm-up period. The second iteration had a 4-year warm-up period, but no change was made to the parameters.

SUBBASINS WITH LOSING STREAMS AND SUSTAINED FLOW

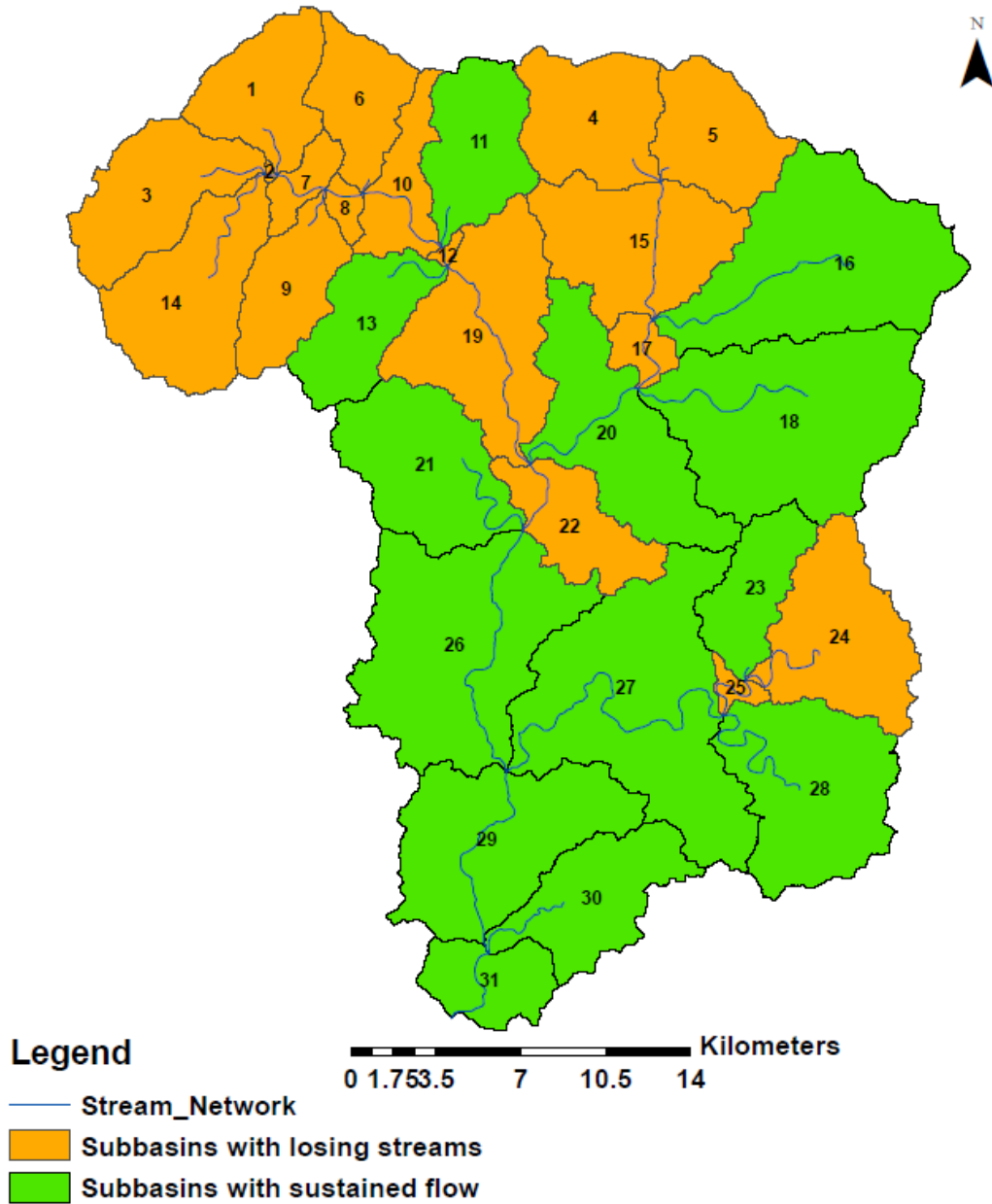


Figure 36. The subbasins with losing streams and subbasins with sustained flow.

Table 25. Manual calibration processes summarized in this table.

Steps	Description	Mean Sim.Flow w(m³/se)	Mean Obsrvd Flow(m³/s)	R Square
Iter1	No warm-up period was specified. The model was run for the 2008-2015 period. All parameters were default except Runoff Coefficient (CN2) parameters for juniper. Values were reported for 2012-2015.	7.05	0.92	0.61
Iter2	Four- year warm up period defined: 2008-2011. Calibration period: 2012-2015	7.05	0.92	0.61
Iter3	Crack flow was activated	6.77	0.92	0.76
Iter4	The deep aquifer percolation (rchrg_deep) parameter was increased to 0.7 from the default value (0.05).	6.28	0.92	0.68
Iter5	Ground water (gw) parameters adjusted to increase baseflow (revapmin, gwqmin,gw_delay, alpha_bf)	7.62	0.92	0.70
Iter6	Soil available water capacity (sol_awl) was increased to maximum. Saturated hydraulic conductivity (sol_k) was decreased to minimum	4.83	0.92	0.76
Iter7	Hydrologic response unit (hru) parameters were adjusted (canmax,esco,ovn and surlag) for OAK, JUNI, BARR and RNGE categories.	3.59	0.92	0.78
Iter8	Based on the preceding simulations, every parameter that had made notable change to the model results were adjusted. Soil parameters were adjusted based on the hydrological group and cared for the spatial characteristics of different soil types.	3.80	0.92	0.79

I monitored the results using SwatCeck module which reads outputted results through the output.std file and illustrates results on a schematic representation of the hydrological processes. I imported the resulting reach file to the Scenarios-Tables out-SwatOutput database where I filtered the subbasins and singled out the subbasin 31,

which has the whole watershed outlet. Thus, I extracted the cumulative flow for the calibration period. I used the cumulative flow outputted by each iteration to investigate the correlation between the simulated flow and the observed flow. In Excel, I calculated R^2 of the regression analysis and averages of the observed and simulated flows to compare the results of manual calibration iterations. The first two iterations produced the same results. I realized that the predicted surface runoff was far above the observed surface runoff values derived from the hydrograph separation analysis.

The results of the hydrograph separation were very helpful for comparing simulated hydrological responses. To understand the relative contributions of baseflow and surface runoff to total flow, I adjusted the model parameters to catch the observed results. The values of the adjusted parameters for each manual calibration iteration is shown in Table 26. For the third iteration, I activated the crack flow which is a general watershed/basin parameter and found that the flow separation improved substantially with a sharp decrease in the surface runoff and an associated sharp increase in the baseflow. For the next four iterations, I adjusted groundwater, soil and HRU parameters. Observing the model output after each iteration, I found that the model was quite sensitive to the parameters adjusted.

Consideration is required by the soil parameters because the mathematical function (relative, absolute, and replace) should account for the spatial variability of the parameters. For example, the saturated hydraulic conductivity of the soil (SOL_K) varies significantly depending on the type of soil hydrological group. Using a replace function may lead to neglect of this variability. To investigate this impact, iteration 6

employed a replace function. But, this also showed that soil available water capacity (SOL_AWL) and SOL_K were very sensitive parameters.

Table 26. Default and adjusted parameter values for manual calibration iterations.

Parameters		Swat Default	Sim2	Sim3	Sim4	Sim5	Sim6	Sim7	Sim8
bsn	crack flow	NO	NO	YES	YES	YES	YES	YES	YES
	esco	0.95	0.95	0.95	0.95	0.95	0.95	0.95	0.5
	surlag	2	2	2	2	2	2	2	20
gw	rchrq_deep	0.05	0.05	0.05	0.7	0.7	0.7	0.7	0.7
	gwqmn	1000	1000	1000	1000	5	5	5	5
	alpha_bf	0.048	0.048	0.048	0.048	0.01	0.01	0.01	0.012
	gw_delay	31	31	31	31	3	3	3	1
	revapmn	750	750	750	750	500	500	500	500
	gw_revap_juni	0.02	0.02	0.02	0.02	0.02	0.02	0.02	0.065
	gw_revap_oak	0.02	0.02	0.02	0.02	0.02	0.02	0.02	0.06
	gw_revap_rnge	0.02	0.02	0.02	0.02	0.02	0.02	0.02	0.056
gw_revap_barr	0.02	0.02	0.02	0.02	0.02	0.02	0.02	0.05	
hru	ovn_juni	0.1	0.1	0.1	0.1	0.1	0.1	0.25	0.5
	ovn_oak	0.14	0.14	0.14	0.14	0.14	0.14	0.2	0.4
	ovn_rnge	0.14	0.14	0.14	0.14	0.14	0.14	0.15	0.3
	ovn_barr	0.14	0.14	0.14	0.14	0.14	0.14	0.14	0.2
	surlag_juni	2	2	2	2	2	2	20	20
	surlag_oak	2	2	2	2	2	2	15	16
	surlag_rnge	2	2	2	2	2	2	10	12
	surlag_barr	2	2	2	2	2	2	7	8
	canmax_juni	0	0	0	0	0	0	4	3.17
	canmax_oak	0	0	0	0	0	0	3	3
	canmax_rnge	0	0	0	0	0	0	2	1.8
	canmax_barr	0	0	0	0	0	0	0.2	0.2
	esco_juni	0.095	0.095	0.095	0.095	0.095	0.095	0.5	0.53
	esco_oak	0.095	0.095	0.095	0.095	0.095	0.095	0.6	0.6
	esco_rnge	0.095	0.095	0.095	0.095	0.095	0.095	0.7	0.65
esco_barr	0.095	0.095	0.095	0.095	0.095	0.095	0.8	0.7	

Table 26 continued

	Parameters	Swat Default	Sim2	Sim3	Sim4	Sim5	Sim6	Sim7	Sim8
sol	sol_awl_a	0.09	0.09	0.09	0.09	0.09	1	1	0.2
	sol_awl_b	0.18	0.18	0.18	0.18	0.18	1	1	0.28
	sol_awl_c	0.08	0.08	0.08	0.08	0.08	1	1	0.18
	sol_awl_d	0.09	0.09	0.09	0.09	0.09	1	1	0.2
	sol_k_a	100.8	100.8	100.8	100.8	100.8	1	1	100.8
	sol_k_b	32.4	32.4	32.4	32.4	32.4	1	1	32.4
	sol_k_c	32.4	32.4	32.4	32.4	32.4	1	1	32.4
	sol_k_d (374302-03,374308,374310)	32.4	32.4	32.4	32.4	32.4	1	1	32.4
	sol_k_d (374292-93)	9.72	9.72	9.72	9.72	9.72	1	1	9.72
mgt	cn2_juni_a	25	25	25	25	25	25	25	25
	cn2_juni_b	55	55	55	55	55	55	55	38
	cn2_juni_c	70	70	70	70	70	70	70	48
	cn2_juni_d	77	77	77	77	77	77	77	53
	cn2_oak_a	45	45	45	45	45	45	45	45
	cn2_oak_b	66	66	66	66	66	66	66	66
	cn2_oak_c	77	77	77	77	77	77	77	77
	cn2_oak_d	83	83	83	83	83	83	83	83
	cn2_rnge_a	49	49	49	49	49	49	49	49
	cn2_rnge_b	69	69	69	69	69	69	69	69
	cn2_rnge_c	79	79	79	79	79	79	79	79
	cn2_rnge_d	84	84	84	84	84	84	84	84
	cn2_barr_a	77	77	77	77	77	77	77	77
	cn2_barr_b	86	86	86	86	86	86	86	86
	cn2_barr_c	91	91	91	91	91	91	91	91
	cn2_barr_d	94	94	94	94	94	94	94	94

The results of each manual calibration iteration are shown in Table 27. Based on the knowledge I obtained from the first seven iterations, I set up a new SWAT model from scratch to account for the spatial variability of the soil parameters along with the CN2 parameters which play a very significant role in the rainfall/runoff partitioning.

Table 27. The model results of manual calibration iterations. Each iteration has a single simulation.

RESULT OF THE ITERATIONS	ITER1	ITER2	ITER3	ITER4	ITER5	ITER6	ITER7	ITER8	
PERIOD	2008-2015	2012-2015							
SWAT PRCP (mm)	565.80	686.20	686.20	686.20	686.20	686.20	686.20	686.20	
IDW PRCP (mm)	578.06	644.07	644.07	644.07	644.07	644.07	644.07	644.07	
ET (mm)	348.20	398.20	402.40	402.40	402.40	501.60	544.00	536.40	
PET (mm)	1834.9	1771.8	1771.8	1771.8	1771.8	1771.8	1771.8	1771.8	
AVERAGE CN2	72.52	72.52	72.52	72.52	72.52	72.52	72.52	59.49	
SURFACE RUNOFF	116.31	157.61	69.16	69.16	69.16	68.56	51.73	11.82	
PERC.TO SHALL.AQ.	62.87	88.27	192.51	192.51	192.68	101.92	79.72	94.87	
RVP. FRM SHALL. AQ.	35.64	33.32	35.44	35.44	35.44	35.44	35.44	19.81	
LATERAL FLOW	33.70	42.30	21.09	21.09	21.09	13.45	10.17	42.70	
RETURN FLOW	31.78	50.08	144.51	12.38	56.21	29.28	22.23	25.89	
RCHR. TO DEEP AQ.	3.14	4.41	9.63	134.76	134.68	71.34	55.81	66.41	
RATIOS									OBS.
STREAMFLOW/PRECP.	0.32	0.36	0.34	0.15	0.21	0.16	0.12	0.12	0.046-0.047
BS.FLW./T.FLW	0.36	0.37	0.71	0.33	0.53	0.38	0.39	0.85	0.78
SRF.FLW/T.FLW	0.64	0.63	0.29	0.67	0.47	0.62	0.61	0.15	0.22
ET/PRCP	0.62	0.58	0.59	0.59	0.59	0.73	0.79	0.78	

To adjust CN2, SOL_K, and SOL_AWL, I had to know the hydrological groups of soil classes. I adopted the CN2 parameter values for juniper from the study of Qiao et al. (2015) and updated the juniper plant database using on-interface tools. However, I

found that the average CN2 values remained the same despite updating plant CN2 values. Therefore, I had to update the management database of the project. I identified every soil classes with varying hydrological groups and used this information while updating CN2 values for Juniper. Because CN2 values increase by hydrological soil groups from A to D, identifying soil classes for each hydrologic group helped me while updating the model with automatically produced parameters from SWAT-CUP. I found that 16 soil classes out of 24 represented by HRUs and they accounted for 97% of the study area. Because 87% of the study area underlain by the soils in the group D, average CN2 value was high. Table 28 indicates the area of each hydrological soil group within the study area. I mapped the distribution of the soil hydrological groups within the study area and quantified the soil class representability. Figure 37 shows the distribution of hydrological soil groups in the study area.

Table 28. Hydrological soil groups and associated soil classes included or excluded in the HRUs in the watershed.

Hydrological Group	Mukey	Area (%)
A	374290/374313	1.00
B	374304/374305/374307	3.00
C	374288/374291/374298/374309/374318	5.00
D	374292/374293/374308/374310/374316/374317	87.00
Not represented	374297/374301/374302/374303/374306/374312/393914/393915	5.00

HYDROLOGICAL SOIL GROUPS OF THE STUDY AREA

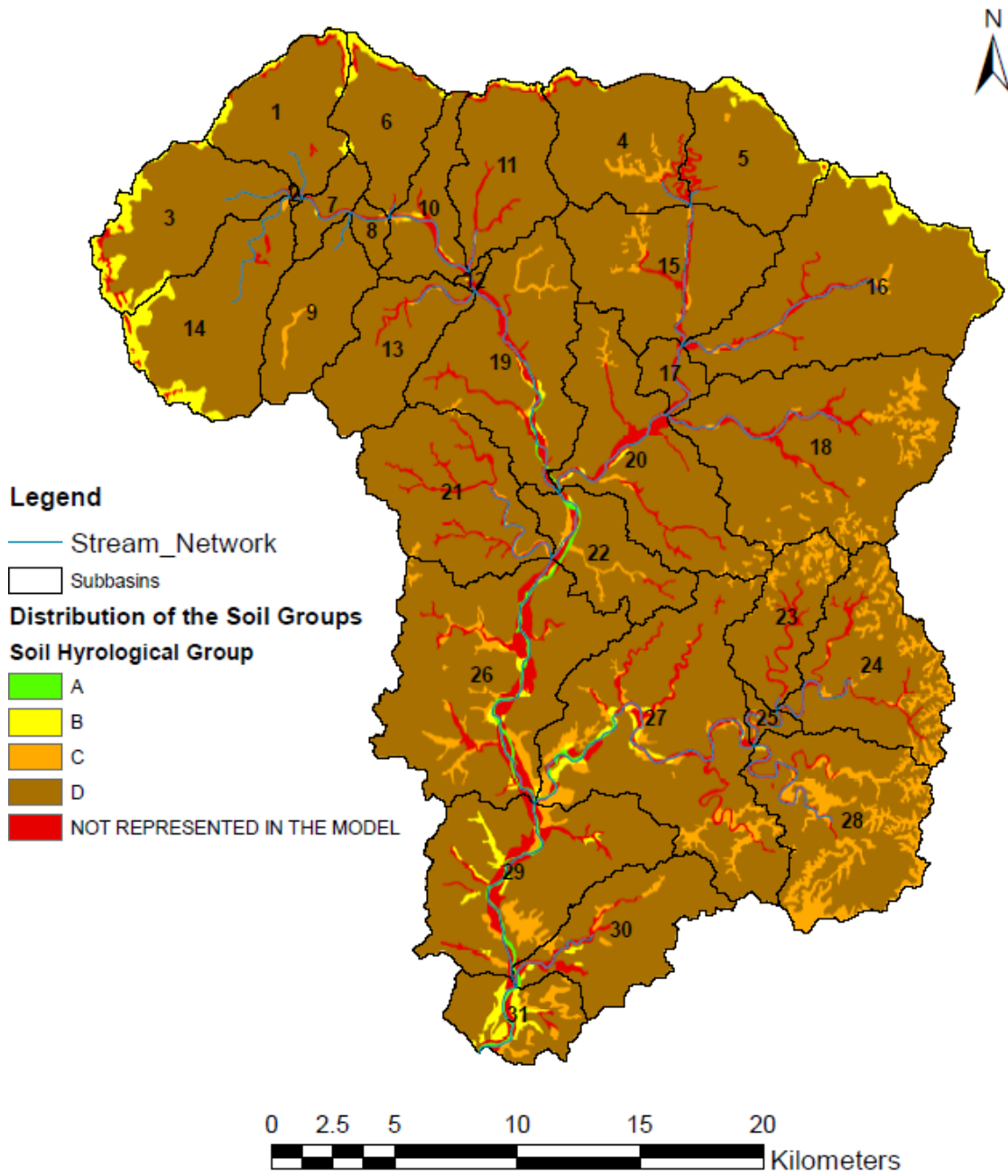


Figure 37. Spatial distribution of the hydrological soil groups included in the HRUs and soil classes remained below the defined threshold.

After identifying each soil class with its corresponding soil hydrological group using the model database which is demonstrated in Figure 38, I adjusted the CN2 parameter for each land use and cover and soil group. I also adjusted soil available water capacity in the final manual calibration iteration considering the variability among soil hydrological groups. I adjusted 15 parameters in total. However, some of these 15 parameters were populated for different land use and cover classes and soil types for the manual calibration. I further populated these 15 parameters when conducting automatic calibration to account for the hydrological variability in subbasins based on the study of Jain et al. (2015). After completing manual calibration, I used the manually calibrated model (model after iteration 8) to set up a SWAT-CUP project for automatic calibration. After running an iteration with 350 simulations and 15 parameters, I performed a global sensitivity analysis.

OID	SUBBASIN	HRU	LANDUSE	SOIL	SLOPE_CD	SNAM	NLAYERS	HYDGRP	SOL_ZMX	ANION_EXCI	SOL_CRK
1	1	1	JUNI	374292	0-3	Eckrant	2 D		2030	0.5	1
2	1	2	JUNI	374292	9-15	Eckrant	2 D		2030	0.5	1
3	1	3	JUNI	374292	3-9	Eckrant	2 D		2030	0.5	1
4	1	4	RNGE	374292	9-15	Eckrant	2 D		2030	0.5	1
5	1	5	RNGE	374292	0-3	Eckrant	2 D		2030	0.5	1
6	1	6	RNGE	374292	3-9	Eckrant	2 D		2030	0.5	1
11	1	11	OAK	374292	15-35	Eckrant	2 D		2030	0.5	1
12	1	12	OAK	374292	9-15	Eckrant	2 D		2030	0.5	1
13	1	13	OAK	374292	0-3	Eckrant	2 D		2030	0.5	1
14	1	14	OAK	374292	3-9	Eckrant	2 D		2030	0.5	1
17	1	17	BARR	374292	15-35	Eckrant	2 D		2030	0.5	1
18	1	18	BARR	374292	0-3	Eckrant	2 D		2030	0.5	1
19	1	19	BARR	374292	9-15	Eckrant	2 D		2030	0.5	1
20	1	20	BARR	374292	3-9	Eckrant	2 D		2030	0.5	1
29	2	7	JUNI	374292	9-15	Eckrant	2 D		2030	0.5	1
30	2	8	JUNI	374292	15-35	Eckrant	2 D		2030	0.5	1
31	2	9	JUNI	374292	3-9	Eckrant	2 D		2030	0.5	1
35	2	13	RNGE	374292	3-9	Eckrant	2 D		2030	0.5	1
36	2	14	RNGE	374292	15-35	Eckrant	2 D		2030	0.5	1
37	2	15	RNGE	374292	9-15	Eckrant	2 D		2030	0.5	1
44	2	22	OAK	374292	9-15	Eckrant	2 D		2030	0.5	1
45	2	23	OAK	374292	3-9	Eckrant	2 D		2030	0.5	1

Figure 38. Identification of soil classes with corresponding soil hydrological group.

I realized that the autocalibration of the preprocessed SWAT-NAIP model yielded satisfactory R square and NSE values based on the model performance criteria established by Moriasi et al. (2007) which is shown in Table 29. However, the percent bias from the calibration of the preprocessed model was very high. The hydrograph of the observed and simulated flow indicated that the model was able to capture the large peak in 2015 but couldn't capture the small peaks for the rest of the period. The trend line of the flow estimated by the model was almost uniform except 2015. This outcome could be the result of using crack flow code to prompt the model to capture the baseflow ratio of the hydrograph separation. Figure 39 shows the response of the model when the crack flow code was activated. To investigate this and decrease percent bias, I set up a new SWAT-NAIP model. I didn't adjust any parameter of the new model manually and called it "Default Model" hereafter. Thus, I had two SWAT-CUP projects for SWAT-NAIP calibrations: one constructed by the preprocessed model and the other with the default model. I tested many parameterization approaches to find the best combination of parameters and their range. These alternatives were parameterizing preprocessed and default model by considering subbasins with flow and subbasins with no flow, parameterizing the default model without considering subbasins with no flow and parameterizing the default model with reduced parameter set.

Table 29. Model Performance Evaluation Criteria. Adapted by Moriasi et al., Van Liew et al. and Fernandez et al. [46, 79, 80].

R Square	Nash Sutcliffe Efficiency	Percent Bias (PBIAS)	Model Performance
$0.75 \leq R^2 \leq 1.00$	$0.75 \leq NSE \leq 1.00$	$Pbias \leq \pm 10$	Very Good
$0.60 \leq R^2 \leq 0.75$	$0.60 \leq NSE \leq 0.75$	$\pm 10 < Pbias \leq \pm 15$	Good
$0.50 \leq R^2 \leq 0.60$	$0.36 \leq NSE \leq 0.60$	$\pm 15 < Pbias \leq \pm 25$	Satisfactory
$0.25 \leq R^2 \leq 0.50$	$0.00 \leq NSE \leq 0.36$	$\pm 25 < Pbias \leq \pm 50$	Poor
$R^2 \leq 0.25$	$NSE \leq 0.00$	$\pm 50 \leq Pbias$	Inadequate

I realized that the initial rainfall/runoff partitioning was better represented by the NLCD model with the default parameters. Because NLCD is a community-level LULC classification dataset, the area of the barren class was much lower compared to the higher resolution thematic map. The shrub category has the largest area (about 60%) in the NLCD, which was commonly associated with the Range Brush (RNGB) in the modeling studies and has default CN2 values like those of an evergreen forest. Upon quantifying the area of each 3rd level classes mapped within the brush category of the NLCD dataset, I found that 30.72% and 12.28% of the brush area are composed of juniper and barren, respectively. This outcome explains the lower average CN2 values which led to more baseflow and less surface runoff in the NLCD SWAT model. Later, I also quantified the 3rd level class area inside the 2nd level NLCD deciduous forest, evergreen forest, and range grass land use cover categories.

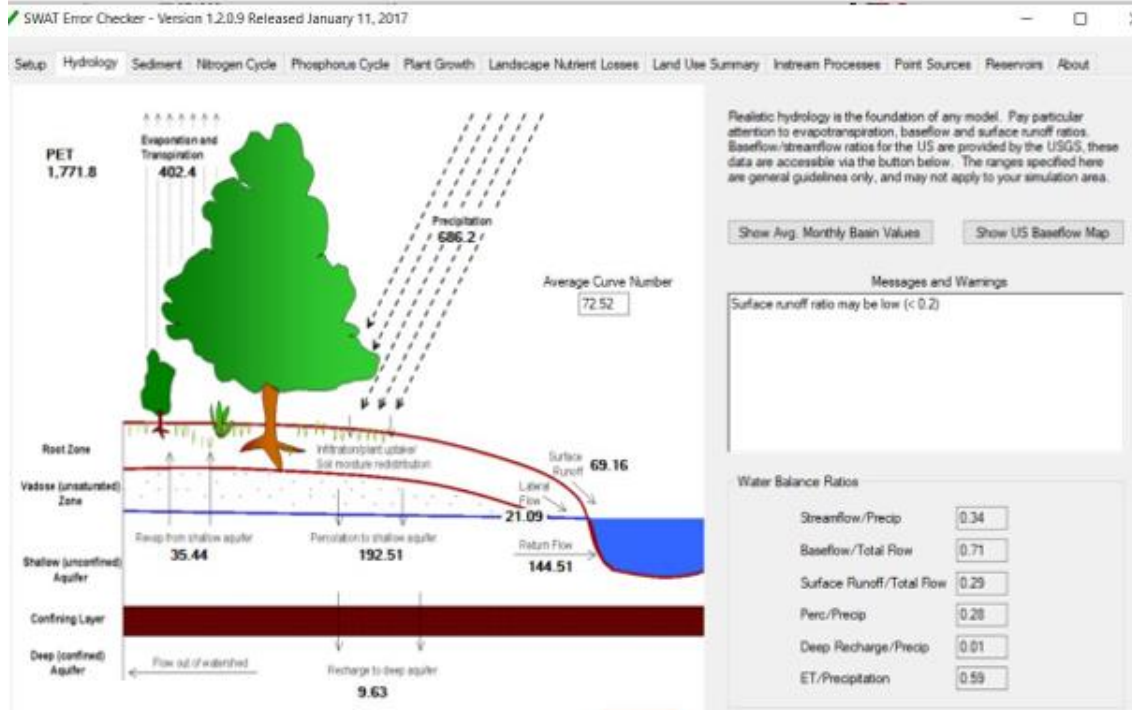
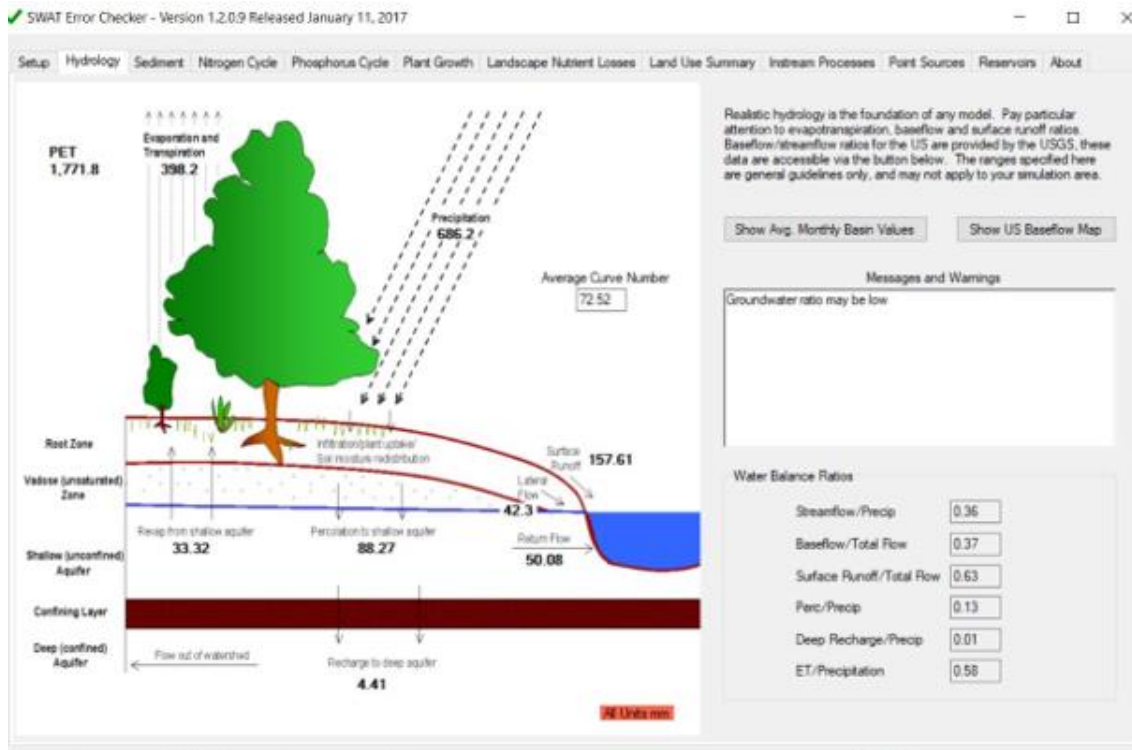


Figure 39. Screenshots indicating how the rainfall partitioning has improved for the watershed following the activation of crack flow (below).

Because Jain et al. (2015) reported calibrated parameters for the whole Nueces River Headwaters watershed, I didn't calibrate NLCD-SWAT model. To investigate if the calibrated parameters can validate the model for the same watershed in a different period, I constructed the NLCD-SWAT model with the similar input data sources used by Jain et al. Although the validation period for the SWAT-NAIP and SWAT-LANDSAT models was from 2016 to 2017, I preferred to validate the SWAT-NLCD model for the 2012-2015 period to have more years and same period to compare the results to the SWAT-NAIP and SWAT-LANDSAT calibrations. I included the same parameters for SWAT-NLCD validation based on the calibrated parameters reported by Jain et al., and gave very small range to prompt the SWAT-CUP account for the parameter uncertainty. Later, I ran an iteration with 150 simulations in SWAT-CUP.

All SWAT-LANDSAT calibration and validation models were default. ASTER DEM data with the 28.97-meter resolution was used to delineate watersheds. Total number of subbasins were 35 in the SWAT-LANDSAT models. LULC class matching was the same for all classes like the SWAT-NAIP models excluding the oak savanna category. Because there is no oak savanna category in the SWAT model and those areas usually located in the range grass (RNGE) and range brush (RNGB) categories of the NLCD data, I determined to match oak savanna area with RNGB category. Because I included most of the parameters related to land use cover like groundwater revaporation coefficient, canopy maximum storage, soil evaporation compensation factor, and curve number (Gw_revap, Canmx, Esco, Cn2) in the parameterization of the models, the

default RNGB parameters could be adjusted to capture the hydrological and biological features of the oak savanna land cover class.

Model validation was performed to investigate the reliability of the calibrated parameter set for the study area. I selected 2016-2017 period for model validation. Because the warm-up periods aren't simulated by the model but having at least one year of the warm-up period is suggested, I specified the 2012-2015 period as the warm-up period for the default SWAT-NAIP and LANDSAT validation models. According to the user's manual of SWAT-CUP, to validate the model, calibrated parameter ranges should be used without any additional change while running an iteration having the same number of simulations used for calibration. This could be less challenging if one LULC and SWAT model used in this study. However, for validating the calibrated models I had to set up validation models for both Landsat and NAIP images.

III.16 Model Simulation Scenario

A scenario of brush control on flat, gentle and moderate slopes was created to simulate the effect of brush management on the water yield of the watershed after the calibration and validation of the model. The scenario assumed the implementation of brush control on slopes less than 15% in the entire study area. The data covering the period of 2009-2011 was used for model verification, and the verified model was used to simulate the impact of brush control. I selected this period because it was used as the model's warm-up period for calibration and wasn't simulated. Furthermore, I had the opportunity to verify the model after calibration and validation using the observed streamflow data.

I identified the juniper cover subjected to brush control to produce the hypothetical LULC data. To achieve this, I created a slope mask by reclassing slopes lower than 15% into one class and slopes greater than 15% into another. I specified the raster values as 10 and 0 for suitable (less than 15 %) and unsuitable (greater than 15%) slopes for brush control, respectively. Then I extracted juniper cover on suitable slopes by summing 2008 land cover raster data with the slope mask raster. I calculated the statistics of the product and reported in Table 30. So, junipers on slopes lower than 15% made up about 18% (160 km²) and 40.53% of the study area and total juniper cover, respectively.

Table 30. Land use and land cover in the study watershed before and after hypothetical brush management.

2008 LULC STATISTICS BEFORE HYPOTHETICAL BRUSH MANAGEMENT			
Value	Class Name	Area (%)	Area (km2)
1	Juniper	25.95	235.42
2	Herbaceous	27.79	252.05
3	Oak	13.52	122.66
4	Barren	14.8	134.27
6	Water	0.16	1.49
7	Urban/Built-up	0.08	0.72
11	Juniper treatment planned	17.69	160.47
2008 LULC STATISTICS AFTER HYPOTHETICAL BRUSH MANAGEMENT			
Value	Model LULC Code	Area (%)	Area (km2)
1	JUNI	25.95	235.42
2	RNGE	45.48	412.52
3	OAK	13.52	122.66
4	BARR	14.8	134.27
6	WATR	0.16	1.49
7	URML	0.08	0.72
LULC CODE DEFINITION			
JUNI	Juniper	BARR	Barren
RNGE	Range Grass	WATR	Water
OAK	Oak	URML	Urban Medium Low Density

I simulated the impact of brush control on the hydrology of the watershed under the brush management scenario. To do this, I first ran the model using the original 2008 LULC data to establish a benchmark for comparison. The distribution of the junipers on suitable slopes in the study area is shown in Figure 40. I converted all juniper cover on the suitable slopes into herbaceous cover as specified in the brush control/management scenario. Figure 41 shows the hypothetical LULC data used for the scenario simulation. I used this hypothetical LULC data to run the SWAT model. Finally, I compared the simulated ET, surface runoff, baseflow and water yield under the brush management scenario with the benchmark results to assess the impact of brush control.

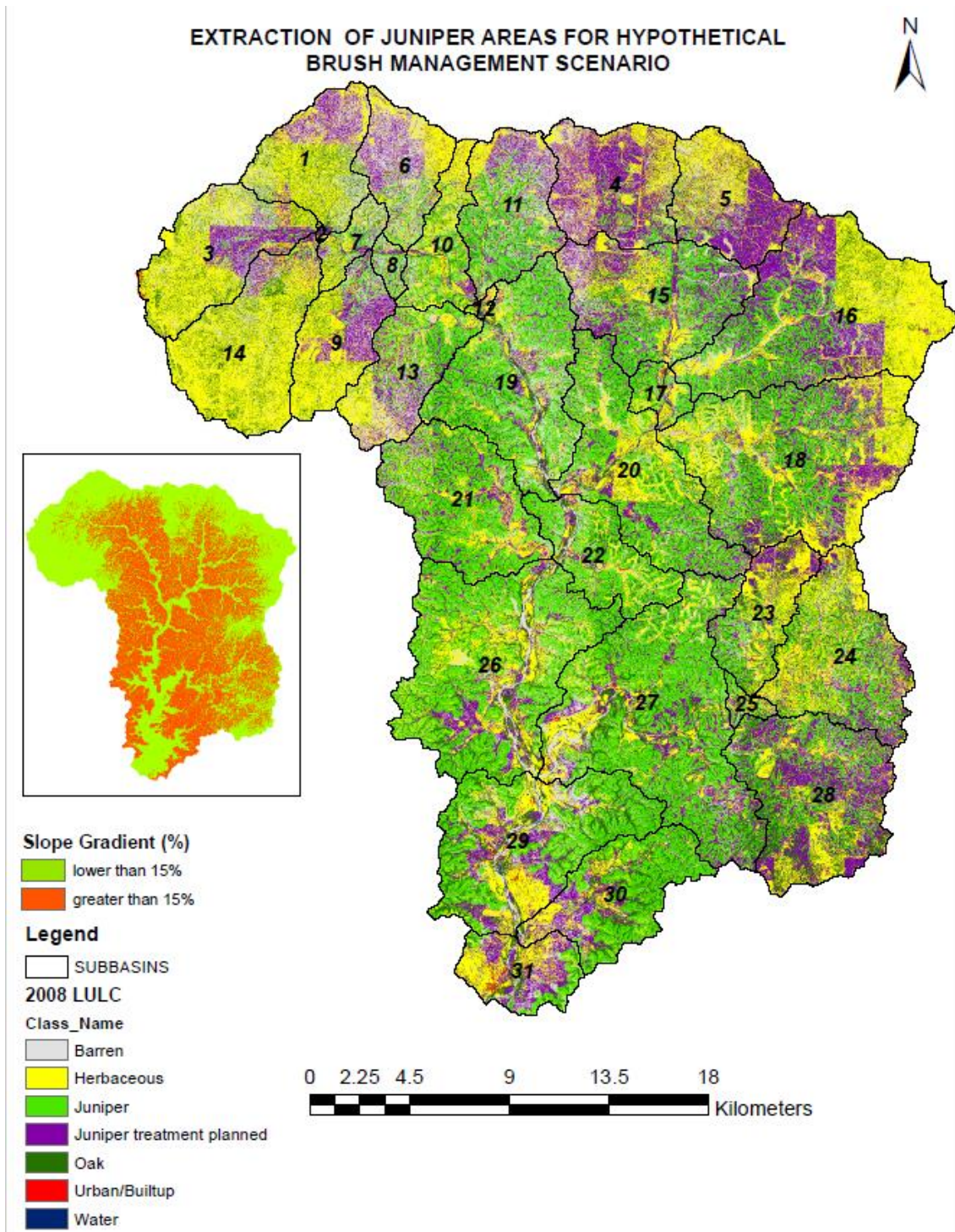


Figure 40. Suitable area for the brush control application.

DISTRIBUTION OF THE LAND COVER CLASSES AFTER
HYPOTHETICAL BRUSH MANAGEMENT

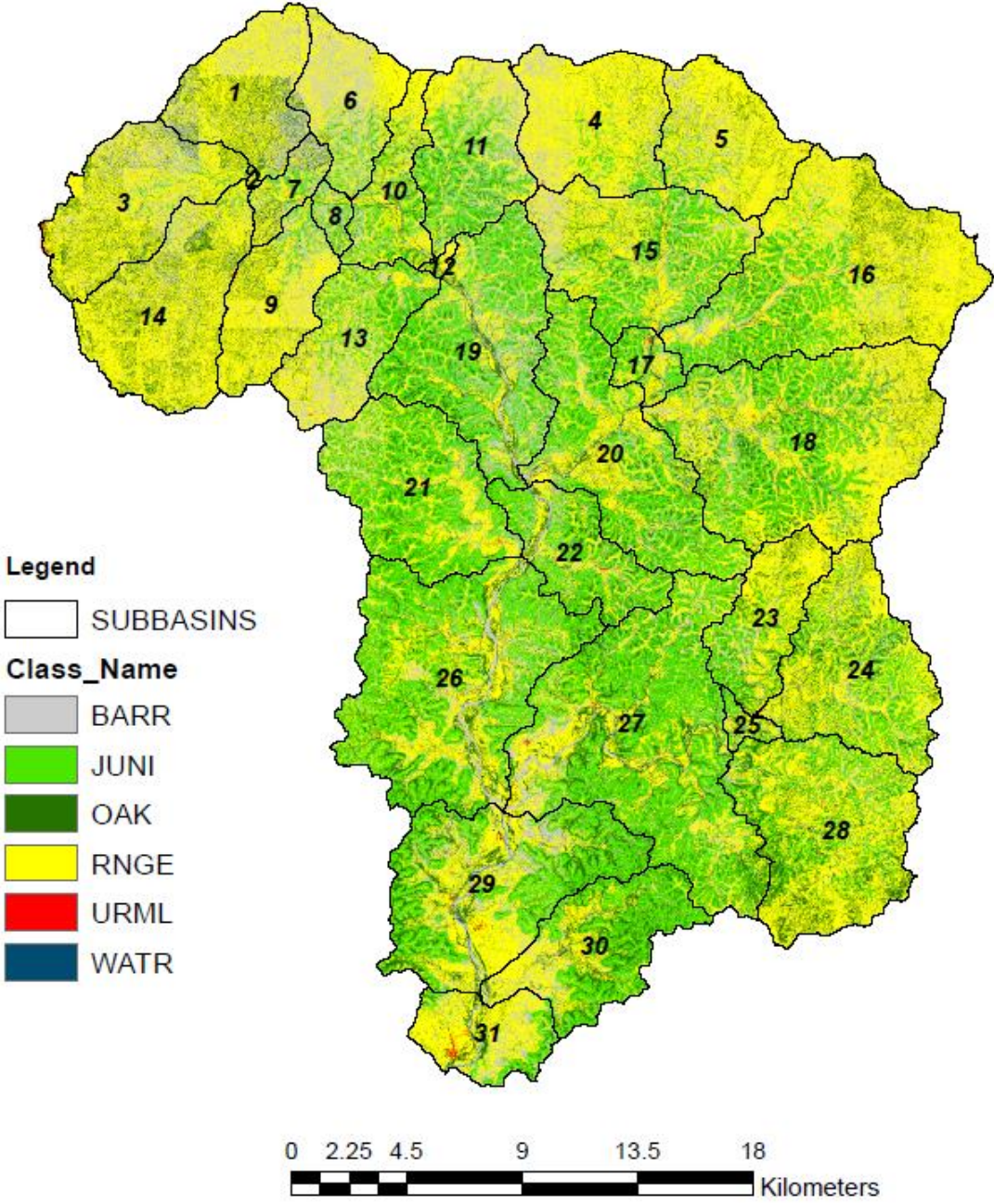


Figure 41. Hypothetical LULC data for the scenario simulation.

CHAPTER IV

RESULTS AND DISCUSSION

IV.1 Interpolated Annual Rainfall, Measured Water Yield and Baseflow Ratio

I found that annual rainfall didn't change significantly with elevation in the study area. Figure 42 demonstrates the distribution and magnitude of the storm events greater than 2.5 mm measured by stations which have different elevations. Green lines in Figure 42 indicates the average of the rainfall. ANOVA results for the precipitation and elevation is shown in Table 31.

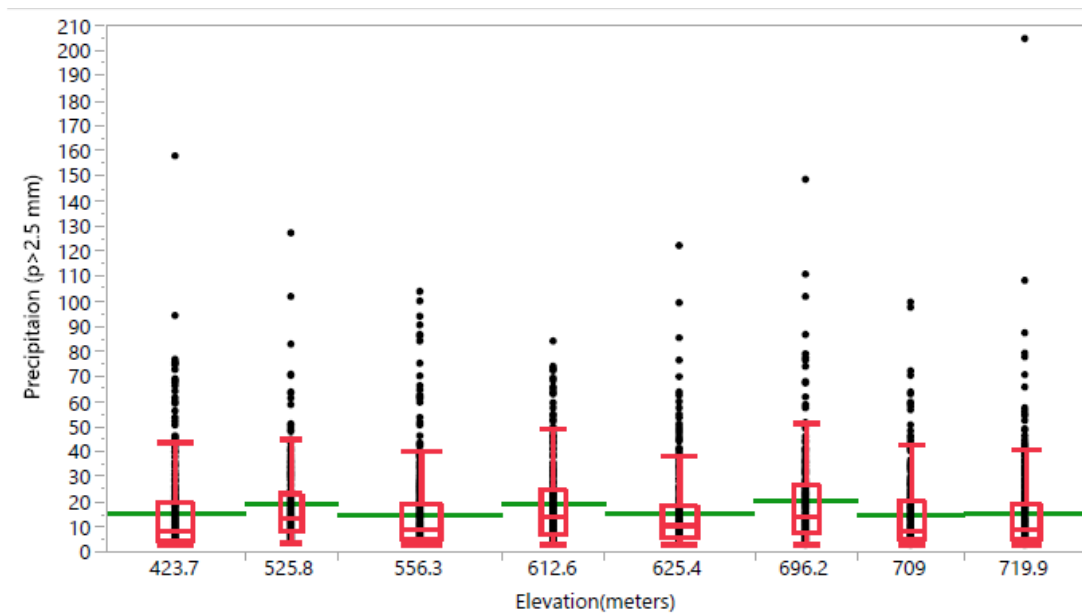


Figure 42. Normal outlier box plots of precipitation over elevation.

Table 31. The statistical relationship between precipitation and elevation.

Summary of Fit			
Rsquare		0.015	
Adj Rsquare		0.013	
Root Mean Square Error		16.872	
Mean of Response		16.43	
Observations		2688	
Means for Oneway Anova			
Precipitation Events			
Elevation Category	(>2.5 mm)	Mean	Std Error
423.7	379	15.35	0.87
525.8	257	19.01	1.05
556.3	451	14.80	0.79
612.6	281	18.93	1.01
625.4	411	15.06	0.83
696.2	282	20.56	1.00
709	295	14.72	0.98
719.9	332	15.45	0.93

The measured water yield is shown in Table 32 demonstrated that annual water yield was very low. The ratio of annual water yield to interpolated annual precipitation remained below 8% for the entire study period. This outcome was comparable to the results from Wilcox and Huang [12]. Simple annual rainfall averages were better correlated with the results from the IDW method ($R^2 = 0.99$ with 95% confidence) than with the PRISM rainfall data ($R^2 = 0.91$ with 95% confidence). Table 33 shows the high correlation between IDW precipitation and PRISM precipitation. However, there is a possibility that the annual rainfall was slightly overestimated by PRISM.

Table 32. Measured annual water yield by years and its ratio to interpolated annual rainfall.

Year	Annual Rainfall (mm)	Annual Mean Flow (f ³ /s)	Annual Flow Volume (m ³)	Drainage Area (m ²)	Annual Flow Per Unit Area (mm)	Water Yield (%)
2009	475.29	26.05	23,258,592.84	907,130,836.2	25.64	5.40
2010	669.75	38.04	33,971,211.15	907,130,836.2	37.45	5.59
2011	325.09	16.94	15,128,909.59	907,130,836.2	16.68	5.13
2012	557.18	20.21	18,046,043.16	907,130,836.2	19.90	3.57
2013	606.21	27.49	24,550,060.37	907,130,836.2	27.07	4.46
2014	484.90	16.43	14,674,967.88	907,130,836.2	16.18	3.34
2015	928.00	66.39	59,287,763.25	907,130,836.2	65.37	7.04
2016	805.71	61.68	55,083,221.24	907,130,836.2	60.73	7.54
2017	625.40	41.42	36,985,086.40	907,130,836.2	40.78	6.52

Table 33. The statistical relationship between IDW and PRISM annual precipitation.

<i>Regression Statistics</i>	
Multiple R	0.966
R Square	0.931
Adjusted R Square	0.922
Standard Error	60.84
Observations	9

<i>ANOVA</i>					
	<i>df</i>	<i>SS</i>	<i>MS</i>	<i>F</i>	<i>Significance F</i>
Regression	1	354856.3	354856.3	95.87635	0.000024576
Residual	7	25908.31	3701.187		
Total	8	380764.6			

Hydrograph separation results displayed in Table 34 indicated that about 80% of the stream flow is the contribution of the baseflow. The hydrograph of the average stream flow and precipitation shown by Figure 43 indicated that not every storm event is capable of producing peak flows in the watershed outlet.

Table 34. Results of the hydrograph separation analysis.

Year	Average of Flow	Average of Base Flow	Average of Direct Runoff	Baseflow Ratio	Surface Runoff Ratio
2009	26.06	20.09	5.97	77.08	22.92
2010	37.71	30.13	7.58	79.91	20.09
2011	16.89	13.55	3.34	80.25	19.75
2012	20.18	16.31	3.87	80.81	19.19
2013	27.47	21.38	6.08	77.85	22.15
2014	16.41	13.31	3.10	81.08	18.92
2015	66.77	48.31	18.46	72.35	27.65
2016	61.71	48.96	12.74	79.35	20.65
2017	41.21	33.32	7.89	80.85	19.15
Study Period Average	34.93	27.26	7.67	78.84	21.16

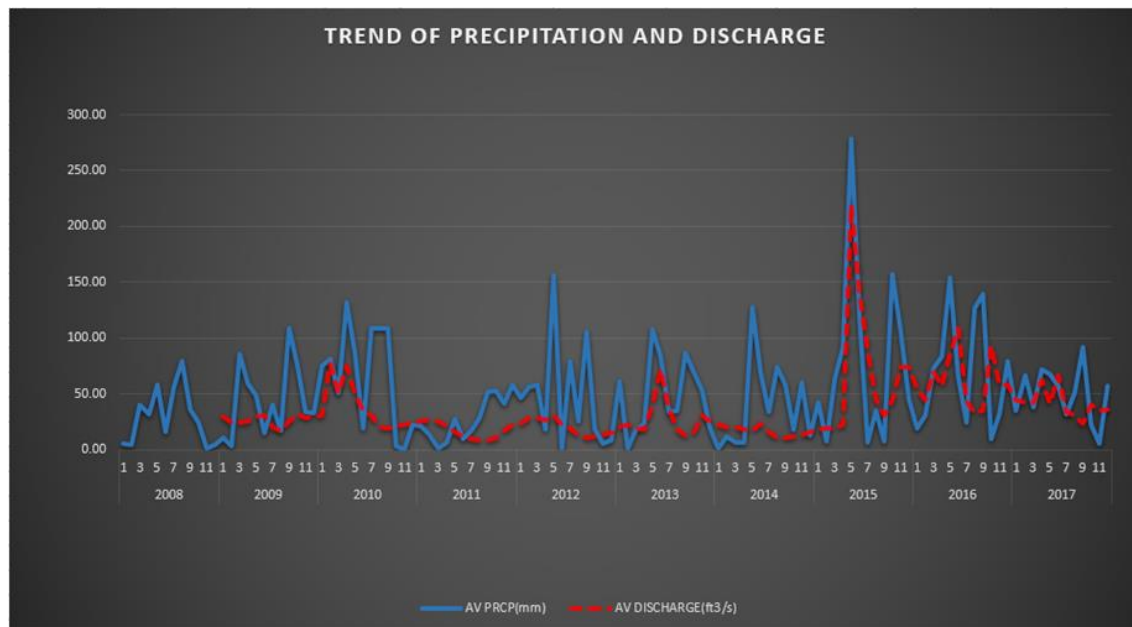


Figure 43. Monthly rainfall and streamflow for the period of 2009-2017. Note that the units are different. Rainfall is expressed in mm, and streamflow is expressed in cubic feet per second. This graph was prepared to indicate peak flows as a response to storm events.

For example, there wasn't significant peak flow observed in 2012 although there were a considerable number of storm events. This situation was addressed previously by Dammeyer et al. who reported that antecedent rainfall makes a significant impact on runoff generation [22]. The annual rainfall distribution of the study area is shown for 2009-2017 period in Figure 44.

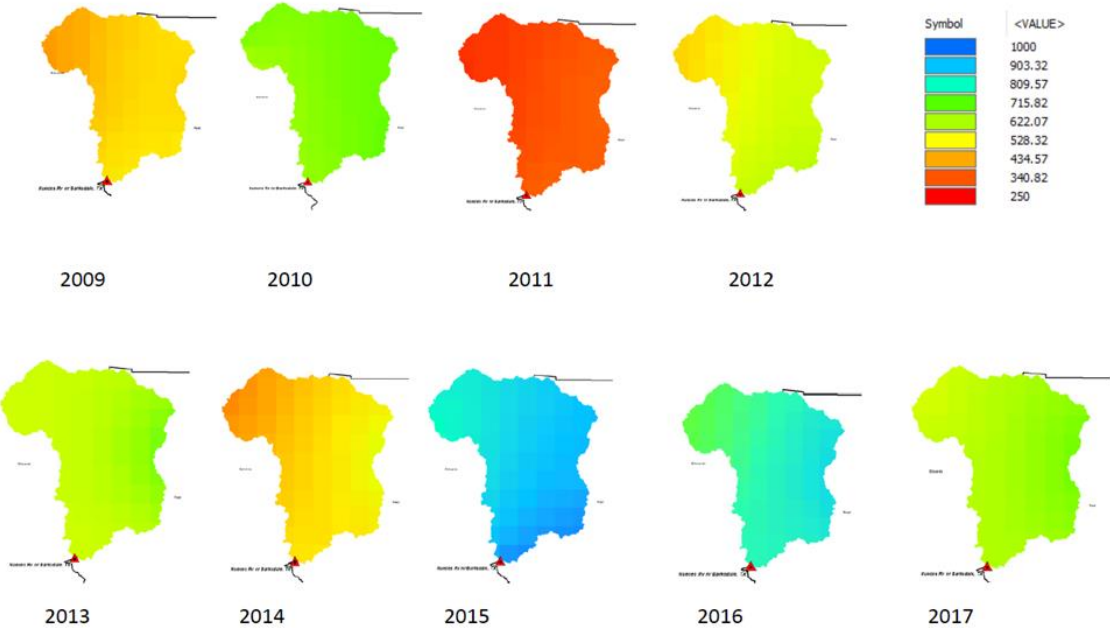


Figure 44. Annual average precipitation distribution throughout the study area calculated by the IDW method for the period 2009-2017. The precipitation values are expressed in mm.

IV.2 Land Use and Cover Maps and Change Detection

IV.2.1 Accuracy of the Shadow Identification Approach and Final Thematic Maps

Classification of the multiple-year aerial and satellite images was a very arduous task. Moreover, the problems caused by shadows and pixel confusion required extra labor. However, the accuracy in the shadow identification method was quite satisfactory and enhanced the utility of the final thematic maps. According to the accuracy assessment results of the shadow detection method which is shown in Table 35, the probability of correctly identifying a shadow area ranged from 89.3% to 98.6%. The count of shadow pixels in the final classifications became so minimal that they are unlikely to make a negative impact for the further hydrological analysis of the study area. More than 99% of the shadow area was identified for each year. Table 36 reports the area of identified shadow cover and the remaining shadow area.

Table 35. Accuracy assessment of the shadow identification method.

Cover Type Inside the Shadow	Ground Truth Pixel Count					
	2008	2010	2012	2014	2015	2016
Juniper	71					
Oak	70					
Trees		70	70	70	70	70
Herbaceous	70	70	70	71	70	70
Shadow Total	211	140	140	141	140	140
	Count of Correctly Identified Shadow Pixels					
Classes Converted from Shadow	2008 ML	2010 ML	2012 ML	2014 ML	2015 ML	2016 ML
Juniper	61					
Oak	67					
Trees		69	70	65	66	70
Herbaceous	64	69	55	64	60	64
Total	192	138	125	129	126	134
Percent Accuracy	91.00	98.57	89.29	91.49	90.00	95.71

Table 36. Areas of classes detected within the shadowed areas and remaining unidentified shadow areas.

Classes Edited for Shadow	Area of the LULC (Percent)					
	2008 ML	2010 ML	2012 ML	2014 ML	2015 ML	2016 ML
Herbaceous Before Editing	28.11	31.42	24.77	29.26	23.35	23.66
Herbaceous After Editing	29.03	32.48	25.45	31.29	24.84	24.76
Herbaceous Inside Shadow	0.92	1.06	0.68	2.02	1.49	1.10
Tree After Editing		55.93	48.75	48.60	61.08	54.09
Tree Before Editing		52.30	44.63	40.66	53.16	48.61
Tree Inside Shadow		3.62	4.12	7.94	7.92	5.48
Juniper Before Editing	36.66					
Juniper After Editing	39.37					
Juniper Inside Shadow	2.71					
Oak Before Editing	13.61					
Oak After Editing	15.53					
Oak Inside Shadow	1.92					
Remaining Shadow	0.01	0.01	0.03	0.03	0.02	0.02
Total Shadow Cover	5.55	4.69	4.83	9.99	9.44	6.61
Total Shadow Area Identified	5.55	4.68	4.80	9.96	9.41	6.58
Percentage of Shadow Identified	99.85	99.83	99.29	99.73	99.74	99.63

Accuracy assessment of the finalized thematic maps yielded very satisfactory results which is shown in Table 37, especially for 2008, 2014 and 2016 image classifications. The accuracy of 2014 image improved by 3% after converting the shadow area into associated land use and cover. All classifications met the minimum accuracy threshold (85% overall accuracy). I also reported other accuracy metrics like Kappa Coefficient, user and producer accuracies.

Table 37. Final accuracies of the NAIP ML image classifications.

	2008	2010	2012	2014	2015	2016
Overall and Kappa	ML	ML	ML	ML	ML	ML
Overall	93.74%	91.35%	93.02%	93.81%	92.89%	97.29%
Kappa	0.92	0.87	0.89	0.91	0.89	0.96

Class	User Accuracy					
	(Percent)					
	2008	2010	2012	2014	2015	2016
Herbaceous	96.94	83.15	93.33	89.06	91.53	100.00
Trees		97.62	94.30	96.92	94.40	98.40
Unvegetated	75.27	84.34	79.49	88.75	82.50	82.35
Urban/Built-up	100.00	100.00	95.83	100.00	100.00	100.00
Water	98.18	100.00	100.00	100.00	100.00	100.00
Juniper	96.65					
Oak	92.57					

Class	Producer Accuracy					
	(Percent)					
	2008	2010	2012	2014	2015	2016
Herbaceous	92.50	94.58	87.50	94.61	90.00	97.08
Trees		88.65	98.38	93.51	95.68	99.73
Unvegetated	100.00	100.00	88.57	100.00	94.29	100.00
Urban/Builtup	96.30	96.00	92.00	96.00	92.00	96.00
Water	77.14	84.29	88.41	85.51	86.96	82.86
Juniper	96.30					
Oak	95.29					

The accuracy assessment results demonstrated that incorporating data from different sensors having distinctive temporal and spatial resolutions can be a very effective strategy to produce useful thematic maps by compensating for the tradeoffs inherent to the data from a single source. Table 38 shows the initial and finalized accuracies of the LULC maps derived from the ML classification of NAIP images. High-resolution imagery provides tremendous details for the analysis of land use and

cover. However, using higher-resolution images for large area mapping is quite labor-intensive.

Table 38. Accuracy of the higher-resolution maps before and after shadow editing.

Image Year	Initial Accuracy Stat		Final Accuracy Stat	
	Overall (%)	Kappa	Overall (%)	Kappa
2008	0.94	0.93	0.94	0.92
2010	0.90	0.87	0.91	0.87
2012	0.93	0.91	0.93	0.89
2014	0.91	0.88	0.94	0.91
2015	0.93	0.91	0.93	0.89
2016	0.97	0.96	0.97	0.96

The percent area of each LULC class is shown in Table 39. I want to note that tree cover was the highest for 2015. This was because the 2015 aerial image was captured at the end of 2015 and early 2016. The rainfall in 2015 was very excessive compared to the long-term average annual precipitation. There was less space observed between tree crowns in 2015 NAIP image which was demonstrated by Figure 45. This was a result of favorable moisture conditions which led to exponential leaf production especially in the juniper-dominated areas. Juniper trees are hydrologically and biologically active all year long and their response to suitable moisture conditions is very rapid. Besides, I found that brush regrowth was occurring from 2008 to 2014 gradually, accelerated in 2015 due to optimal climatic conditions. Although the year 2016 was also a wet year, tree cover dropped compared to 2015. This indicates that a different period of image capture can have a very different canopy morphology of brush species.

Table 39. Percentage of the area of each LULC class across the years.

Number of Classes	Class Name	Final Area of LULC Classes(Percent)					
		2008	2010	2012	2014	2015	2016
1	Herbaceous	27.81	29.41	22.08	28.69	23.82	23.22
2	Shadow	0.01	0.00	0.03	0.02	0.02	0.02
3	Trees		60.77	52.45	51.74	63.58	56.98
4	Unvegetated	14.81	9.59	25.22	19.32	12.39	19.49
5	Urban/Built-up	0.08	0.06	0.11	0.11	0.08	0.09
6	Water	0.16	0.16	0.11	0.11	0.11	0.20
7	Juniper	43.60					
	Oak	13.53					
	Total (%)	100	100	100	100	100	100

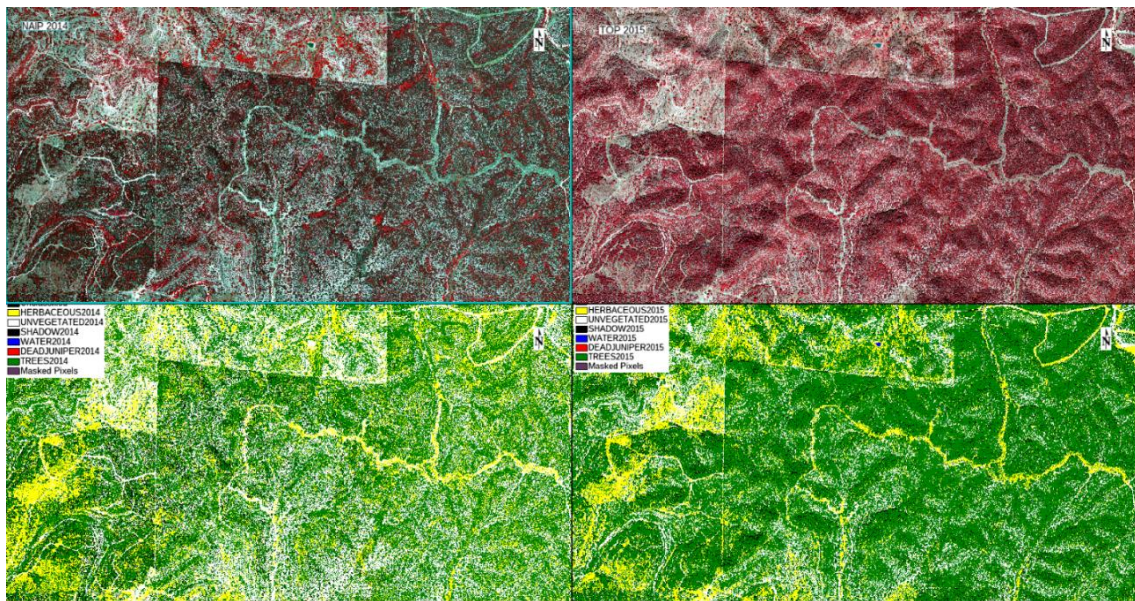


Figure 45. Figure 44: Decreases in intercanopy space from 2014 (left column) to 2015 (right column).

Figure 46 demonstrates the presence of more unvegetated area in 2016 when the image captured compared to 2015. The 2016 image was captured at late summer when there was less rainfall, which may explain the lower canopy cover. I would like to point out that higher-resolution details in aerial image classifications can indicate seasonal biogeomorphological changes very effectively. It would be more difficult to see this dynamism with community-level classifications because most of the change occurs in smaller areas (less than 900 m²) [52]. Figure 47 shows the thematic maps derived from the classification of aerial images for a part of the study area.

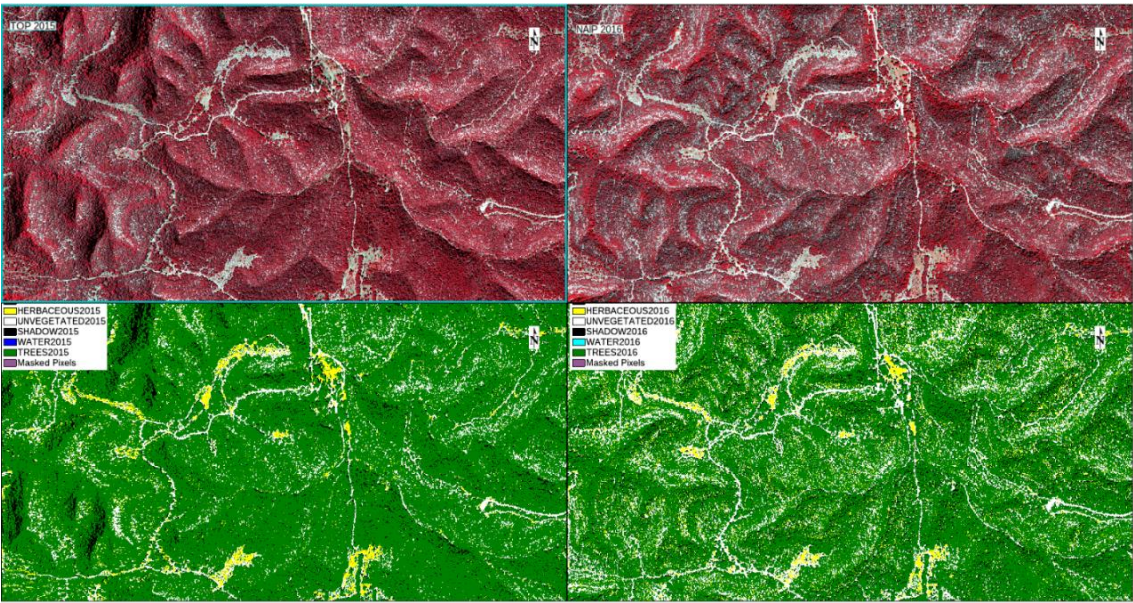


Figure 46. Differences in canopy closure between 2015 (left column) and 2016 (right column).

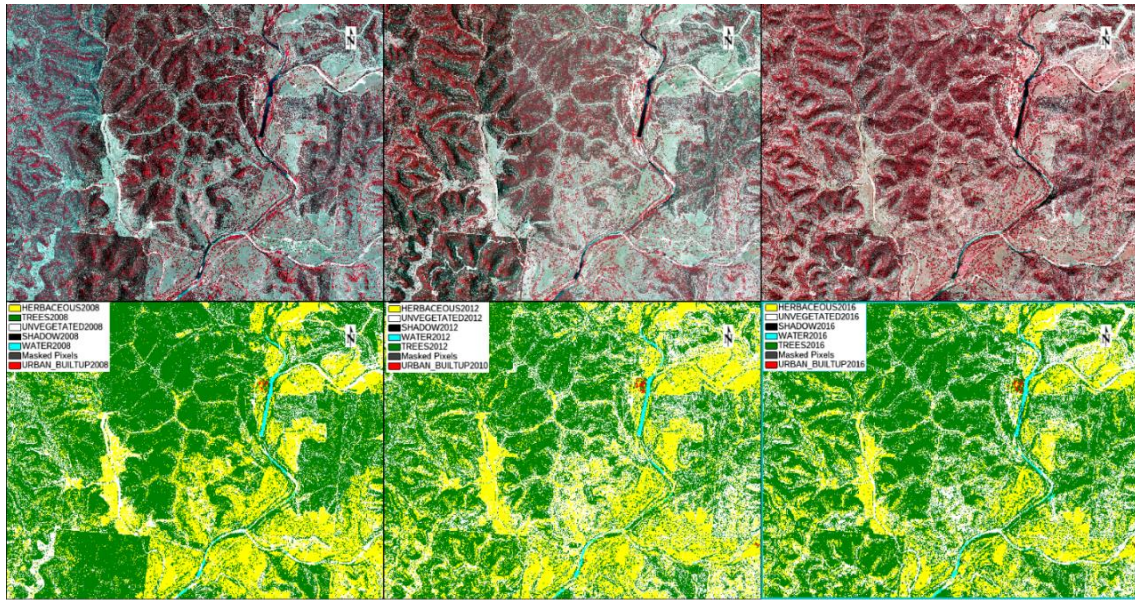


Figure 47. A portion of the study area shown by classified (below) and NIR false color composite (above) aerial images. The year of the images from left to right is 2008, 2012 and 2016. Note that the farthest distance in this portion of the area is longer than 10 kilometers.

IV.2.2 Thematic Change Detection

Below, as shown in Table 40 and 41, I reported the changes in area (km²) and percentages between tree cover and other two land use and cover classes (herbaceous and unvegetated) given the focus of this study on brush management. Because the statistics from change detection were important to update the SWAT model, I quantified the change from 2008 to another year instead of for any consecutive years. Thus, I could see the increase or decrease in the tree cover from 2008 to any year having a thematic LULC map.

Table 40. The results of change detection analysis reported in percentages for aggregated and original thematic change.

Period Type Class Summary	2008 to 2010 (%)		2008 to 2012 (%)		2008 to 2014(%)	
	Bf. Agg.	After	Bf. Agg.	After	Bf. Agg.	After
No Change	85.72	98.16	83.41	95.42	80.36	94.27
Herbaceous' To 'Trees'	5.62	0.84	4.02	0.47	4.33	0.70
Trees' To 'Herbaceous'	3.35	0.50	5.21	2.79	8.52	3.56
Trees' To 'Unvegetated'	1.98	0.08	5.42	1.21	4.00	1.03
Unvegetated' To 'Trees'	3.33	0.41	1.93	0.11	2.80	0.43
Sum	100	100	100	100	100	100
Tree Difference	3.62	0.67	-4.68	-3.43	-5.39	-3.46
Period Type Class Summary	2008 to 2015(%)		2008 to 2016(%)			
	Bf. Agg.	After	Bf. Agg.	After		
No Change	80.58	95.28	82.30	95.73		
Herbaceous' To 'Trees'	9.01	1.96	6.24	0.89		
Trees' To 'Herbaceous'	4.14	1.83	4.60	2.22		
Trees' To 'Unvegetated'	2.36	0.45	4.33	1.07		
Unvegetated' To 'Trees'	3.91	0.47	2.54	0.09		
Sum	100	100	100	100		
Tree Difference	6.41	0.14	-0.16	-2.30		

Table 41. Results of thematic change detection analysis reported in area.

Period Type Class Summary	2008 to 2010		2008 to 2012		2008 to 2014	
	Bf. Agg.	After	Bf. Agg.	After	Bf. Agg.	After
	Area (km ²)		Area (km ²)		Area (km ²)	
No Change	777.58	890.45	756.66	865.55	729.01	855.12
Herbaceous' To 'Trees'	50.98	7.64	36.49	4.26	39.25	6.37
Trees' To 'Herbaceous'	30.38	4.54	47.26	25.31	77.25	32.33
Trees' To 'Unvegetated'	17.95	0.73	49.18	11.02	36.24	9.37
Unvegetated' To 'Trees'	30.23	3.76	17.53	0.99	25.37	3.94
Sum	907.13	907.13	907.13	907.13	907.13	907.13
Tree Difference	32.88	6.12	-42.42	-31.07	-48.87	-31.38

Period Type Class Summary	2008 to 2015		2008 to 2016	
	Bf. Agg.	After	Bf. Agg.	After
	Area (km ²)		Area (km ²)	
No Change	730.92	864.35	746.54	868.38
Herbaceous' To 'Trees'	81.70	17.77	56.59	8.10
Trees' To 'Herbaceous'	37.60	16.64	41.73	20.12
Trees' To 'Unvegetated'	21.42	4.10	39.27	9.69
Unvegetated' To 'Trees'	35.49	4.26	23.00	0.85
Sum	907.13	907.13	907.13	907.13
Tree Difference	58.17	1.29	-1.41	-20.86

I compared the statistics of original thematic change and aggregated thematic change with tables and figures. Figure 48 shows a large brush control area for different years and the thematic change detection maps in the original format.

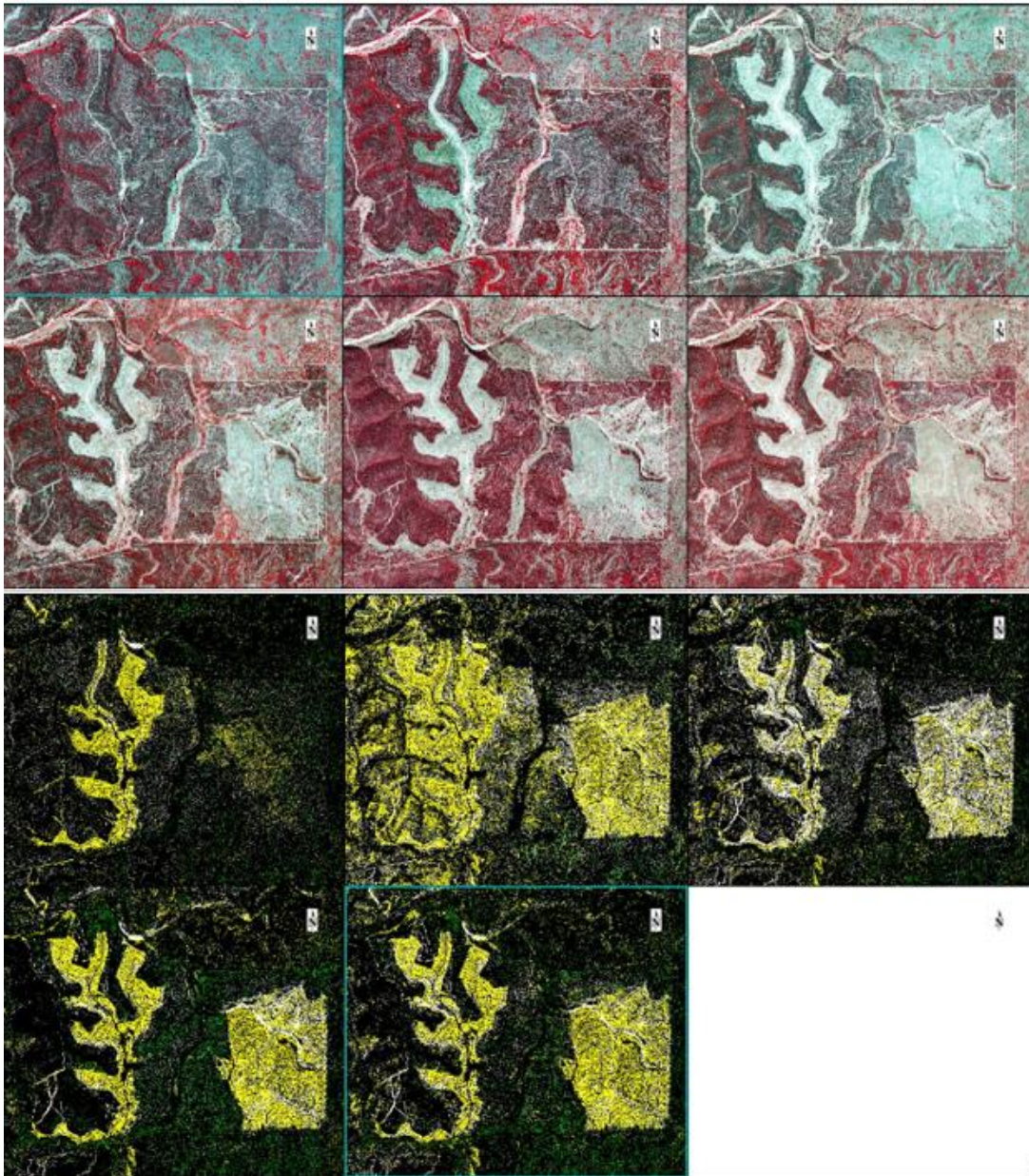


Figure 48. Land cover change at a large brush management site in the study area. The NIR false-color images are 2008, 2010, 2012 (above) and 2014, 2015, 2016 (below) from left to right. Below are the original thematic change maps showing land cover change. On top from left to right, the thematic change maps are 2008-2010, 2008-2012, 2008-2014. Below from left to right 2008-2015 and 2008-2016 thematic change maps are shown. Dark color indicates no change, yellow indicates a change from trees to herbaceous, white indicates a change from trees to unvegetated, and green indicates a change from herbaceous or unvegetated to trees.

Aggregated thematic change maps are shown in Figure 49 for the same location. Aggregation of change detection classes yielded very distinctive results. The potential of representing changes resulting from brush control activities and brush encroachment increased by the aggregation because smaller changes due to forage production and loss were eliminated.

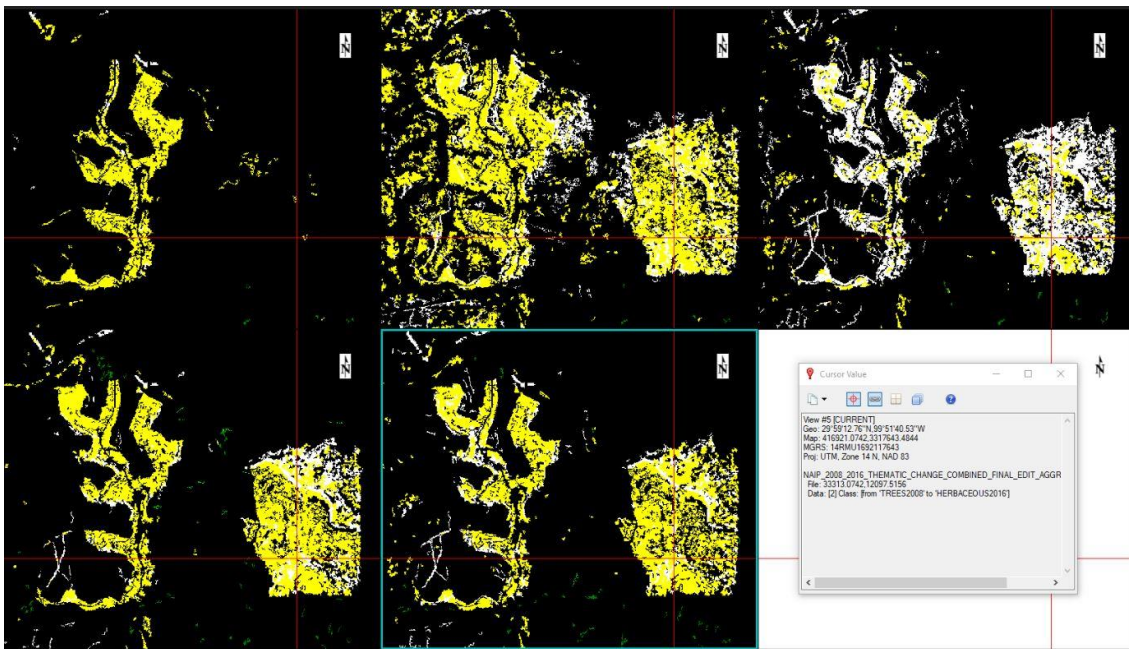


Figure 49. Aggregated thematic change maps from 2008 to all other years (with 2010, 2012, 2014 above and 2015 and 2016 below and aligned from left to right). Dark color indicates no change, yellow indicates change from trees to herbaceous, and white indicates change from trees to unvegetated.

According to the original change detection analysis, the total change between trees and the other two classes ranged from 14% to 20 % of the total area. On the other hand, aggregated change detection statistics indicated that total interclass changes varied

between 1.84% and 6.83% of the total area. Since the changes between these classes were multi-directional, the final gain and loss values were important. The intensity of brush control peaked between 2012 and 2014. I also observed this before change detection analysis by visual interpretation of both classified and unclassified images as demonstrated in Figure 50.

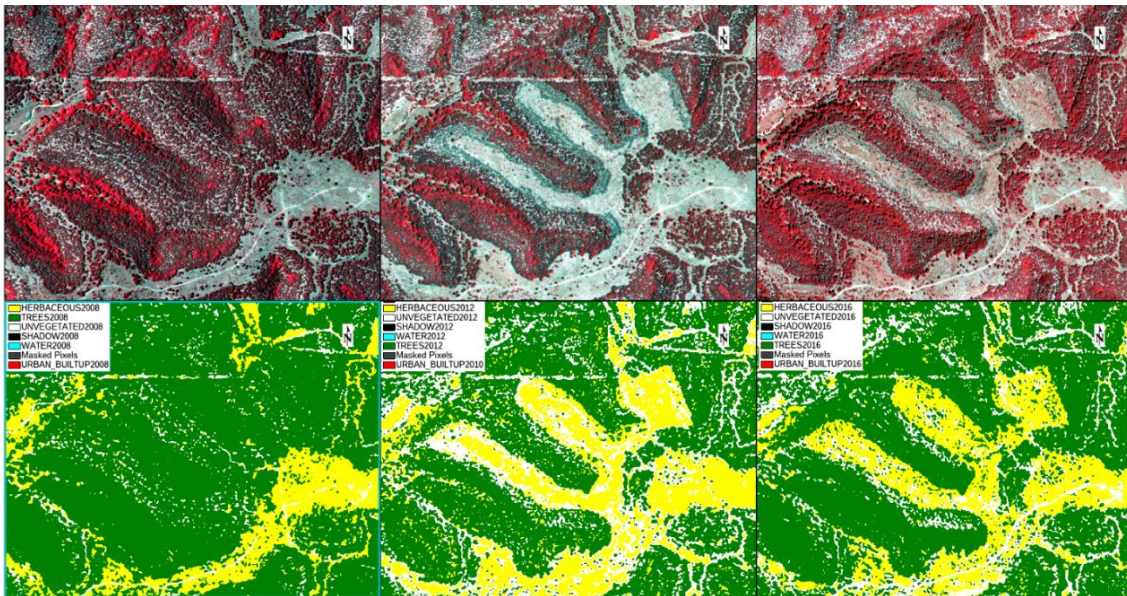
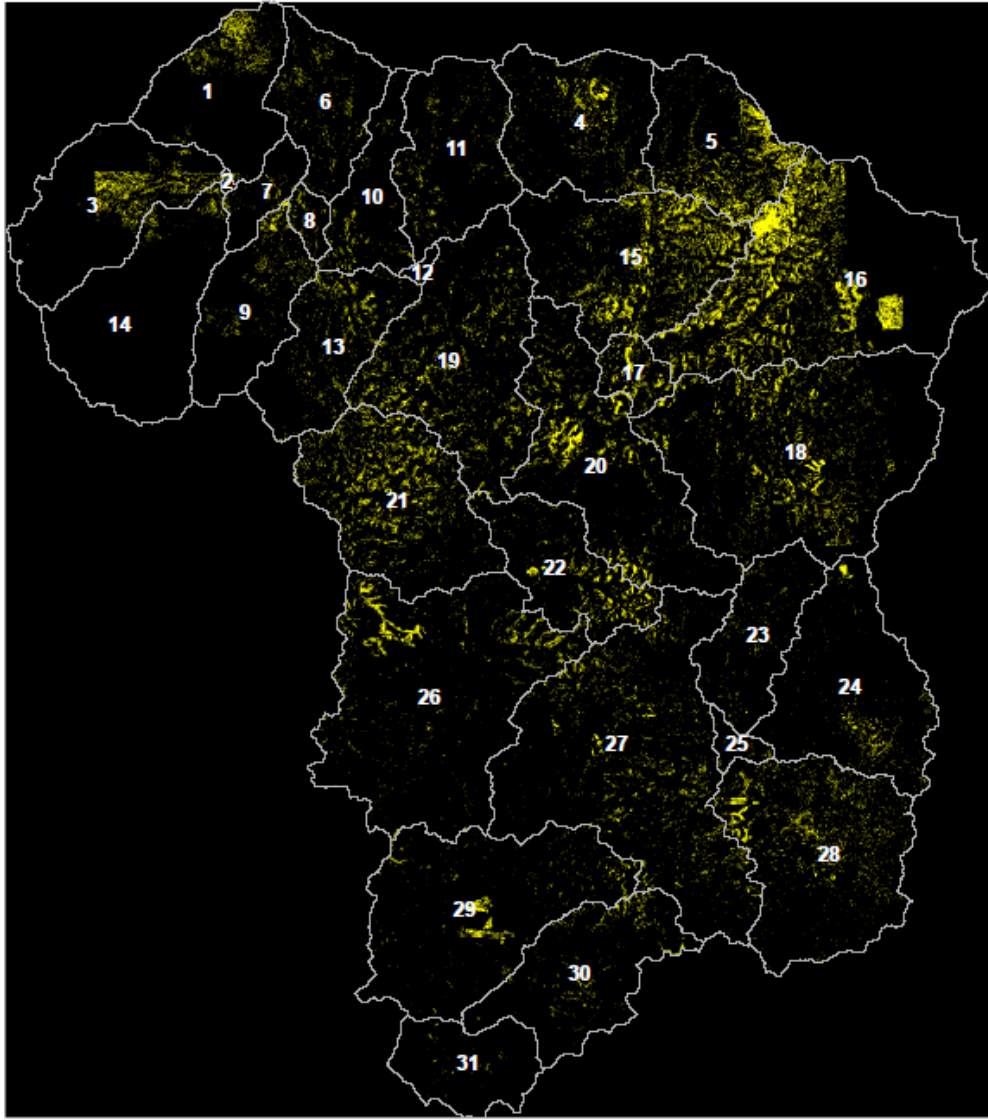



Figure 50. Land cover change at a brush management cite in the study area. Images from left to right are 2008, 2012 and 2016 with the NIR false color composites above and the classified images below.

The largest brush management activities took place between 2008 and 2014 and covered an area of 48.87 square kilometers (5.39 % of the total area). Figure 51 shows the spatial distribution of brush control activities took place in the entire study area between 2008 and 2014.


DISTRIBUTION OF JUNIPER COVER CHANGE
FROM 2008 TO 2014



Legend

 SUBBASINS

Juniper Cover Change 2008 - 2014

 Juniper Treatment


 No Juniper Treatment



Figure 51. Spatial distribution of change from juniper cover to herbaceous and barren (from 2008 to 2014).

IV.3 Statistical Relationship Between Annual Rainfall, Tree Cover and Water Yield

According to the results of the multiple regression analysis shown in Table 42, 93% of the change in the water yield can be explained jointly by annual rainfall and tree cover with a 95% confidence level. However, the effect of tree cover was insignificant (p -value = 0.663) while rainfall had a significant impact (p -value = 0.032).

Table 42. Multiple regression results of annual precipitation, tree cover, and water yield.

<i>Regression Statistics</i>					
Multiple R	0.964				
R Square	0.93				
Adjusted R Square	0.883				
Standard Error	7.20				
Observations	6				
<i>ANOVA</i>					
	<i>df</i>	<i>SS</i>	<i>MS</i>	<i>F</i>	<i>Significance F</i>
Regression	2	2065.79	1032.89	19.92	0.019
Residual	3	155.53	51.84		
Total	5	2221.32			
	<i>Coefficients</i>	<i>Standard Error</i>	<i>t Stat</i>	<i>P-value</i>	
Intercept	-57.48	48.91	-1.18	0.33	
Tree Cover(km ²)	0.056	0.12	0.48	0.66	
Annual Rainfall (mm)	0.101	0.03	3.80	0.03	

Linear regression results of water yield-rainfall and water yield-tree cover is shown in Table 43. All in all, the impact of tree cover on water yield wasn't significant at the 5% significant level in both statistical tests. This result, though derived from a small sample, is counterintuitive to the findings of some previous studies in which they

found brush management led to a positive impact on water yield [13, 16, 30]. This study revealed that an area of about 42 square kilometers was converted from brush to herbaceous and unvegetated in 2012. Although the annual rainfall in 2012 (557.18 mm) was higher than that in 2009 (475.29 mm) and 2011 (325.9 mm), the water yield percentage in 2012 (3.57%) remained below that in 2009 (5.40%) and 2011 (5.13%).

Table 43. Linear regression of water yield on rainfall (top) and tree cover (bottom).

Summary of Fit (Rainfall and Water Yield)					
RSquare		0.93			
RSquare Adj		0.91			
Root Mean Square Error		6.47			
Mean of Response		37.55			
Observations (or Sum Wgts)		6			
Analysis of Variance (Rainfall and Water Yield)					
Source	DF	SS	MS	F Ratio	Significance
Model	1	2053.80	2053.8	49.04	0.0022
Error	4	167.53	41.88		
C. Total	5	2221.32			
Summary of Fit (Tree cover and Annual Water Yield)					
RSquare		0.59			
RSquare Adj		0.49			
Root Mean Square Error		15.03			
Mean of Response		37.55			
Observations (or Sum Wgts)		6			
Analysis of Variance (Tree cover and Annual Water Yield)					
Source	DF	SS	MS	F Ratio	Significance
Model	1	1317.46	1317.46	5.83	0.0732
Error	4	903.87	225.97		
C. Total	5	2221.32			

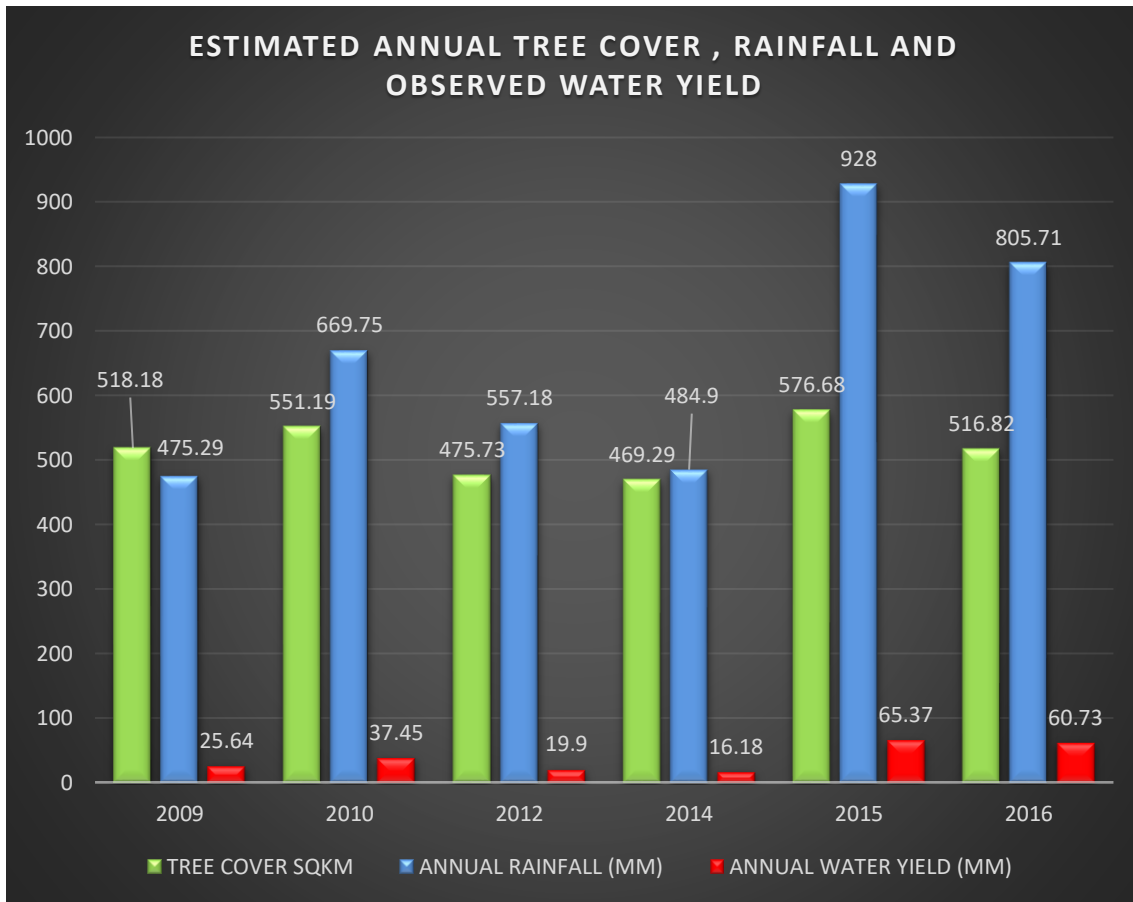


Figure 52. Annual tree cover, rainfall and water yield in the study area.

Figure 52 shows the annual water yield, tree cover and rainfall of all years having the data. The measured water yield was the lowest in 2014 which also had the lowest tree cover of all years included in the analysis. Besides, the amount of rainfall in 2014 (484.9 mm) was higher than that in 2009 (475.29 mm). The decline in the water yield in 2012 and 2014 could be resulted from the increased surface runoff due to a significant amount of brush removal in those years. Because the study area is composed of karst watersheds, karstic features like depressions and sinkholes can trap the water coming via

overland flow. The study area falls into a semi-arid climate zone. The water accumulated especially in uncovered sinkholes and depressions can easily be evaporated following the storm events due to relatively high potential evapotranspiration rates in semi-arid regions.

According to Dammeyer et al., water is stored in the deeper parts of the epikarst and cannot be accessed by the juniper roots [22]. They noted that previous water content of the soil and pattern of the rainfall are key factors which can enable bypass flow and generate deep recharge [22]. The results of the statistical tests and observations also comply with the finding of Wilcox and Huang (2010) that in karst watersheds where springs exist, and soils are shallow, degradation (removal of vegetative cover, mostly human-induced) leads to a reduction in water yield. They also marked that brush encroachment favored the increase in water yield in such an environment where baseflow is the dominant component of the stream flow [12]. I found that baseflow contribution to streamflow accounts for about 80% of the total flow in the study area. This finding also supports the notion that the infiltration capacity of soil was reduced following the removal of junipers reducing the groundwater flow and stream flow [12].

IV.4 Quantified 3rd Level LULC Classes within The NLCD 2011 Classes

The area of varying land cover features which are included in the NLCD 2011 LULC map categories for the study area is shown in Table 44. The quantification of the higher-level classes in each NLCD category indicated that barren area computed by the aerial image classification involved in every major NLCD land use cover classes with varying intensity. The barren area in NLCD classes ranged from 7.86% in evergreen forest class to 17.98% in brush class. This outcome explains the higher surface runoff initially simulated by the SWAT-NAIP model. Because the SWAT model clumped scattered barren pixels in a subbasin, the surface runoff estimated by SWAT-NAIP models was higher than the SWAT-NLCD and SWAT-LANDSAT models before parameterizations applied to the models. So, it is obvious that the model cannot account for the full connectivity between different land cover types.

Another point to make, the oak cover was quantified inside the deciduous category covered 10.55% of the class area while juniper covered 68.55%. This result indicates the low accuracy of NLCD data, especially in mapping deciduous tree cover. Furthermore, this result implies that NLCD data cannot provide sufficiently precise information on land use cover. Even though the classification scheme of the NLCD and aerial image classifications are different, higher resolution image classifications can be a much better alternative for supporting decision making in natural resource management.

Table 44. Area of each land use and cover class mapped using higher-resolution aerial images inside the community-level classes of the NLCD 2011 dataset.

NLCD 2011 (30m)	Area (Km ²)	Percent Study Area	Higher Res. Map (1m)	Area in NLCD Class (Km ²)	Area %
Brush	543.37	59.91	Juniper	166.93	30.72
			Herbaceous	210.29	38.70
			Oak	66.75	12.28
			Barren	97.68	17.98
			Shadow	0.02	0.00
			Water	0.88	0.16
			Urban/Built-up	0.43	0.08
Evergreen Forest	225.67	24.88	Juniper	152.11	67.41
			Herbaceous	15.52	6.88
			Oak	40.04	17.74
			Barren	17.75	7.86
			Shadow	0.01	0.00
			Water	0.15	0.07
			Urban/Built-up	0.01	0.01
Deciduous Forest	92.31	10.18	Juniper	63.29	68.55
			Herbaceous	8.91	9.65
			Oak	9.74	10.55
			Barren	10.31	11.17
			Shadow	0.00	0.00
			Water	0.04	0.05
			Urban/Built-up	0.01	0.01
Grassland/ Herbaceous	23.56	2.60	Juniper	5.17	21.93
			Herbaceous	11.14	47.30
			Oak	3.03	12.87
			Barren	4.06	17.23
			Shadow	0.00	0.01
			Water	0.12	0.52
			Urban/Built-up	0.04	0.16

IV.5 Model Results

IV.5.1 Calibration and Sensitivity Analysis

The results of the sensitivity analysis are shown in Table 45 revealed that SOL_AWL, GW_DELAY, GWQMN, CH_K2, and SOL_K were the most sensitive parameters. While CN2 was reported by most studies to be one of the most sensitive parameters, the sensitivity of CN2 for the model was insignificant. Because the models are calibrated by the incorporation of manual and automatic calibration are very rare may explain this outcome. To elaborate, because I adjusted CN2 for each major land use and cover class and hydrological soil group based on the values from the most recent literature, before importing the model simulation into SWAT-CUP, no significant further adjustments were made to CN2 parameters by the SUFI2 algorithm. Thereby, I was able to decrease the model uncertainty caused by CN2 values. Similarly, the uncertainty decreased for a considerable number of parameters following the adjustments prior to autocalibration. So, beginning even from the first iteration in SWAT-CUP, I could obtain satisfactory uncertainty estimates for the calibration of the model considering the R square and NSE. Table 46 shows the results of the calibration of the pre-processed and default SWAT-NAIP model.

Table 45. The results of the sensitivity analysis conducted by following the automatic calibration of previously adjusted parameters.

PARAMETER SENSITIVITY ANALYSIS				
Par.Number	Parameter Name	Function	t-Stat	P-Value
1	SOL_AWC(..).sol	absolute	16.19	0.00
2	GW_DELAY.gw	replace	4.70	0.00
3	GWQMN.gw	replace	3.11	0.00
4	CH_K2.rte	replace	-1.89	0.06
5	SOL_K(..).sol	relative	-1.83	0.07
6	RCHRG_DP.gw	replace	-1.23	0.22
7	ESCO.hru	replace	-1.23	0.22
8	ALPHA_BF.gw	replace	-1.07	0.29
9	OV_N.hru	replace	0.83	0.41
10	SURLAG.bsn	replace	0.64	0.52
11	GW_REVAP.gw	replace	0.60	0.55
12	CH_K1.sub	replace	0.23	0.82
13	CN2.mgt	relative	0.12	0.90
14	REVAPMN.gw	replace	0.11	0.92
15	CANMX.hru	replace	0.04	0.97

Table 46. Pre-Processed and default SWAT-NAIP Calibration Results.

SWAT-NAIP PRE-PROCESSED MODEL CALIBRATION RESULTS (2012-2015)									
Iteration No	Simulation Count	Crack Flow	Karst Features Considered	Par. Count	R Square	NSE	Mean Sim.	Mean Obs.	PBIAS
3	500	Active	YES	49	0.89	0.63	1.44	0.93	-55.7
7	250	Active	YES	50	0.67	0.6	1.2	0.93	-29.9
8	650	Active	YES	50	0.71	0.63	1.22	0.93	-31.8
SWAT-NAIP DEFAULT MODEL CALIBRATION RESULTS (2012-2015)									
Iteration No	Simulation Count	Crack Flow	Karst Features Considered	Par. Count	R Square	NSE	Mean Sim.	Mean Obs.	PBIAS
3	250	Inactive	NO	37	0.54	-2.43	1.98	0.93	-114.5
5	100	Inactive	YES	39	0.49	0.48	0.93	0.93	-0.7
7	250	Inactive	YES	39	0.58	0.57	0.90	0.93	2.6
11	75	Inactive	YES	30	0.61	0.6	0.89	0.93	4.3

Every best parameter set of the calibrated pre-processed models yielded significantly higher mean values and percent bias. I reported the best parameters of two iterations for the pre-processed model calibration which is shown in Table 47.

Table 47. The best parameters of the pre-processed SWAT-NAIP calibration from iterations 7 and 8.

	Parameters	Func.	LULC	Main Chnl Flow	Hyd. Grp	Pre-processed Model Value	ITER 7	ITER 8
1	cn2.mgt	replace	JUNI		A	25	18.466	18.343
2	cn2.mgt	replace	JUNI		B	38	37.521	37.609
3	cn2.mgt	replace	JUNI		C	48	44.291	44.310
4	cn2.mgt	replace	JUNI		D	53	52.085	51.520
5	cn2.mgt	replace	OAK		A	45	23.787	23.807
6	cn2.mgt	replace	OAK		B	66	34.756	40.531
7	cn2.mgt	replace	OAK		C	77	53.218	53.751
8	cn2.mgt	replace	OAK		D	83	64.910	65.675
9	cn2.mgt	replace	RNGE		A	49	35.791	35.884
10	cn2.mgt	replace	RNGE		B	69	57.898	58.465
11	cn2.mgt	replace	RNGE		C	79	60.735	61.017
12	cn2.mgt	replace	RNGE		D	84	65.972	63.549
13	cn2.mgt	replace	BARR		A	77	65.155	64.994
14	cn2.mgt	replace	BARR		B	86	66.310	66.512
15	cn2.mgt	replace	BARR		C	91	70.139	69.213
16	cn2.mgt	replace	BARR		D	94	73.496	75.034
17	esco.hru	replace	JUNI			0.53	0.463	0.457
18	esco.hru	replace	OAK			0.6	0.633	0.635
19	esco.hru	replace	RNGE			0.65	0.632	0.645
20	esco.hru	replace	BARR			0.7	0.630	0.638
21	canmx.hru	replace	JUNI			3.17	5.829	5.833
22	canmx.hru	replace	OAK			3	4.140	3.888
23	canmx.hru	replace	RNGE			1.8	2.197	2.408
24	sol_awc(..).sol	add				0.1(a)	0.066	0.121
25	gw_delay.gw	replace		Cont.		1	218.578	232.119
26	rcharg_dp.gw	replace		Cont.		0.7	0.538	0.463
27	ch_k2.rte	replace		Cont.		default	31.320	16.486
28	alpha_bf.gw	replace		Cont.		0.012	0.012	0.011
29	sol_k(..).sol	relative		Cont.		default	-0.305	-0.293
30	gwqmn.gw	replace		Cont.		5	495.966	502.494
31	revapmn.gw	replace		Cont.		500	303.404	296.323

Table 46 continued

	Parameters	Func.	LULC	Main Chnl Flow	Hyd. Grp	Pre-processed Model Value	ITER 7	ITER 8
32	revapmn.gw	replace		Intrm.		500	301.016	295.568
33	gwqmn.gw	replace		Intrm.		5	2.83	1.939
34	sol_k(..).sol	relative		Intrm.		default	0.168	0.182
35	gw_delay.gw	replace		Intrm.		1	0.205	0.493
36	rchrg_dp.gw	replace		Intrm.		0.7	0.825	0.846
37	alpha_bf.gw	replace		Intrm.		0.012	0.998	0.983
38	ch_k2.rte	replace		Intrm.		default	260.06	257.887
39	gw_revap.gw	replace	JUNI			0.065	0.088	0.087
40	gw_revap.gw	replace	OAK			0.06	0.068	0.07
41	gw_revap.gw	replace	RNGE			0.056	0.048	0.051
42	gw_revap.gw	replace	BARR			0.05	0.054	0.053
43	ov_n.hru	replace	JUNI			0.5	0.764	0.755
44	ov_n.hru	replace	OAK			0.4	0.745	0.74
45	ov_n.hru	replace	RNGE			0.3	0.205	0.204
46	ov_n.hru	replace	BARR			0.2	0.108	0.105
47	surlag.bsn	replace	JUNI			20	19.472	18.789
48	surlag.bsn	replace	OAK			16	14.477	14.627
49	surlag.bsn	replace	RNGE			12	9.62	9.004
50	surlag.bsn	replace	BARR			8	6.751	6.201

Unlike the pre-processed model calibration, default model calibration generated very comparable mean simulated flow to observed flow. With respect to very close average simulated flow, percent bias was very low for the calibration of the default SWAT model. This implied that crack flow activation led the model to misrepresent a sizable portion of the small peaks which is demonstrated in Figure 53.

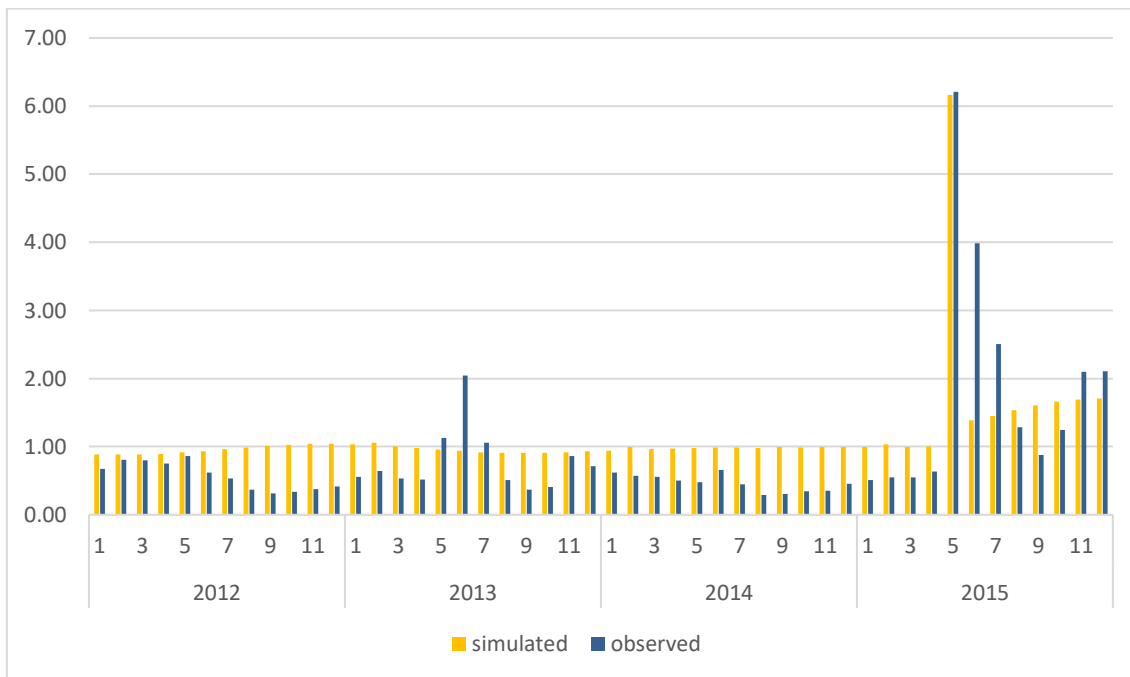


Figure 53. The best simulation results of iteration 8 for the pre-processed SWAT-NAIP calibration.

Calibration of the default model without considering the subbasins with different flow conditions yielded very unsatisfactory results. The results shown in Figure 54 indicated that the model substantially overestimated the streamflow and produced more peaks compared to the observed flow.

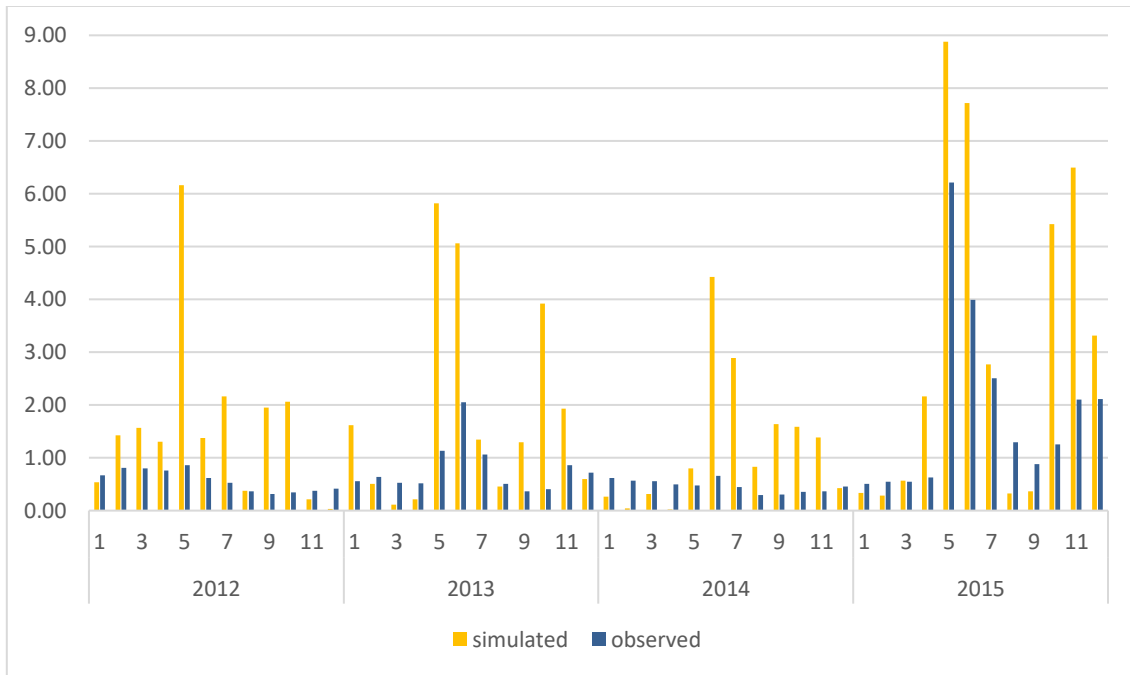


Figure 54. The best simulation result of iteration 3 for the default SWAT-NAIP calibration model. Karst features weren't considered in the parametrization.

Because karst watersheds are very heterogenous and complex, it is quite difficult to express a certain reason residing behind the overestimated flow. There is little potential that this negative bias can be substantially decreased with a thorough examination of parameters and more iteration if the cumulative flow measured at the USGS gage missing some portion of the flow due to the transport of water via subsurface conduits. Because the NSE and R^2 values crossed the minimum threshold to be counted as satisfactory and percent bias values were more satisfactory for the default SWAT-NAIP model which considers the karst features, I used the best parameter set shown in Table 48 derived from the calibration of the default SWAT model for the model validation.

Table 48. The best parameters of the iteration 7 for the default SWAT-NAIP calibration.

NO	Parameter Name	Math. Operation	LULC	Fitted Value	Min value	Max value	SUBBASINS
1	CN2.mgt	Relative	JUNI	-0.100	-0.123	0.019	
2	CN2.mgt	Relative	OAK	-0.090	-0.126	0.035	
3	CN2.mgt	Relative	RNGE	-0.172	-0.269	-0.090	
4	CN2.mgt	Relative	BARR	-0.315	-0.316	-0.226	
5	ESCO.hru	Replace	JUNI	0.549	0.501	0.559	
6	ESCO.hru	Replace	OAK	0.537	0.500	0.580	
7	ESCO.hru	Replace	RNGE	0.612	0.500	0.800	All
8	ESCO.hru	Replace	BARR	0.785	0.600	0.900	
9	CANMX.hru	Replace	JUNI	4.119	3.795	4.600	
10	CANMX.hru	Replace	OAK	3.899	3.091	4.366	
11	CANMX.hru	Replace	RNGE	1.524	1.250	2.102	
12	SOL_AWC(.).sol	Add		0.523	0.335	0.551	
13	GW_DELAY.gw	Replace		147.591	80.192	241.433	
14	RCHRG_DP.gw	Replace		0.479	0.403	0.711	
15	CH_K2.rte	Replace		6.264	0.000	66.642	
16	ALPHA_BF.gw	Replace		0.014	0.012	0.016	With Continuous Flow
17	SOL_K(.).sol	Relative		-0.495	-0.494	-0.496	
18	GWQMN.gw	Replace		258.323	184.417	454.146	
19	REVAPMN.gw	Replace		439.884	406.787	731.270	
20	REVAPMN.gw	Replace		145.929	129.749	390.709	
21	GWQMN.gw	Replace		5.653	2.493	5.996	
22	SOL_K(.).sol	Relative		0.195	0.175	0.226	
23	GW_DELAY.gw	Replace		0.551	0.417	0.981	With Losing Streams
24	RCHRG_DP.gw	Replace		0.780	0.665	0.989	
25	ALPHA_BF.gw	Replace		0.933	0.898	0.978	
26	CH_K2.rte	Replace		307.433	258.810	313.442	
27	GW_REVAP.gw	Replace	JUNI	0.070	0.065	0.076	
28	GW_REVAP.gw	Replace	OAK	0.062	0.060	0.070	
29	GW_REVAP.gw	Replace	RNGE	0.033	0.028	0.049	
30	GW_REVAP.gw	Replace	BARR	0.049	0.032	0.051	
31	OV_N.hru	Replace	JUNI	0.562	0.417	0.606	
32	OV_N.hru	Replace	OAK	0.469	0.458	0.590	
33	OV_N.hru	Replace	RNGE	0.293	0.260	0.344	All
34	OV_N.hru	Replace	BARR	0.119	0.101	0.127	
35	SURLAG.bsn	Replace	JUNI	21.861	16.415	24.000	
36	SURLAG.bsn	Replace	OAK	11.833	9.876	13.654	
37	SURLAG.bsn	Replace	RNGE	8.256	5.000	9.000	
38	SURLAG.bsn	Replace	BARR	6.525	4.680	8.606	
39	ESCO.bsn	Replace		0.678	0.585	0.783	

The best simulation result of the default SWAT-NAIP model with the parameter set 7 is shown in Figure 55. As shown in Figure 55, simulated streamflow was more comparable to observed streamflow given the higher streamflow was simulated by the pre-processed SWAT-NAIP model.

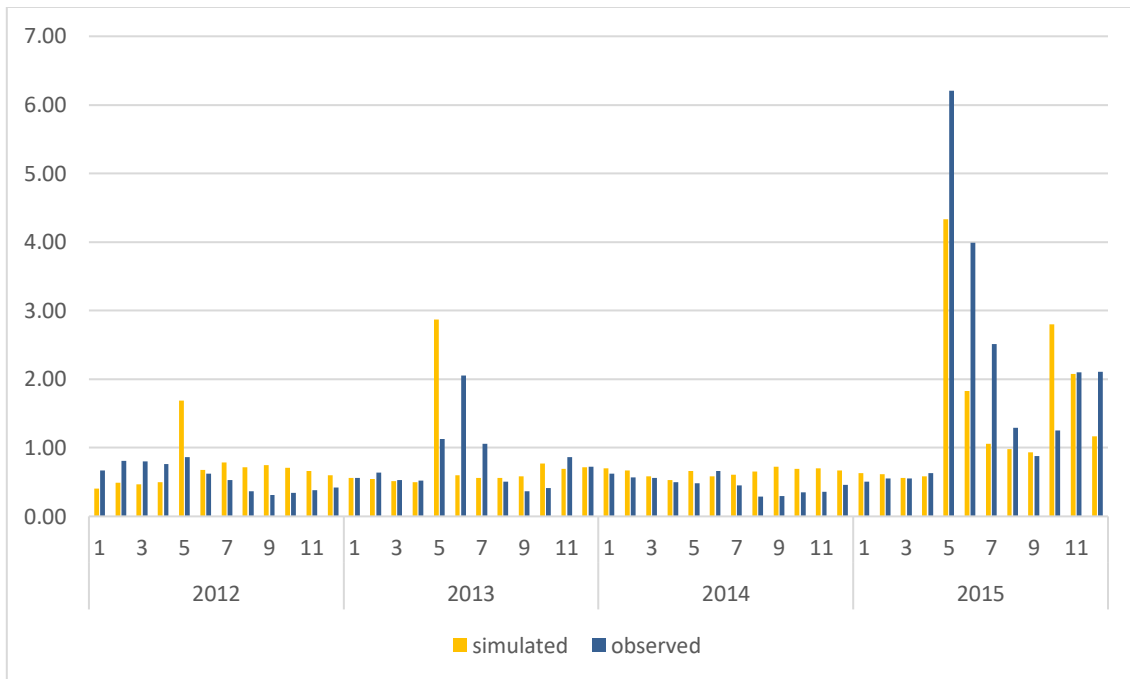


Figure 55. The best simulation of the default SWAT-NAIP calibration iteration 7.

Calibration of the SWAT-LANDSAT model produced satisfactory results. Table 49 shows the results of the successful iterations derived from the calibration of the SWAT-LANDSAT model. Figure 56 and 57 show the relationship between simulated streamflow by the SWAT-LANDSAT model and observed streamflow.

Table 49. Calibration results of the SWAT-LANDSAT model.

DEFAULT SWAT-LANDSAT MODEL CALIBRATION RESULTS (2012-2015)									
Iteration No	Simulation Count	Crack Flow	Karst Features Considered	Par. Cnt.	R ²	NSE	Mean Sim.	Mean Obs.	PBIAS
6	150	Inactive	YES	59	0.6	0.58	1.08	0.93	-16.15
8	500	Inactive	YES	44	0.69	0.68	0.99	0.93	-6.80

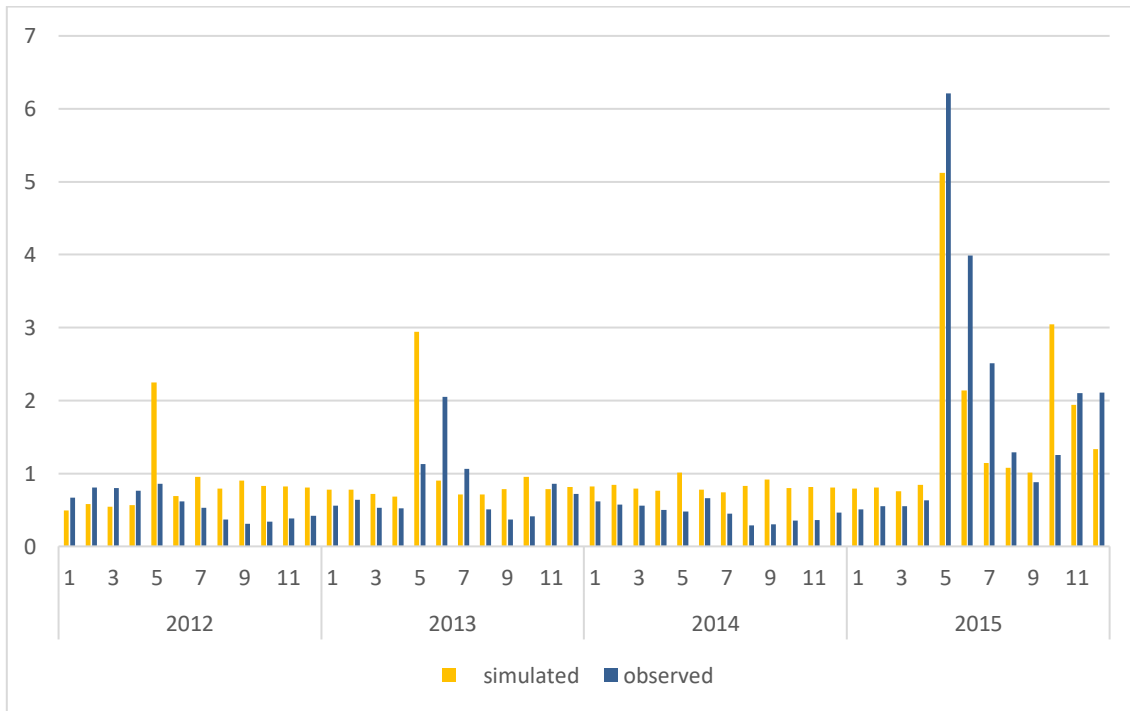


Figure 56. The best simulation result of iteration 6 for the SWAT-LANDSAT calibration.

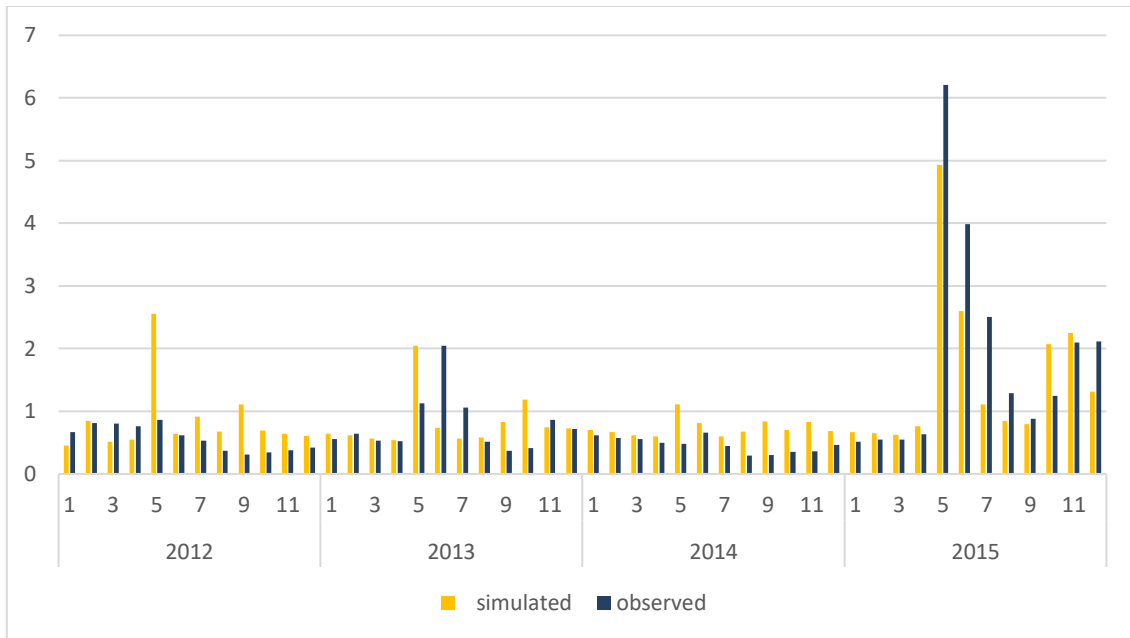


Figure 57. The best simulation result of iteration 8 for the SWAT-LANDSAT calibration.

IV.5.2 Results of the Model Validation

I used the parameter set 7 and 11 from the calibration of the default SWAT-NAIP model for validation. For validation of the pre-processed SWAT-NAIP model, I used the calibrated parameter set 8. Table 50 shows the results of the validation of the default and pre-processed SWAT-NAIP models.

Table 50. Validation results of the SWAT-NAIP models for the data period of 2016-2017.

Parameter Set Number	Model Category	Warm-Up Year Cnt	R ²	NSE	Mean Simulated	Mean Observed	BIAS (%)
8	PRE-PROC.	0	0.07	-2.14	1.07	1.46	26.8
8	PRE-PROC.	4	0.42	0.09	1.79	1.46	-22.9
7	DEFAULT	4	0.15	0.14	1.49	1.46	-2.2
11	DEFAULT	4	0.07	0.05	1.55	1.46	-6.1

For the SWAT-LANDSAT model, calibrated parameter sets 6 and 8 were used respectively during the validation in SWAT-CUP. As I mentioned earlier, I tried to validate the SWAT-NLCD model for the 2012-2015 period with the parameters obtained for the Nueces Headwaters Watershed in a previous modeling study [47]. Table 51 shows the validation results of the SWAT-LANDSAT and SWAT-NLCD models.

Table 51. Validation results of the SWAT-LANDSAT and SWAT-NLCD models.

THE SWAT-LANDSAT MODEL (2016-2017)									
Parameter Set Number	Simulation Count	Crack Flow	Karst Features Considered	Parameter Count	R ²	NSE	Mean Sim.	Mean Obs.	PBIAS
6	150	Inactive	YES	59	0.01	-9.55	2	1.46	-37.30
8	500	Inactive	YES	44	0.13	0.01	1.58	1.46	-7.90
THE SWAT-NLCD MODEL (2012-2015)									
Parameter Set Number	Simulation Count	Crack Flow	Karst Features Considered	Parameter Count	R ²	NSE	Mean Sim.	Mean Obs.	PBIAS
1	150	Inactive	YES	17	0.58	-3.77	2.57	0.92	-178.4

Unfortunately, none of the calibrated parameter sets yielded satisfactory R^2 and NSE statistics for the validation processes. However, the percent bias obtained from the validation processes was the lowest and within the very reasonable range for the default SWAT-NAIP model. Figure 58 shows the observed and simulated streamflow obtained from the default SWAT-NAIP model which produced relatively better results.

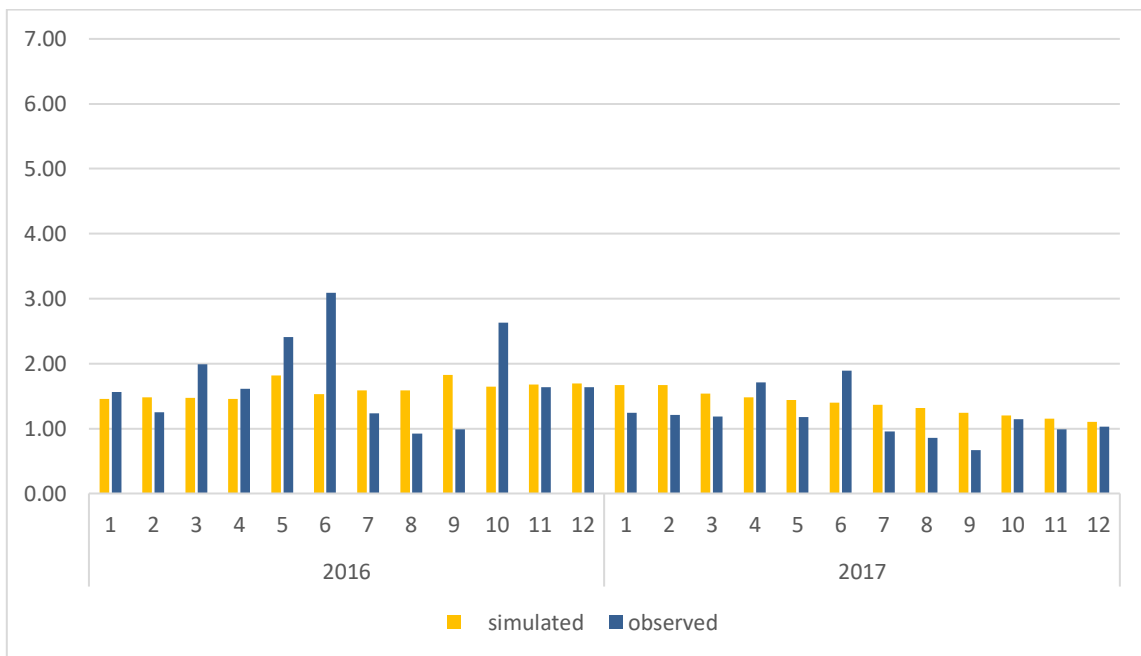


Figure 58. Validation simulation of the SWAT-NAIP model with calibrated parameter set 7 of the default model.

Because I didn't specify a model warm-up period for the validation of the pre-processed SWAT-NAIP model, the SWAT model didn't simulate streamflow for the first half of 2016 which is shown in Figure 59. To compensate for this issue, I switched on the crack flow code of the default validation model by editing the file.cio in the

SWAT-CUP project. I imported the best parameters of the iteration 8 obtained from the pre-processed SWAT-NAIP model calibration. Because a 4 year-warm-up period specified in this validation, the results were different. R^2 value increased from 0.07 to 0.42 and NSE increased from -2.14 to 0.09. Percent bias was the statistics changed the most. It changed from a positive value of 26.8 to a negative value of -22.9. This outcome underscores the necessity of specifying at least one year as the model's warm-up period. Figure 60 shows the simulation result of the pre-processed SWAT-NAIP model validation after defining a 4-year warm-up period.

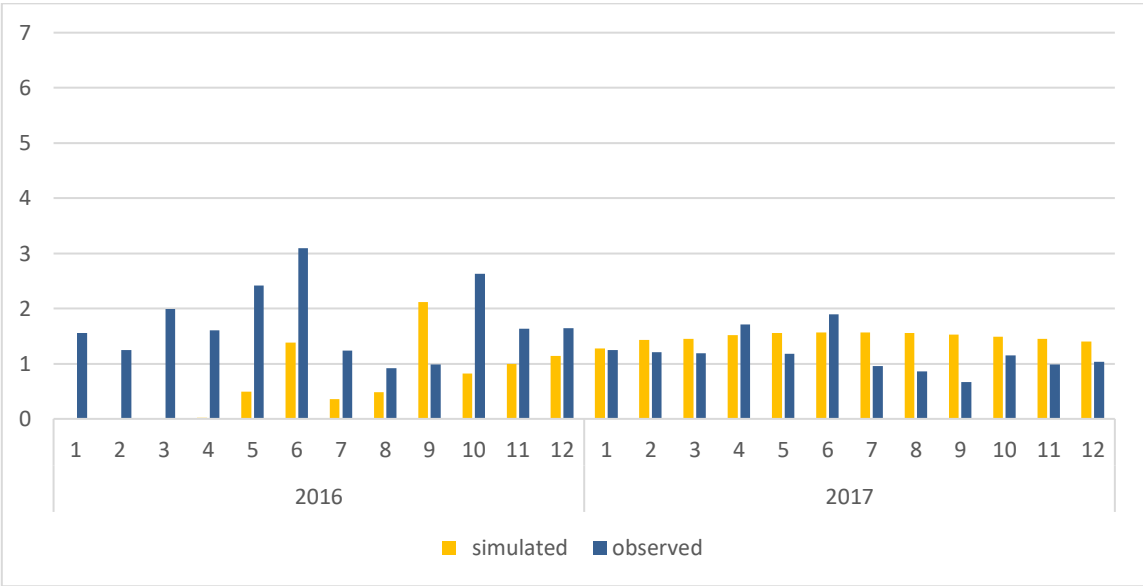


Figure 59. The result of the validation simulation of the SWAT-NAIP model with the parameter set 8 from the preprocessed model calibration. No warm-up period was specified.

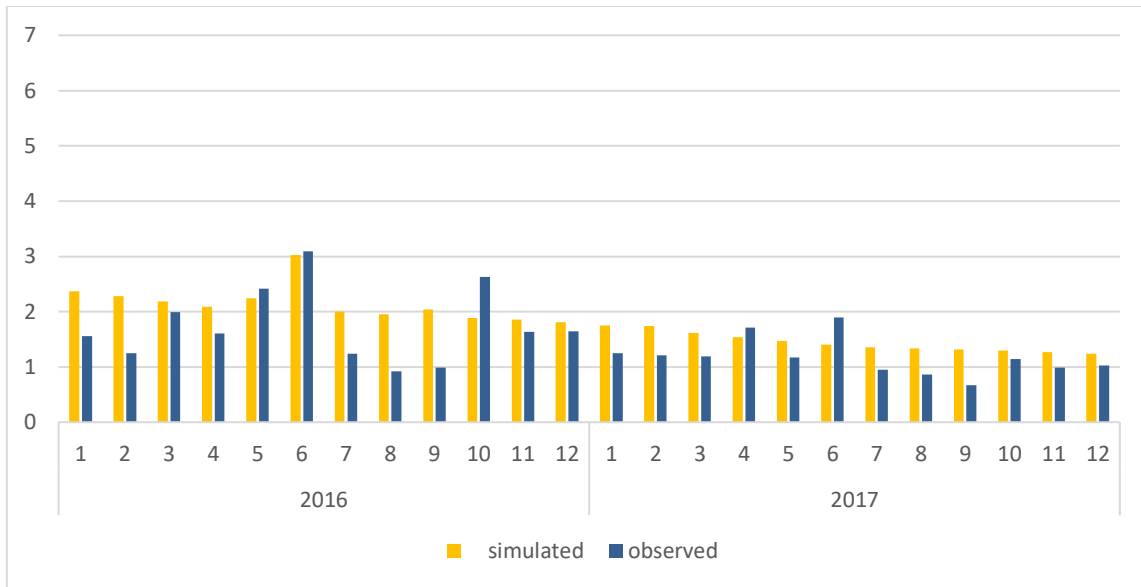


Figure 60. Validation simulation of the pre-processed SWAT-NAIP model after specifying a 4-year warm-up period.

The percent bias resulted from the validation of the SWAT-LANDSAT model was also in the acceptable range whereas the R^2 and NSE remained below the acceptable range. Figure 61 shows the simulation result of the SWAT-LANDSAT model validation.

Parameters used to validate the SWAT-NLCD model is shown in Table 52. Although the calibrated parameters proved to yield good statistics in the Jain et al.’s study for the same ecohydrological and geological setting, they didn’t yield good statistics for the validation of the SWAT-NLCD model in this study. Both NSE and PBIAS statistics were below the acceptable range in the validation of the SWAT-NLCD model. However, the R^2 value of the SWAT-NLCD validation was 0.58. Figure 62 shows the streamflow simulated by the validation of the SWAT-NLCD model and observed streamflow.

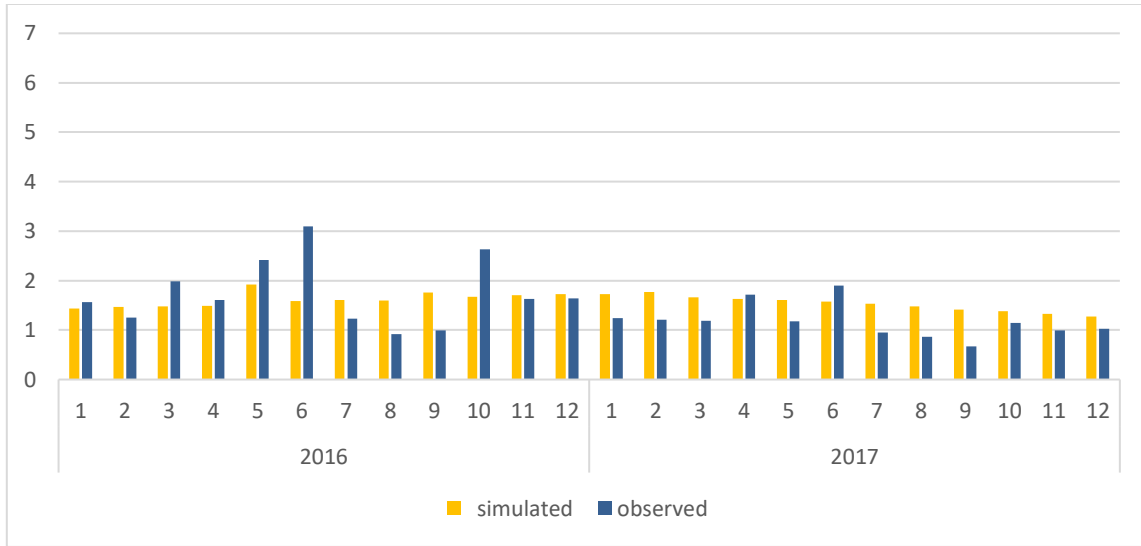


Figure 61. The simulation result of the SWAT-LANDSAT model validation with the calibrated parameter set 8 from the calibration of the model.

Table 52. Parameters based on two previous studies used for SWAT-NLCD model validation. Adapted by Jain et al. (2015) and Qiao et al (2015).

#	Parameter Name	Land Cover	Method	Subbasins	Fitted Value	Min.Value	Max.Value
1	CN2.mgt		Relative	ALL	-0.15	-0.16	-0.15
2	ESCO.hru		Add	ALL	-0.12	-0.09	-0.12
3	CANMX.hru	JUNI	Replace	ALL	3.18	3.15	3.18
4	CANMX.hru	OAK	Replace	ALL	2.60	2.50	3.00
5	CANMX.hru	RNGE	Replace	ALL	1.82	1.70	1.90
6	CANMX.hru	RNGB	Replace	ALL	2.13	1.80	2.20
7	SOL_AWC(..).sol		Add	ALL	0.15	0.09	0.15
8	GW_DELAY.gw		Replace	SUBBASINS WITHOUT SPRINGS	216.08	215.00	220.00
9	CH_K2.rte		Replace	AND	51.35	49.00	52.00
10	ALPHA_BF.gw		Replace	SINKHOLES	0.015	0.01	0.02
11	SOL_K(..).sol		Relative		-0.28	-0.20	-0.30
12	GWQMN.gw		Replace		4.50	4.00	6.00
13	SOL_K(..).sol		Relative	SUBBASINS	0.14	0.14	0.17
14	GW_DELAY.gw		Replace	WITH	1.46	0.90	1.50
15	RCHRG_DP.gw		Add	LOSING STREAMS	0.20	0.19	0.21
16	ALPHA_BF.gw		Replace		0.98	0.90	1.00
17	CH_K2.rte		Replace		245.57	245.00	255.00

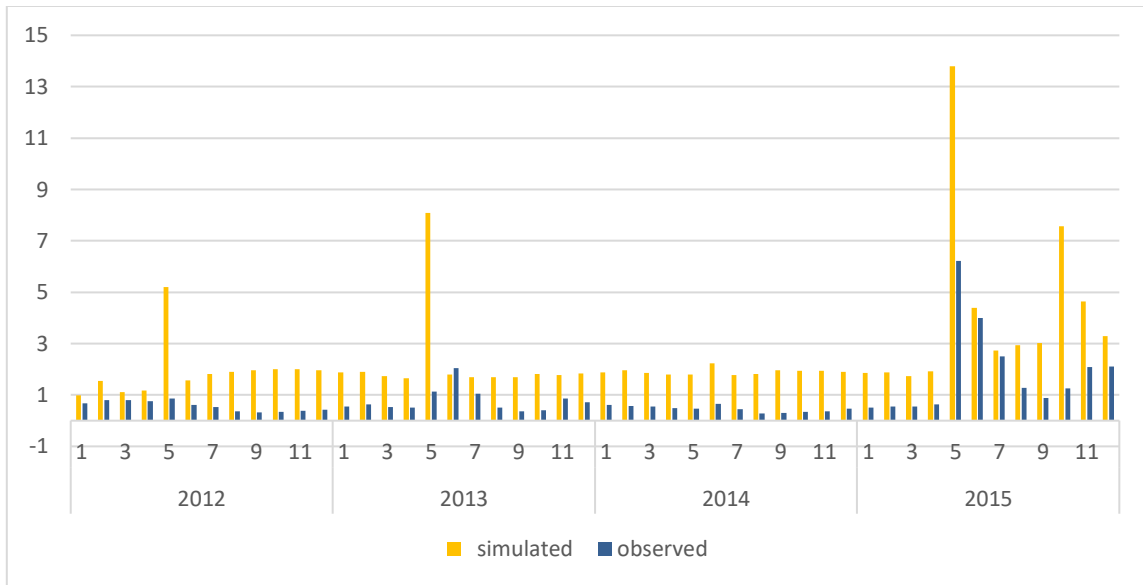


Figure 62. The simulation result of the SWAT-NLCD validation with the calibrated parameters obtained from the literature.

Although the calibration of the default and pre-processed models produced satisfactory statistics, the values degraded substantially for the validation of the models. There can be several reasons for this. First, it was obvious that, a calibration approach which didn't consider the distinctive characteristics of the karst geology yielded poor results compared to the calibration methods accounting for them. Hence, more work is required to better identify and quantify karst features like sinkholes, springs and losing streams in the study area. However, this is beyond the scope of this study given the large size of the watershed. Field studies could take months or even years to map all karst features thoroughly in a large karst watershed like this one.

Second, the previous studies conducted on karst watersheds have modeled either small subbasins with short periods or large watersheds with longer periods. This study,

on the other hand, strives to model a large watershed with a relatively short period. Because antecedent climatic conditions used to calibrate the model are very decisive to the hydrological response of the karst watershed to future weather events like storms, longer periods of calibration and validation data could yield greater consistency between the calibration and validation results. For example, Jain et al. modeled the same watershed by specifying 15 years for each of the calibration and validation periods. A longer time period can reduce the impact of extreme values of some factors (e.g., rainfall) in a specific year on the calibration and validation results, increasing their agreement.

Third, most previous studies modeled the hydrological response of the watershed to LULC changes, usually based on the same LULC data used for model calibration. Therefore, the average values of climate and other variables like land cover are more likely to be similar in the two periods selected for model calibration and validation. Thus, obtaining comparable results from the calibration and validation of the models became a much easier task. With such a modeling approach, satisfactory calibration results can usually guarantee satisfactory validation results due to similar ecological, geological and climatological characteristics of the two periods. In contrast, the calibration and validation periods specified in this study had very distinct climatic and ecological conditions. For example, the average rainfall of the calibration period was 644 mm while it was 715 mm in the validation period. The unusually high rainfall in 2015 (928 mm) increased the average rainfall of the calibration period, forcing the

model to capture the impact of the extreme event at the cost of neglecting the normal conditions prevailing during most of the data period.

At least about 8% of the total juniper cover was removed from 2008 to 2014 by human or climate-induced factors. This indicated that there was LULC change even in such a short modeling period. This implies that using a single LULC data of a given year to model the impact of LULC change over a longer period conflicts with the primary goals of the studies by ignoring the potential land cover changes over the modeling period. Additionally, calibrating the model for the whole watershed by focusing on a specific type of land use and cover change in a small portion of the watershed can also underestimate the potential changes in the rest of the study area. In contrast, I used different LULC datasets for each of the calibration, validation and verification periods. It is obvious that calibrated parameters can't always ensure that the SWAT model estimates the streamflow successfully when the calibration and validation periods have distinct LULC and climate features. This situation may have been compounded given the heterogeneity and unpredictability of the karst watershed.

Fourth, although the stream flow data measured by the USGS has been used very widely for conditioning the hydrological models, this approach have limitations. For example, in late May 2015, the stream flow couldn't be measured by the USGS for four days and had to be estimated. But, the estimated streamflow was quite high compared to the records of the previous and following days. Given the excessive rainfall in May 2015, this could be reasonable. However, there is still some deficiency associated with using only the observed value of one variable from a single location. This limitation was

also addressed by Qiao et al. and Baffaut et al [18, 49]. Also, because the location of the gage was not in the final outlet of the Headwaters Nueces River, some of the incoming flow may have followed a separate way towards to the final outlet via underground conduits which are common in karst geological settings.

The SWAT-NLCD model couldn't produce satisfactory result although I used previously reported calibrated parameters. The only difference was made to the SWAT-NLCD model validation was the inclusion of canopy maximum storage (CANMX) parameters based on Qiao et al.'s study. It was a necessary step because the SWAT model didn't have any value for canopy maximum storage values of different land cover types in the HRU parametrization. I discussed this with Dr. Srinivasan and was told that CANMX values should be inputted to the model. To conclude, even a model constructed with the same source of input data (soil, land use cover, and elevation) and parameterized with the published calibrated parameters for the same hydrological setting couldn't capture the observed streamflow satisfactorily for a period having a distinct climate.

The relatively better calibration and validation results obtained from the SWAT-NAIP models indicated that the resolution of the DEM and LULC data can have an impact in the estimation of the streamflow. A similar finding was formerly reported by Fishers et al. (2017) [52]. They emphasized that this impact was more obvious when estimating the total suspended sediment yield.

IV.5.3 Results of the Verification and Scenario Analysis

I used the parameter set 7 obtained from the calibration of the default SWAT-NAIP model for the model verification and scenario simulation. Because it produced satisfactory statistics for the calibration period and the highest values of R^2 and NSE (though unsatisfactory), the calibrated parameter set 7 was the best alternative. Because there is no measured streamflow for 2008, I specified this year as the model's warm-up period. Using the same parameter ranges which yielded the best parameter set from iteration 7 in SWAT-CUP, I ran an iteration with the same number of simulations as in the calibration process. The R^2 and NSE were also unsatisfactory for the verification period as shown in Table 53. But the PBIAS value was 15.8 and in the acceptable range.

Table 53. Whole verification period modeling results.

SWAT-NAIP MODEL VERIFICATION RESULTS (2009-2011)									
Par Set	Sim. Count	MODEL	Karst Features Considered	Par. Count	R^2	NSE	Mean Sim.	Mean Obs.	PBIAS
7	250	DEFAULT	YES	39	0.03	-0.53	0.63	0.77	15.8

I realized that the SWAT model produced better-simulated streamflow for the second half of the period from June 2010 to December 2011. R^2 value was 0.44 for this period. The simulated results were even closer to the observed values for 2011 with an R^2 of 0.56 which is reported in Table 54. But for the whole verification period, these values were very low depending on the simulation of the first half of the period. The poor performance of the model for the first half of the period may have been resulted

from the short (1 year) model warm-up period. Figure 63 shows the verification simulation for the whole period and Figure 64 shows the simulation for the second half of the period.

Table 54. R² value obtained from the SWAT-NAIP model for the second half and last year of the verification period.

6/2010 to 12/2011	
<i>Regression Statistics</i>	
Multiple R	0.66
R Square	0.44
Adjusted R Square	0.41
Standard Error	0.16
Observations	19
2011	
<i>Regression Statistics</i>	
Multiple R	0.75
R Square	0.56
Adjusted R Square	0.52
Standard Error	0.14
Observations	12

I used the verification SWAT-NAIP model (pre-treatment/benchmark) results to compare the results of the scenario model (post-treatment). SWAT-CUP uses executable files to run SWAT model while doing autocalibration. However, the resulting parameters need to be updated manually using the on-interface tools. So, I updated every calibrated parameter for the verification model using the manual calibration helper on the interface. I used the same parameter values to update the scenario model.

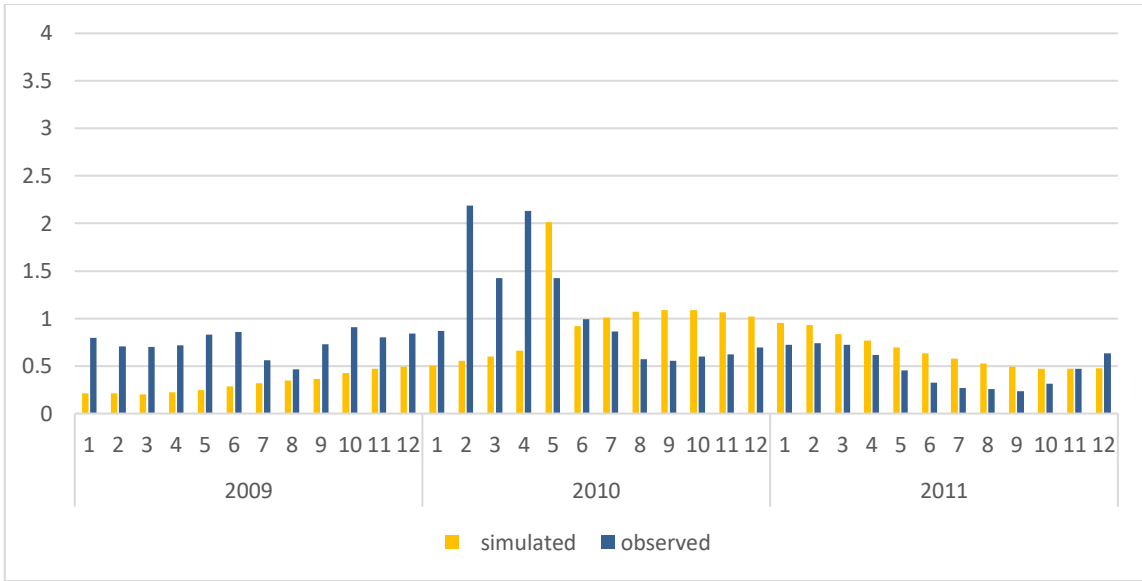


Figure 63. Verification simulation of the SWAT-NAIP model with the parameters obtained from the default model calibration parameter set.

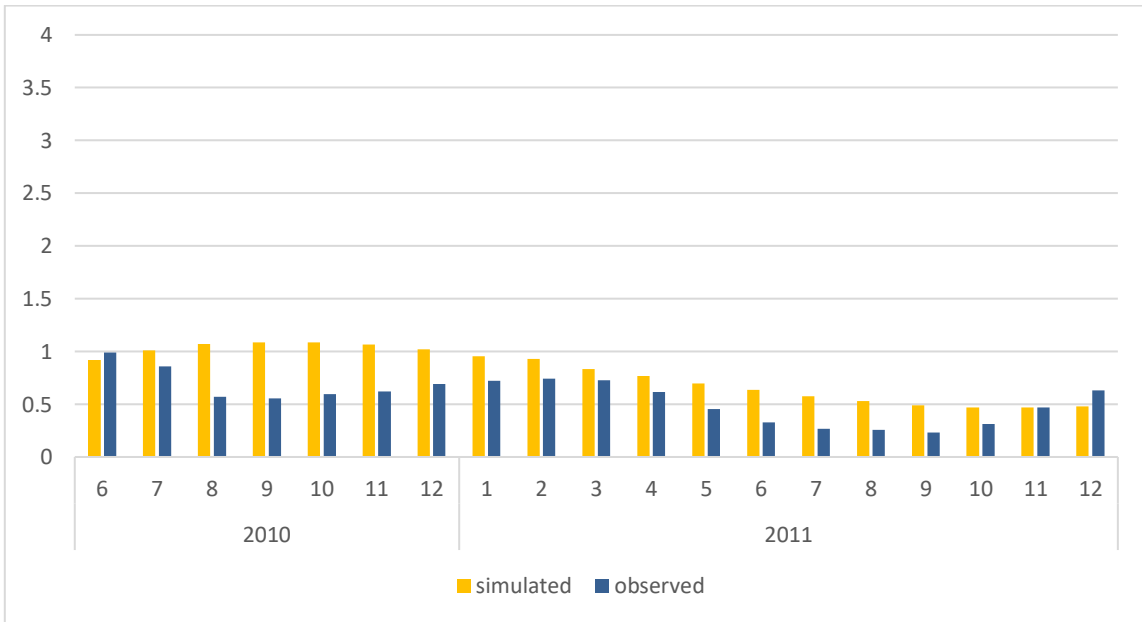


Figure 64. Simulation result of the second half of the verification period.

The hydrological results obtained from the benchmark and scenario simulations were reported in Table 55. Although statistical values especially for the first half of the pre-treatment model were poor, I found simulated water yield, base flow, surface flow, and streamflow ratios were comparable to observed data. The average ET estimated by the benchmark model was about 460 mm per year. This result was comparable to the study of Bednarz et al. (2001) who conducted brush control feasibility studies in the several Texas watersheds including Nueces River Headwater watershed. They reported 533 mm ET with brush condition and 471.62 mm ET without brush condition. The simulated ET was more comparable to the ET simulated in Afinowicz et al.'s study (474.85 mm) [16]. But, there was very insignificant ET change between pre-treatment and post-treatment simulations in this study. Although CANMX, ESCO, GWREVAP parameters for Juniper were approximately two-fold of the range grass, the ET remained almost the same. This can be explained by the relatively low average rainfall of the period. Qiao et al. also reported that the ET was limited by the amount of rainfall in a relatively dry period resulting in an insignificant difference between juniper and range grass [18]. Some woody plants are very adaptive to water stress. When there is less rainfall they consume less when the rainfall is over a threshold they consume more.

Table 55. Results of the benchmark and scenario models.

	swat-naip benchmark model	scenario model	observed
Period	2009-2011		
Mean Precipitation(mm)	508.60	508.60	490 (IDW)
Mean Water yield (mm)	25.07	24.33	26.59
Water yield/Rainfall	0.0492	0.0478	0.054
ET	459.50	459.70	
Baseflow/Total Flow	0.85	0.84	0.79
Surface runoff/Total Flow	0.15	0.16	0.21

The rainfall was about 350 mm in 2011 and remained below the 450 mm threshold proposed by Thurow and Wilcox as the minimum amount of rainfall required for a brush control to yield streamflow increase. But in 2009 and 2010 rainfall was over the proposed threshold. Simulated streamflow after juniper removal was higher only in May 2010 compared to pre-treatment model simulation. This finding was reasonable given the surface runoff contribution to total flow increase when there is sufficiently large runoff generating storm events. These results agree with the observational analysis. The mapped brush control in the study period was intensified in 2012 to 2014 removing at least about 8% of the juniper didn't result in a distinct increase in the streamflow. On the contrary, the water yield to rainfall ratio was the lowest in these two years. The decline in the streamflow may have resulted from the increase in the surface runoff as predicted by the scenario model simulation.

The scenario simulation results illustrated by Figure 65 indicated that average surface runoff increased by about 8% following the juniper removal with a concurrent 4.8% decrease in average baseflow which resulted in a 3% reduction in average water yield for the period. Baseflow ratio decreased by 1% after a hypothetical brush control. Because about 85% of the streamflow generated by the contribution of baseflow, water yield decreased slightly. This finding was in a good agreement with the study of Wilcox et al. (2010) in which they investigated the impact of woody plant encroachment on the streamflow of several watersheds in the Edwards Plateau including the Nueces River Watershed. They reported that in 3 out of the 4 watersheds, water yield increased following the brush encroachment. The water yield also increased in the Nueces River was the minimum among those three watersheds. They reported that improved land cover condition due to juniper encroachment, the baseflow almost doubled depending on the higher infiltration capacity of the soil.

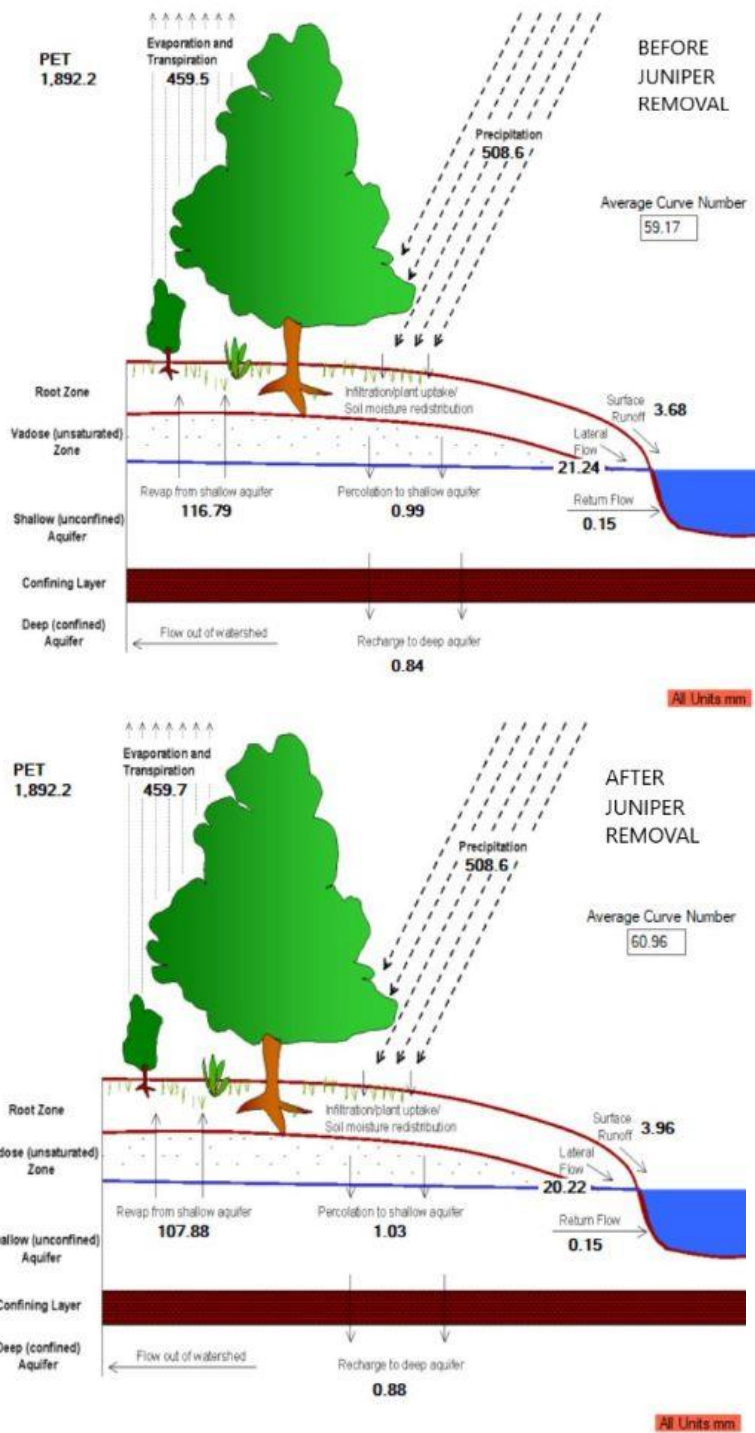


Figure 65. Before (above) and after (below) the simulation of the juniper removal.

CHAPTER V

CONCLUSION

Water yield from the semi-arid watersheds of Texas has long been under intense pressure due to changing climatic and ecological conditions. Rangelands in Texas have undergone considerable land use cover transformations in the last 150 years. The impact of the land use and cover change on the water yield has been investigated by several studies. These studies include long-term trend analysis of observed streamflow, and research using paired-catchment, experimental watershed, and hydrological modeling approaches.

Expansion in the woody plant cover has been considered a threat to water budget due to reported higher water use of brush species like salt cedar and juniper. The studies investigating the impact of brush control on water yield are usually based on hydrological modeling conducted mostly on small and mesoscale watersheds. Most of the modeling studies suggested brush removals as a viable resource management alternative for obtaining more water from the watersheds. However, the results of these studies weren't consistently confirmed by the observational field studies. Besides, the same or a single LULC dataset was used for both calibration and validation of the models. As a result, the data used for the model calibration and validation had similar climatic, geologic and ecologic conditions which were often sharply different from the conditions defined in the simulation scenarios. NLCD land cover data was widely used in these studies as the input land cover data to the SWAT model. However, the spatial

and temporal resolution of the NLCD is coarse. Therefore, the high model performance evaluation statistics obtained from these studies may be overrated in terms of the model's applicability to simulating the defined simulation scenarios.

The objectives of this study were to classify LULC types in the shadow areas of aerial images; to evaluate the complement between LULC data and ancillary data; to detect LULC changes covering the data period (2008-2017); and to assess the impact of land cover change on the water yield of the Nueces River Headwaters watershed by using multi-year and multi-sensor LULC data and the SWAT model.

National Agricultural Imagery Program (NAIP) and Landsat images were used to produce LULC maps of the study area (about 908 km²). Using higher-resolution NAIP images in image classification was more time consuming than using Landsat images. Based on the spatial resolution, classification schemes for NAIP and Landsat images were different. Higher-resolution LULC data was a requirement to quantify LULC change precisely for the 2008-2017 period. However, a sizable amount of shadow cover on the aerial images brought about a notable challenge. The average shadow cover in six aerial images used in this study accounted for 6.83% of the study area. The tradeoff between the temporal and spatial resolutions of the digital images (NAIP: higher spatial resolution, lower temporal resolution; Landsat: coarse spatial resolution, higher temporal resolution) was mitigated by the incorporation of multi-sensor data to image classifications. Thus, more than 99% of the shadow area was identified with a 92.68% average accuracy. Six higher-resolution (1 meter) LULC maps were derived from the National Agricultural Imagery Program (NAIP) images. The overall classification

accuracy using these maps ranged from 91.35% to 97.29%. I used a modified version of Anderson classification scheme to derive the LULC maps from Landsat 5 and Landsat 8 scenes. The acquisition dates of Landsat images corresponded with the data year of the NAIP images. These maps generated overall classification accuracies ranging from 87% to 94.59%.

Thematic change detection analysis was conducted using LULC maps derived from the NAIP images. The results revealed about an 8% (aggregated change detection) to 12.37% (original change detection) reduction in the total juniper cover of 2008 for the 2008-2014 period due to human (e.g. brush control) and climate-induced (e.g. drought) factors. Considering the notable LULC change, 2012, 2016 and 2008 LULC data were used to construct the SWAT models for the calibration (2012-2015), validation (2016-2017), and simulation scenario (2009-2011) periods, respectively. Also, the corresponding year's Landsat classification maps were used to test the model's sensitivity to different spatial resolutions and classification schemes of LULC data. The NLCD LULC data was used to construct a comparable model to validate formerly-reported parameters for the Nueces Headwaters Watershed and junipers.

Although satisfactory uncertainty estimates were obtained from the calibration of the model, the R^2 and NSE values were degraded in the validation of the model. The model constructed with the NLCD data and parameterized with the previously-reported parameters didn't yield satisfactory uncertainty estimates. A benchmark model was constructed for the 2009-2011 period using the most successful parameter set in the calibration and validation. Simulated baseflow, surface runoff, and total flow were

comparable to the observed data. A hypothetical 40% juniper removal scenario was simulated, and the results were compared with those of the benchmark model. An 8% increase in the average surface runoff, a 4.8% decrease in the average baseflow, and a 3% reduction in the average water yield were simulated by the scenario. The results were reasonable given the higher contribution of the baseflow to the total streamflow in the study area (about 80% for the 2009-2017 period).

Overall, LULC types of shadow area on higher-resolution images can be classified successfully with a straightforward method incorporating the multi-sensor LULC classification schemes. The high accuracy of multi-year and multi-sensor LULC maps revealed the benefits of ancillary data use in remote sensing image classification. Thematic change detection results indicated that the variability in LULC needs to be accounted for especially in hydrological modeling studies of large watersheds over a lengthy period. Because addressing a specific vegetation cover precisely is not possible with a coarser-resolution image classification scheme, the LULC maps derived from the higher-resolution NAIP images can be a viable alternative source of LULC data for hydrological modeling and LULC change monitoring.

My study makes several contributions to LULC classification and hydrological modeling. First, I developed and tested an approach to detecting LULC types in shadow areas of remote sensing images. Second, I assessed the feasibility and benefits of using multi-sensor data for LULC classification. Third, to best of my knowledge, this study may be the first study conducted in a large karst watershed in the Edwards Plateau which accounted for the watershed-wide LULC changes for the entire modeling period. The

approaches and results generated from this study would be of value for future LULC classification and hydrological modeling, especially in semi-arid rangelands.

This study, however, has limitations. The calibration and validation results of the SWAT model indicated that the model was somewhat sensitive to the resolution and classification scheme of the LULC data. The percent bias was lower for the model constructed with the higher-resolution LULC data. Poor uncertainty estimates obtained from the validation of the model imply that the model couldn't sufficiently assess the variability in the LULC and weather data for the relatively short validation period in this specific karst watershed. Unlike the former modeling studies investigating the impact of shrub encroachment/management on the water yield of the same and nearby watersheds, this study couldn't find an increase in the average water yield in the case of removing 40% of junipers in the study area. This outcome may imply that the increase in the surface runoff following the brush management may lead to a decrease in the baseflow and water yield in the karst-influenced watershed where the baseflow ratio substantially outweighs the surface runoff ratio. However, better model uncertainty estimates are necessary to support decision making on shrub management. Hence, the future hydrological modeling studies should thoroughly investigate the LULC changes that took place in the watersheds within the entire modeling period and focus on improving the model uncertainty estimates.

REFERENCES

1. White, R.P. and J. Nackoney, *Drylands, people, and ecosystem goods and services: a web-based geospatial analysis (PDF version)*. World Resources Institute (<http://pdf.wri.org/drylands.pdf> accessed on 30 January 2012), 2003.
2. Schimel, D.S., *Drylands in the earth system*. Science, 2010. **327**(5964): p. 418-419.
3. Huang, J., et al., *Drylands face potential threat under 2 °C global warming target*. Nature Climate Change, 2017. **7**(6): p. 417-422.
4. FAO, *Drylands, people and land use*. 2012.
5. Falkenmark, M. and J. Rockström, *Building resilience to drought in desertification-prone savannas in Sub-Saharan Africa: The water perspective*. Natural resources forum, 2008. **32**(2): p. 93-102.
6. Jackson, R., et al., *WATER IN A CHANGING WORLD*. Ecological applications, 2001. **11**(4): p. 1027-1045.
7. Lal, R., *Carbon sequestration in dryland ecosystems*. Environ Manage, 2004. **33**(4): p. 528-44.
8. Wilcox, B., M. Sorice, and M. Young, *Dryland Ecohydrology in the Anthropocene: Taking Stock of Human-Ecological Interactions*. Geography compass, 2011. **5**(3): p. 112-127.

9. R.Hart, C., *Brush Management for Water Conservation, Chapter 16*. Aquifers of the Edwards Plateau: Texas Water Development Board Report 360 (2004): 303-314., 2004.
10. Wilcox, B.P., et al., *Shrubs, streamflow, and the paradox of scale*. Hydrological Processes, 2006. **20**(15): p. 3245-3259.
11. Eggemeyer, K. and S. Schwinning, *Biogeography of woody encroachment: why is mesquite excluded from shallow soils?* Ecohydrology, 2009. **2**(1): p. 81-87.
12. Wilcox, B.P. and Y. Huang, *Woody plant encroachment paradox: Rivers rebound as degraded grasslands convert to woodlands*. Geophysical Research Letters, 2010. **37**(7).
13. Wu, X.B., E.J. Redeker, and T.L. Thurow, *Vegetation and Water Yield Dynamics in an Edwards Plateau Watershed*. Journal of Range Management, 2001. **54**(2): p. pp. 98-105.
14. Bradford P. Wilcox, M.K.O., Robert W. Knight, and Robert K. Lyons, *Do Woody Plants affect Streamflow On Semiarid Karst Rangelands?* Ecological Society of America, 2005. **15**(1): p. pp. 127–136.
15. Owens, M. and J. Ansley. *Ecophysiology and growth of Ashe and redberry juniper*. in *Juniper Symposium*. 1997. Texas A&M University: San Angelo, TX.
16. Afinowicz, J.D., C.L. Munster, and B.P. Wilcox, *MODELING EFFECTS OF BRUSH MANAGEMENT ON THE RANGELAND WATER BUDGET: EDWARDS PLATEAU, TEXAS I*. JAWRA Journal of the American Water Resources Association, 2005. **41**(1): p. 181-193.

17. White, J., et al., *The importance of parameterization when simulating the hydrologic response of vegetative land-cover change*. Hydrology and Earth System Sciences, 2017. **21**(8): p. 3975-3989.
18. Qiao, L., et al., *Calibration of SWAT model for woody plant encroachment using paired experimental watershed data*. Journal of Hydrology, 2015. **523**: p. 231-239.
19. Huxman, T., et al., *ECOHYDROLOGICAL IMPLICATIONS OF WOODY PLANT ENCROACHMENT*. Ecology, 2005. **86**(2): p. 308-319.
20. Wilcox, B.P., *Shrub control and streamflow on rangelands: A process based viewpoint*. Journal of Range Management, 2002: p. 318-326.
21. Thurow, T. *Assessment of brush management as a strategy for enhancing water yield*. in *Proceedings of the 25th Water for Texas Conference*. Texas Water Resources Institute, Texas A&M University System, College Station, TX. 1998.
22. Cardella Dammeyer, H., et al., *Effects of juniper removal and rainfall variation on tree transpiration in a semi-arid karst: evidence of complex water storage dynamics*. Hydrological Processes, 2016. **30**(24): p. 4568-4581.
23. Siriwardena, L., B.L. Finlayson, and T.A. McMahon, *The impact of land use change on catchment hydrology in large catchments: The Comet River, Central Queensland, Australia*. Journal of Hydrology, 2006. **326**(1-4): p. 199-214.
24. Arnold, J.G., et al., *Large area hydrologic modeling and assessment part I: model development*. JAWRA Journal of the American Water Resources Association, 1998. **34**(1): p. 73-89.

25. Mosbahi, M., S. Benabdallah, and M.R. Boussema, *Assessment of soil erosion risk using SWAT model*. Arabian Journal of Geosciences, 2012. **6**(10): p. 4011-4019.
26. Tadele, K. and G. Förch. *Impact of land use/cover change on streamflow: the case of Hare River Watershed, Ethiopia*. in *Catchment and lake research, proceedings 2nd Lake Abaya research symposium (LARS), Arba Minch, Ethiopia*. 2007.
27. Afinowicz, J.D., et al., *A Process for Assessing Wooded Plant Cover by Remote Sensing*. Rangeland Ecology & Management, 2005. **58**(2): p. 184-190.
28. Mace, R.E., et al., *Groundwater availability of the Trinity aquifer, Hill Country area, Texas: numerical simulations through 2050*. Texas Water Development Board Report, 2000. **353**: p. 117.
29. Archer, S., *Woody plant encroachment into southwestern grasslands and savannas: rates, patterns and proximate causes*. Ecological implications of livestock herbivory in the West, 1994.
30. Bednarz, S., et al., *Brush Management/Water Yield Feasibility Studies for Eight Watersheds in Texas—TR-182*. Texas Water Resources Institute, College Station, Texas, 2000.
31. Thanapakpawin, P., et al., *Effects of landuse change on the hydrologic regime of the Mae Chaem river basin, NW Thailand*. Journal of Hydrology, 2007. **334**(1-2): p. 215-230.

32. DeFries, R. and K.N. Eshleman, *Land-use change and hydrologic processes: a major focus for the future*. Hydrological processes, 2004. **18**(11): p. 2183-2186.
33. Seibert, J. and J.J. McDonnell, *Land-cover impacts on streamflow: a change-detection modelling approach that incorporates parameter uncertainty*. Hydrological Sciences Journal, 2010. **55**(3): p. 316-332.
34. Kundzewicz, Z.W. and A.J. Robson, *Change detection in hydrological records— a review of the methodology/revue méthodologique de la détection de changements dans les chroniques hydrologiques*. Hydrological sciences journal, 2004. **49**(1): p. 7-19.
35. Choodarathnakara, A., et al., *Mixed pixels: a challenge in remote sensing data classification for improving performance*. International Journal of Advanced Research in Computer Engineering & Technology (IJARCET), 2012. **1**(9): p. pp: 261-271.
36. Khatami, R., G. Mountrakis, and S.V. Stehman, *A meta-analysis of remote sensing research on supervised pixel-based land-cover image classification processes: General guidelines for practitioners and future research*. Remote Sensing of Environment, 2016. **177**: p. 89-100.
37. Xie, Y., Z. Sha, and M. Yu, *Remote sensing imagery in vegetation mapping: a review*. Journal of plant ecology, 2008. **1**(1): p. 9-23.
38. Ahmad, A. and S. Quegan, *Analysis of maximum likelihood classification on multispectral data*. Applied Mathematical Sciences, 2012. **6**(129): p. 6425-6436.

39. Barandela, R. and M. Juarez, *Supervised classification of remotely sensed data with ongoing learning capability*. International Journal of Remote Sensing, 2002. **23**(22): p. 4965-4970.
40. Haque, M.I. and R. Basak, *Land cover change detection using GIS and remote sensing techniques: A spatio-temporal study on Tanguar Haor, Sunamganj, Bangladesh*. The Egyptian Journal of Remote Sensing and Space Science, 2017. **20**(2): p. 251-263.
41. Baker, T.J. and S.N. Miller, *Using the Soil and Water Assessment Tool (SWAT) to assess land use impact on water resources in an East African watershed*. Journal of Hydrology, 2013. **486**: p. 100-111.
42. Lu, D. and Q. Weng, *A survey of image classification methods and techniques for improving classification performance*. International Journal of Remote Sensing, 2007. **28**(5): p. 823-870.
43. Arnold, J.G., et al., *SWAT: Model Use, Calibration, and Validation*. Transactions of the ASABE, 2012. **55**(4): p. 1491-1508.
44. Guse, B., D.E. Reusser, and N. Fohrer, *How to improve the representation of hydrological processes in SWAT for a lowland catchment - temporal analysis of parameter sensitivity and model performance*. Hydrological Processes, 2014. **28**(4): p. 2651-2670.
45. Cibin, R., K.P. Sudheer, and I. Chaubey, *Sensitivity and identifiability of stream flow generation parameters of the SWAT model*. Hydrological Processes, 2010. **24**(9): p. 1133-1148.

46. Moriasi, D.N., et al., *Model evaluation guidelines for systematic quantification of accuracy in watershed simulations*. Transactions of the ASABE, 2007. **50**(3): p. 885-900.
47. Jain, S., et al., *Simulating the Hydrologic Impact of Arundo donax Invasion on the Headwaters of the Nueces River in Texas*. Hydrology, 2015. **2**(3): p. 134-147.
48. Amatya, D.M., et al., *SWAT-Based Streamflow and Embayment Modeling of Karst-Affected Chapel Branch Watershed, South Carolina*. Transactions of the ASABE, 2011. **54**(4): p. 1311-1323.
49. Baffaut, C., C. Baffaut, and V.W. Benson, *Modeling Flow and Pollutant Transport in a Karst Watershed with SWAT*. Transactions of the ASABE, 2009. **52**(2): p. 469-479.
50. Ghanbarpour, M.R., et al., *Stochastic modeling of surface stream flow at different time scales: Sangsoorakh karst basin, Iran*. Journal of Cave and Karst Studies, 2010. **72**(1): p. 1-10.
51. Yactayo, G.A., *Modification of the SWAT model to simulate hydrologic processes in a karst-influenced watershed*. 2009, Virginia Tech.
52. Fisher, J.R.B., et al., *Impact of satellite imagery spatial resolution on land use classification accuracy and modeled water quality*. Remote Sensing in Ecology and Conservation, 2018. **4**(2): p. 137-149.
53. Wayne J. Gabriel, D.L.E.L., and James A. Douglass II Natural Resources Conservation Service, *Soil Survey of Edwards and Real Counties, Texas*. USDA,NRCS and in Cooperation with Texas Agrilife Research Center, 2009.

54. Daly, C., et al., *Physiographically sensitive mapping of climatological temperature and precipitation across the conterminous United States*. International Journal of Climatology, 2008. **28**(15): p. 2031-2064.
55. Noori, M.J., H.H. Hassan, and Y.T. Mustafa, *Spatial estimation of rainfall distribution and its classification in Duhok governorate using GIS*. Journal of Water Resource and Protection, 2014. **6**(02): p. 75.
56. Baillargeon, S., *Kriging: A review of theory and application to spatial interpolation of rainfall data*. 2005, M. Sc. Thesis, University of Laval, Quebec.
57. Keblouti, M., L. Ouerdachi, and H. Boutaghane, *Spatial interpolation of annual precipitation in Annaba-Algeria-comparison and evaluation of methods*. Energy Procedia, 2012. **18**: p. 468-475.
58. Lu, G. and D. Wong, *An adaptive inverse-distance weighting spatial interpolation technique*. Computers & geosciences, 2008. **34**(9): p. 1044-1055.
59. Li, J., et al., *Analyze and compare the spatial interpolation methods for climate factor*. Pratacultural Science, 2006. **8**: p. 001.
60. Dirks, K., et al., *High-resolution studies of rainfall on Norfolk Island: Part II: Interpolation of rainfall data*. Journal of Hydrology, 1998. **208**(3-4): p. 187-193.
61. CHU, S.-l., et al., *Study on spatial precipitation interpolation methods—A case of Gansu province [J]*. Pratacultural Science, 2008. **6**: p. 006.
62. Taesombat, W. and N. Sriwongsitanon, *Areal rainfall estimation using spatial interpolation techniques*. Science Asia, 2009. **35**(3): p. 268-275.

63. Anderson, J.R., *A land use and land cover classification system for use with remote sensor data*. Vol. 964. 1976: US Government Printing Office.
64. Wickham, J.D., et al., *Accuracy assessment of NLCD 2006 land cover and impervious surface*. *Remote Sensing of Environment*, 2013. **130**: p. 294-304.
65. Elliott, L.F., et al., *Ecological mapping systems of Texas: summary report*. Texas Parks and Wildlife Department, Austin, Texas, 2014.
66. Richards, J.A. and J. Richards, *Remote sensing digital image analysis*. Vol. 3. 1999: Springer.
67. Montanaro, M., et al., *Stray light artifacts in imagery from the Landsat 8 Thermal Infrared Sensor*. *Remote Sensing*, 2014. **6**(11): p. 10435-10456.
68. Ustuner, M., F.B. Sanli, and B. Dixon, *Application of Support Vector Machines for Landuse Classification Using High-Resolution RapidEye Images: A Sensitivity Analysis*. *European Journal of Remote Sensing*, 2017. **48**(1): p. 403-422.
69. Mas, J.-F., et al., *A Suite of Tools for Assessing Thematic Map Accuracy*. *Geography Journal*, 2014. **2014**: p. 1-10.
70. Stehman, S.V. and R.L. Czaplewski, *Design and analysis for thematic map accuracy assessment: fundamental principles*. *Remote sensing of environment*, 1998. **64**(3): p. 331-344.
71. Lillesand, T., R.W. Kiefer, and J. Chipman, *Remote sensing and image interpretation*. 2014: John Wiley & Sons.

72. Scepán, J., *Thematic validation of high-resolution global land-cover data sets*. *Photogrammetric engineering and remote sensing*, 1999. **65**(9): p. 1051-1060.
73. Story, M. and R.G. Congalton, *Accuracy assessment: a user's perspective*. *Photogrammetric Engineering and remote sensing*, 1986. **52**(3): p. 397-399.
74. Jensen, J., *Introductory digital image processing: a remote sensing perspective: Pearson Prentice Hall*. Upper Saddle River, NJ, 2005.
75. Woldesenbet, T.A., et al., *Hydrological responses to land use/cover changes in the source region of the Upper Blue Nile Basin, Ethiopia*. *Science of the Total Environment*, 2017. **575**: p. 724-741.
76. Awotwi, A., F. Yeboah, and M. Kumi, *Assessing the impact of land cover changes on water balance components of White Volta Basin in West Africa*. *Water and Environment Journal*, 2015. **29**(2): p. 259-267.
77. Moussa, R. *Significance of the Nash-Sutcliffe efficiency measure for linear rise and exponential recession in event based flood modelling*. in *Geophysical Research Abstracts*. 2008.
78. Santhi, C., et al., *Validation of the swat model on a large river basin with point and nonpoint sources*. *JAWRA Journal of the American Water Resources Association*, 2001. **37**(5): p. 1169-1188.
79. Van Liew, M., J. Arnold, and J. Garbrecht, *Hydrologic simulation on agricultural watersheds: Choosing between two models*. *Transactions of the ASAE*, 2003. **46**(6): p. 1539.

80. Fernandez, G.P., et al., *Development and testing of watershed-scale models for poorly drained soils*. Transactions of the ASAE, 2005. **48**(2): p. 639-652.